

REPORT DOCUMENTATION PAGE

Form Approved
OMB No. 0704-0188

The public reporting burden for this collection of information is estimated to average 1 hour per response, including the time for reviewing instructions, searching existing data sources, gathering and maintaining the data needed, and completing and reviewing the collection of information. Send comments regarding this burden estimate or any other aspect of this collection of information, including suggestions for reducing the burden, to Department of Defense, Washington Headquarters Services, Directorate for Information Operations and Reports (0704-0188), 1215 Jefferson Davis Highway, Suite 1204, Arlington, VA 22202-4302. Respondents should be aware that notwithstanding any other provision of law, no person shall be subject to any penalty for failing to comply with a collection of information if it does not display a currently valid OMB control number.

PLEASE DO NOT RETURN YOUR FORM TO THE ABOVE ADDRESS.

1. REPORT DATE (DD-MM-YYYY) 10/Aug/2001	2. REPORT TYPE THESIS	3. DATES COVERED (From - To)		
4. TITLE AND SUBTITLE COMPUTATIONAL EVALUATION OF QUIET TUNNEL HYPERSONIC BOUNDARY LAYER STABILITY EXPERIMENTS		5a. CONTRACT NUMBER		
		5b. GRANT NUMBER		
		5c. PROGRAM ELEMENT NUMBER		
6. AUTHOR(S) 2D LT MANNING MELISSA L		5d. PROJECT NUMBER		
		5e. TASK NUMBER		
		5f. WORK UNIT NUMBER		
7. PERFORMING ORGANIZATION NAME(S) AND ADDRESS(ES) NORTH CAROLINA STATE UNIVERSITY			8. PERFORMING ORGANIZATION REPORT NUMBER CI01-195	
9. SPONSORING/MONITORING AGENCY NAME(S) AND ADDRESS(ES) THE DEPARTMENT OF THE AIR FORCE AFIT/CIA, BLDG 125 2950 P STREET WPAFB OH 45433			10. SPONSOR/MONITOR'S ACRONYM(S)	
			11. SPONSOR/MONITOR'S REPORT NUMBER(S)	
12. DISTRIBUTION/AVAILABILITY STATEMENT Unlimited distribution In Accordance With AFI 35-205/AFIT Sup 1				
13. SUPPLEMENTARY NOTES				
14. ABSTRACT				
20010904 042				
15. SUBJECT TERMS				
16. SECURITY CLASSIFICATION OF: a. REPORT		17. LIMITATION OF ABSTRACT	18. NUMBER OF PAGES 104	19a. NAME OF RESPONSIBLE PERSON 19b. TELEPHONE NUMBER (Include area code)

BIOGRAPHY

~~Melissa Joy Manning was born in Miami, Florida and grew up in Burnsville, North Carolina with her parents, Donald and Carolyn Lister and her sisters, Laura Cifaldi and Missa Lister. In July 1998, she married Rufus Manning, Jr. of Raleigh, NC.~~

She earned her Bachelor of Science degree in Aerospace Engineering at North Carolina State University in December 1998 with a minor in Military Science. In December 1998, she was also commissioned as a Second Lieutenant in the United States Air Force. In January 1999, she returned to NC State to pursue her Master's Degree in Aerospace Engineering with a minor in Mathematics and graduated in December 2000. Melissa is currently serving in the Air Force as an Aerospace Developmental Engineer.

ACKNOWLEDGEMENTS

Many people have supported me though out my Master's work, both professionally and personally. I would like to thank Dr. Nd Chokani for his diligence and enthusiasm and for the substantial amount of instruction and patience he afforded me. My appreciation goes to Dr. Jack Edwards for his assistance in running his Navier-Stokes solver. A special thanks goes to Dr. Joe Marlin for his help with the mathematical aspects of my research. I would like to acknowledge the North Carolina Supercomputing Center for providing time on the Cray T-196 for my calculations. I would like to extend my appreciation to the Air Force Institute of Technology for their generous support and for affording me the opportunity to pursue my Master's degree. I would also like to acknowledge the Department of Mechanical and Aerospace Engineering for their financial support. Additionally, I would like to thank my lab partners for their help and encouragement, especially, Ryan, Keith, Randy and Jeff. They were always there to answer my questions and listen to my complaints.

Finally, I am ever grateful to my family for their continued support.

TABLE OF CONTENTS

	<i>Page</i>
LIST OF TABLES	vi
LIST OF FIGURES	vii
LIST OF SYMBOLS	x
1 INTRODUCTION	1
1.1 Motivation	1
1.2 Transition Process	1
1.3 Empirical Methods	2
1.4 Stability Theory	3
1.5 Stability Experiments	6
1.6 Freestream Noise	6
1.7 Quiet Wind Tunnel	7
1.8 Effects of Pressure Gradient and Cooling	8
1.9 Objectives and Approach	8
2 WIND TUNNEL EXPERIMENTS	13
2.1 Introduction	13
2.2 Mach 6 Axisymmetric Quiet Nozzle Facility	15
2.3 Models	16
2.4 Measurements	18
3 NUMERICAL METHOD	28
3.1 Introduction	28
3.2 Grid Generation	29
3.3 Mean Flow Analysis	30

	<i>Page</i>
3.4 Grid Refinement Study	33
3.5 Linear Stability Theory	35
4 RESULTS AND DISCUSSION	44
4.1 Introduction	44
4.2 Mean Flow Analysis	44
4.3 Linear Stability Analysis	54
5 CONCLUDING REMARKS	97
REFERENCES	100

LIST OF TABLES

<i>Table</i>	<i>Page</i>
3.1 Case Descriptions for 91-6 Model Grid Refinement Study	39
3.2 Grid Spacing for 93-10 Model	39

LIST OF FIGURES

<i>Figure</i>	<i>Page</i>
1.1 Transition Process	10
1.2 Comparison of Sharp Cone Transition Reynolds Numbers from Wind Tunnels and an Aeroballistic range	11
1.3 Comparison of Transition Onset Reynolds Numbers on a Cone and Flat Plate .	12
2.1a Disturbances in a Conventional Wind Tunnel	22
2.1b Quiet wind Tunnel Design	22
2.2 NASA Langley Quiet Wind Tunnel Facility	23
2.3 91-6 Cone-Flare Model and Dimensions	24
2.4 Active Cooling System for 91-6 Cooled Cone	24
2.5 93-10 Cone-Flare Model and Dimension	25
2.6 Placement of Flared Cone Models in Wind Tunnel	26
2.7 Freestream RMS Contours	26
2.8 Constant Voltage Anemometer Circuit	27
2.9 Hot-Wire Probe	27
3.1 Computational Grid, 91-6 Model	40
3.2 Convergence History	40
3.3 Effect of Grid Spacing on Velocity Profiles, $x=9"$	41
3.4 Effect of Grid Spacing on Temperature Profiles, $x=9"$	41
3.5 Effect of Grid Spacing on First Derivative of Velocity Profiles, $x=9"$	42
3.6 Effect of Grid Spacing on First Derivative of Temperature Profiles, $x=9"$	42
3.7 Effect of Grid Spacing on Generalized Inflection Point Profiles, $x=9"$	43
3.8 Effect of Grid Spacing on Boundary Layer Thickness Distribution	43
4.1 Pressure Distribution on 91-6 and 93-10 Models	61
4.2 Velocity Profiles at $x=11"$	61
4.3 Temperature Profiles at $x=11"$	62
4.4 Density Profiles at $x=11"$	62
4.5 Mass Flux Profiles at $x=11"$	63
4.6 Total Temperature Profiles at $x=11"$	63
4.7 First Derivative of Velocity Profiles at $x=11"$	64
4.8 First Derivative of Temperature Profiles at $x=11"$	64
4.9 First Derivative of Density Profiles at $x=11"$	65
4.10 Second Derivative of Velocity Profiles at $x=11"$	65
4.11 Second Derivative of Temperature Profiles at $x=11"$	66
4.12 Second Derivative of Density Profiles at $x=11"$	66
4.13 Generalized Inflection Point Profiles at $x=11"$	67
4.14 Effect of Wall Cooling on Boundary Layer Thickness Distribution, 91-6 Model	67
4.15 Surface Pressure Distribution, 91-6 Model	68
4.16 Effect of Wall Cooling on Surface Temperature Distribution, 91-6 Model	68
4.17 Curve Fit to 91-6 Cooled Model Experimentally Measured Surface Temperature Distribution	69

<i>Figure</i>	<i>Page</i>
4.18 Effect of Initial Temperature Profile on Boundary Layer Thickness Distribution for 91-6 Cooled Model	69
4.19 Velocity Profiles at $x=9"$ for 91-6 Cooled Model with Constant and Variable Wall Temperature Boundary Conditions	70
4.20 Velocity Profiles at $x=13"$ for 91-6 Cooled Model with Constant and Variable Wall Temperature Boundary Conditions	70
4.21 Total Temperature Profiles at $x=9"$ for 91-6 Cooled Model with Constant and Variable Wall Temperature Boundary Conditions	71
4.22 Total Temperature Profiles at $x=13"$ for 91-6 Cooled Model with Constant and Variable Wall Temperature Boundary Conditions	71
4.23 Density Profiles at $x=9"$ for 91-6 Cooled Model with Constant and Variable Wall Temperature Boundary Conditions	72
4.24 Density Profiles at $x=13"$ for 91-6 Cooled Model with Constant and Variable Wall Temperature Boundary Conditions	72
4.25 Pressure Distribution for 93-10 Adiabatic Model	73
4.26 Temperature Distribution for 93-10 Adiabatic Model	73
4.27 Effect of Adverse Pressure Gradient on Boundary Layer Thickness Distribution	74
4.28 Boundary Layer Thickness Distribution for 93-10 Adiabatic Model	74
4.29 Comparison of Calculated Total Temperature and Normalized Wire Resistance Obtained in Low Overheat at $x=9"$ (91-6 Adiabatic Model)	75
4.30 Comparison of Calculated Total Temperature and Normalized Wire Resistance Obtained in Low Overheat at $x=9"$ (91-6 Cooled Model)	75
4.31 Normalized Total Temperature Contour Plot, 91-6 Adiabatic Model	76
4.32 Contour Plot of Normalized R_w Obtained in Low Overheat, 91-6 Adiabatic Model	76
4.33 Normalized Mass Flux Contour Plot, 91-6 Adiabatic Model	77
4.34 Contour Plot of Normalized $V_{s,mean}$ Obtained in High Overheat, 91-6 Adiabatic Model	77
4.35 Normalized Total Temperature Contour Plot, 91-6 Cooled Model	78
4.36 Contour Plot of Normalized R_w Obtained in Low Overheat, 91-6 Cooled Model	78
4.37 Normalized Mass Flux Contour Plot, 91-6 Cooled Model	79
4.38 Contour Plot of Normalized $V_{s,mean}$ Obtained in High Overheat, 91-6 Cooled Model	79
4.39 Mass Flux Profiles at Select Streamwise Locations, 93-10 Adiabatic Model ..	80
4.40 Total Temperature Profiles at Select Streamwise Locations, 93-10 Adiabatic Model	81
4.41 Pitot Pressure Profiles	82
4.42 Pitot Pressure Distribution for Various x -locations Along 91-6 Cooled Model Surface	82
4.43 Pitot Pressure Distribution for Various x -locations for Stetson's Experiments ..	83
4.44 Time Constant Values as a Function of Hot-Wire Reynolds Numbers and Currents	84

<i>Figure</i>	<i>Page</i>
4.45 Wire Reynolds Number for 0.0001in Wire at Various Streamwise Locations, 91-6 Adiabatic Model	85
4.46 Wire Reynolds Number for 0.0001in Wire at Various Streamwise Locations, 91-6 Cooled Model	85
4.47 Wire Reynolds Number for 0.0001in Wire at Various Streamwise Locations, 93-10 Adiabatic Model	86
4.48 Amplification Rates for 91-6 and 93-10 Models	86
4.49 Estimated Second-Mode Disturbance Frequency with Measured <i>N</i> -Factor Contours for 0° Baseline Case	87
4.50 Hot-wire Measurement Location, Front View of Model	87
4.51 Effect of Variable Temperature Distribution on Amplification Rates, 91-6 Cooled Model	88
4.52 Amplification Rates for Peak Second Mode Frequencies	89
4.53 <i>N</i> -factor Variation for Peak Second Mode Frequencies	89
4.54 Density Eigenfunctions for 91-6 and 93-10 Models, $x=13''$	90
4.55 Velocity Eigenfunctions for 91-6 and 93-10 Models, $x=13''$	90
4.56 Mass Flux Eigenfunctions for 91-6 and 93-10 Models, $x=13''$	91
4.57 Total Temperature Eigenfunctions for 91-6 and 93-10 Models, $x=13''$	91
4.58 RMS Hot-wire Output for 91-6 Adiabatic Model at $x=9''$	92
4.59 RMS Hot-wire Output for 91-6 Cooled Model at $x=9''$	92
4.60 Streamwise Evolution of DNS Computed Mass Flux Fluctuations, 93-10 Model	93
4.61 Normalized Mass Flux Contour Plot, 91-6 Adiabatic Model	93
4.62 Normalized Total Temperature Contour Plot, 91-6 Adiabatic Model	94
4.63 Hot-Wire Survey Path and RMS Contours for 91-6 Adiabatic Model	94
4.64 Normalized Mass Flux Contour Plot, 91-6 Cooled Model	95
4.65 Normalized Total Temperature Contour Plot, 91-6 Cooled Model	95
4.66 Hot-Wire Survey Path and RMS Contours for 91-6 Cooled Model	96

LIST OF SYMBOLS

Roman Symbols

A	Integrated amplitude
a	Speed of sound (Section 1.2), Wire sensitivity (Section 4.2)
b	Wire sensitivity
c_r	Phase velocity
e	Hot-wire output (Section 2.4), Internal energy (Section 3.3)
\mathbf{E}, \mathbf{F}	Flux vectors
E_t	Total energy
f	Frequency
i	$\sqrt{-1}$
J	Jacobian
k	Thermal conductivity
M	Mach number
N	Exponent in e^N transition prediction criterion
P, p	Pressure
q	Heat flux (Section 3.3), Flow variable (Section 3.5)
Re	Reynolds number
R	Resistance of sensing element (Section 2.4), Square root of Re (Chapter 4)
R_s	Square root of Reynolds number based on arc length
\mathbf{S}	Source vector
$S_{\rho u}, S_{T o}$	Sensitivity coefficients
t	Time
T	Temperature
u	Streamwise velocity
\mathbf{U}	Vector of conserved variables
U_c	Contravariant streamwise velocity component
v	Streamwise normal velocity
V_s	Output voltage of CVA
V_c	Contravariant streamwise normal velocity component
w	Spanwise velocity
x	Coordinate in streamwise direction
y	Coordinate in surface normal direction

Greek Symbols

α	Streamwise wave number (Sections 1.2 and 3.5), Temperature coefficient of resistivity (Section 2.4)
α_i	Amplification rate
β	Spanwise wave number
δ	Boundary layer thickness
Δ	Gradient
ζ	Spanwise transformed coordinate
η	Surface normal transformed coordinate
μ	Molecular viscosity
ξ	Streamwise transformed coordinate

ρ	Density
τ	Stress
ϕ	Vector of disturbance variables
ω	Disturbance frequency
Subscripts	
e	Boundary layer edge
I	Inviscid
l	Local
o	Total or stagnation conditions, Initial condition (Section 3.5)
ref	Reference
RMS, rms	Root mean square
T	Transition
Tr	Transition
V	Viscous
w	Wire
x	Streamwise direction
y	Surface normal direction
θ	Circumferential direction
∞	Conditions in the freestream
Superscripts	
$'$	Fluctuation
$^{\wedge}$	Eigenfunction
$-$	Mean component
Abbreviations	
CCA	Constant current anemometer
CTA	Constant temperature anemometer
CVA	Constant voltage anemometer
DC	Direct current
DNS	Direct numerical simulation
LES	Large eddy simulation
LST	Linear stability theory
PSE	Parabolized stability equations
RMS	Root mean square
T-S	Tollmien-Schlichting

ABSTRACT

Manning, Melissa Lynn. Computational Evaluation of Quiet Tunnel Hypersonic Boundary Layer Stability Experiments. (Under the direction of Dr. Ndaona Chokani.)

A computational evaluation of two stability experiments conducted in the NASA Langley Mach 6 axisymmetric quiet nozzle test chamber facility is conducted. Navier-Stokes analysis of the mean flow and linear stability theory analysis of boundary layer disturbances is performed in the computations. The effects of adverse pressure gradient and wall cooling are examined.

Calculated pressure, temperature and boundary layer thickness distributions show very good overall agreement with experimental measurements. Computed mass flux and total temperature profiles show very good quantitative agreement with uncalibrated hot-wire measurements obtained with the hot-wire operated in high and low overheat modes respectively. Comparisons between calibrated hot-wire data and mean flow computations show excellent agreement in the early stages of the transitional flow. However, examination of the wire Reynolds number and mass flux and total temperature eigenfunction profiles suggest that when operated in high overheat mode the sensitivity of the hot-wire to total temperature is significant. Thus, while uncalibrated hot-wire measurements are useful to characterize the overall features of the flow, calibrated hot-wire measurements are necessary for quantitative comparison with stability theory. Computations show that adverse pressure gradient and wall cooling decrease the boundary layer thickness and increase the frequency and amplification rate of the unstable second mode disturbances; these findings are consistent with the experimental observations.

**COMPUTATIONAL EVALUATION OF QUIET TUNNEL
HYPersonic BOUNDARY LAYER STABILITY EXPERIMENTS**

by

Melissa Lynn Manning

A thesis submitted to the Graduate Faculty of
North Carolina State University
in partial fulfillment of the
requirements for the Degree of
Master of Science

Aerospace Engineering

Raleigh, NC
November 2000

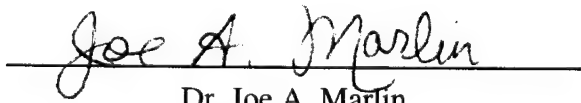
Approved by:



Dr. Ndaona Chokani
Advisory Committee Chairman



Dr. Jack R. Edwards
Advisory Committee Member



Dr. Joe A. Marlin
Advisory Committee Minor Representative

**THE VIEWS EXPRESSED IN THIS ARTICLE
ARE THOSE OF THE AUTHOR AND DO NOT
REFLECT THE OFFICIAL POLICY OR
POSITION OF THE UNITED STATES,
DEPARTMENT OF DEFENSE, OR THE U.S.
GOVERNMENT**

CHAPTER 1

INTRODUCTION

1.1 Motivation

The location and extent of boundary layer transition is a major issue in the design of hypersonic atmospheric and reentry vehicles. The nature of the boundary layer over the vehicle affects the aerodynamic performance of the vehicle as well as thermal protection system and propulsion system requirements. In hypersonic flight, vehicles experience much higher skin friction and surface heat transfer due to transitional and turbulent boundary layer flow than for laminar boundary layer flow. Transition delay can result in significant drag reduction and can greatly reduce aerodynamic heating loads. Thus, there exists a fundamental need for accurate laminar to turbulent boundary layer transition prediction tools in order to accomplish improved vehicle design at hypersonic speeds.

1.2 Transition Process

Natural laminar to turbulent boundary layer transition, Figure 1.1, is a multistage process, which is initiated from an initial, external disturbance field (White, 1991). This external disturbance field is internalized in the boundary layer through receptivity. The term receptivity was coined by Morkovin (1969) to define the means by which a disturbance environment generates growing disturbances in a boundary layer. Stages of linear and nonlinear growth of the internalized disturbances follow receptivity and lead to the onset of transition and the breakdown to turbulent flow. Transition can also be

described as a consequence of the laminar boundary layer acting as a nonlinear oscillator to environmental disturbances (Reshotko, 1994).

In attempting to describe the natural transition process, either the transition approach or stability theory are followed (Lachowicz and Chokani, 1996). Empirical methods are often used in the transition approach and are only able to locate transition. Thus, in the transition approach, the Reynolds number at either the onset or end of transition is determined and no details of the transition phenomena nor the disturbance mechanisms that caused the transition are included. Stability theory, on the other hand, describes the behavior of the disturbances in the flow leading to boundary layer transition; this provides a physical understanding of the transition process. In between these two approaches is transition modeling; in the more recent approach of Warren and Hassan (1998) stability theory is used to provide the basic elements of the modeling for transition prediction.

1.3 Empirical Methods

In the past, empirical relationships that are based on mean flow parameters such as edge Mach number and Reynolds number have been used to predict boundary layer transition. Herbert states that empirical methods should be supported by a broad database and must account for all parameters relevant to the flow (1991). In the hypersonic flight range, wind tunnel data obtained under realistic flight conditions are sparse. Reentry flight data have also been used to determine empirical relationships. When ablating thermal protection systems were used on reentry vehicles, accurate transition prediction was not critical and empirical relationships were adequate for use as a design tool.

However, modern hypersonic vehicles have strict weight limitations and conservative ablative systems are no longer feasible. Thus, empirical relationships are no longer useful for hypersonic vehicle design.

1.4 Stability Theory

Stability theory provides details of the mechanisms that subsequently lead to transition. Most of our knowledge of hypersonic boundary layer stability theory comes from Mack's pioneering work (1984, 1987). In hypersonic flows, inviscid instability dominates viscous stability at all Reynolds numbers. Mack showed that there are multiple modes of inviscid instability for hypersonic flow. The low frequency first mode or Tollmien-Schlichting (T-S) instability is due to vorticity disturbances, which exist if there is a generalized inflection point (gip) somewhere in the boundary layer. If the local Mach number relative to the phase velocity, defined as

$$M_l = \frac{u - c_r}{a} \quad (1.2.1)$$

is subsonic everywhere, Lees and Lin (1946) showed that a gip, defined as

$$\frac{\partial}{\partial y} \left(\rho \frac{\partial u}{\partial y} \right) = 0 \quad (1.2.2)$$

is a sufficient condition for the existence of a first mode instability. For compressible flow, the most unstable first mode disturbance is always oblique.

Mack showed that in addition to the first mode instability, multiple solutions to the inviscid stability equations exist if $\bar{M}^2 > 1$, that is if a relatively supersonic region exists somewhere in the boundary layer, where

$$\bar{M}^2 = \frac{(\alpha u - \omega) M_e}{((\alpha^2 + \beta^2) T)^{1/2}} \quad (1.2.3)$$

$\overline{M}^2 > 1$ is a sufficient condition for the inviscid disturbances to exist and the presence of a generalized inflection point is not required. The additional solutions, so called higher modes, are referred to as Mack modes and physically represent new instabilities that can affect hypersonic transition. Equation 1.2.3 is first satisfied at an edge Mach number of 2.2 for the case of an insulated flat plate boundary layer; this is the lowest Mach number where Mack modes can exist. The high frequency Mack modes are acoustical in character. The first of the Mack modes is called the second mode and it is the most unstable. For hypersonic boundary layers, the second mode disturbances are more dominant than first mode disturbances and are responsible for transition. The most unstable disturbances are two-dimensional for the Mack modes. Mack also discovered evidence of the tuning effect of the boundary layer, where the most amplified disturbances have a wavelength of approximately twice the boundary layer thickness. Thus, as the boundary layer thickness decreases, the second mode frequency increases.

The hierarchy of stability analysis methods involve, in order of decreasing complexity, direct numerical simulation, large eddy simulation, parabolized stability theory, and linear stability theory. Direct numerical simulation (DNS) is a method that attempts to resolve all features of the flow in time and space down to the smallest turbulence scales. Large eddy simulation (LES) assumes that the nature of the flow is contained primarily in larger eddies which can be calculated on a suitable grid; smaller eddies are assumed to behave more universally and are modeled without regard to the flow. Application of both LES and DNS is restricted by computer time and memory requirements, with computation times ranging from days to months and thus, only simple geometries are computed. For example, Pruett and Chang's spatial DNS calculation

simulating the Lachowicz and Chokani (1996) Mach 6 flow on an axisymmetric flared cone had a run time of approximately 250 hours on a Cray supercomputer (1998). Parabolized stability equations (PSE) model the spatially evolving linear and nonlinear instabilities in a growing boundary layer flow. Chang and Malik (1993) showed that the PSE are able to predict the nonlinear effects observed in the experiments of Stetson *et al* (1983). However, the PSE are computationally demanding to solve. The PSE are space marched and initial conditions must be specified; these initial conditions are not completely defined for many experiments. Furthermore, for largely uncalibrated experimental stability measurements, comparisons between flow variables and PSE calculations are difficult at best. Linear stability theory (LST) models the spatially evolving linear instabilities and assumes parallel boundary layer flow. Thus, LST is not restricted by computer time or memory requirements and solutions on complex geometries are easier to obtain. The basis of linear stability theory is that all flow variables of a perturbation grow or decay in the same manner. Kimmel and Kendall (1991) stated that in the linear region the individual hot-wire components need not be known and only the logarithmic growth or decay of the voltage fluctuation is required to determine the amplification rate. Thus, amplification rates derived from uncalibrated hot-wire data are comparable to LST calculations. Mack showed that LST adequately describes the onset of the second mode disturbance growth and the initial growth characteristics (1987). Malik stated that while the transition process is a complex, rate-dominated process, prediction methods may be based solely upon LST (1989). This work utilizes LST to examine boundary layer instabilities.

1.5 Stability Experiments

The stability experiments of Kendall (1975) provided the first confirmation of the existence and dominance of the second-mode disturbances in hypersonic boundary layer flow. Demetriades' experiments revealed the periodic wavelike structure of laminar boundary layers (1977). Stetson *et al* performed a series of experiments that examined the effects of bluntness, angle of attack, unit Reynolds number and environmental effects on the stability of laminar boundary layer flow over a cone (1983, 1984, 1986, 1989). Demetriades (1978) and Stetson (1983) have verified Mack's findings that the wavelength of the most amplified second-mode disturbance is approximately twice the boundary layer thickness. Kimmel and Poggie examined the effect of total temperature on boundary layer stability (2000). All of the above mentioned experiments were conducted in conventional wind tunnels. It is commonly known that conventional high-speed wind tunnel flows produce large amplitude freestream disturbances. Thus, the use of conventional wind tunnel data to predict flight transition is hindered by the influence of the tunnel's freestream disturbance environment.

1.6 Freestream Noise

The primary source of wind tunnel freestream disturbances is sound radiated into the test section from the turbulent boundary layer on the nozzle walls. The frequency content of the sound radiation excites disturbances in the boundary layer and results in transition locations farther upstream than found in flight. Pate (1971) presented a comparison of transition Reynolds numbers for three conventional wind tunnels with aeroballistic range data obtained by Potter (1968), Figure 1.2. The wind tunnel transition

Reynolds numbers are significantly lower than the flight data. This early transition occurs because the wind tunnel freestream disturbances are large enough to bypass linear growth and force early nonlinear growth, so-called bypass transition (Reshotko, 1994). The wind tunnel environment provides the mechanism by which boundary layer disturbance growth is initiated and establishes the initial disturbance amplitude at the onset of the disturbance growth (Stetson *et al*, 1986). Thus, different acoustic disturbance environments found in different conventional wind tunnels also produce different transition results. This is evident when comparing the transition Reynolds numbers from the three different wind tunnels seen in Figure 1.2. Discrepancies are also found when comparing conventional wind tunnel data with stability analysis data, which assume that no freestream disturbances are present, see Mack (1987) for example. Thus, the usefulness of stability data acquired in the conventional wind tunnel experiments is limited (Reshotko, 1997).

1.7 Quiet Wind Tunnel

In order to obtain stability measurements indicative of free flight, wind tunnels with very low freestream disturbance environments, so called quiet wind tunnels, are desired. Laminar boundary layer flow on the nozzle walls is required to decrease the sound radiated into the test section and achieve low freestream disturbance levels. Stability experiments conducted in quiet wind tunnels yield transition data comparable to that obtained in free flight. Chen *et al* (1989) showed good agreement between transition Reynolds number measurements obtained in a Mach 3.5 low disturbance wind tunnel and predictions of stability theory as seen in Figure 1.3. In the early 1990's, the NASA

Langley Research Center developed a Mach 6 quiet wind tunnel facility. Three stability experiments were conducted by Lachowicz *et al* (1996), Doggett *et al* (1997) and Blanchard and Selby (1996) in this facility before it was decommissioned. These experiments examined the effects of adverse pressure gradient, angle of attack and wall cooling respectively on flared-cone geometries. It is necessary to compare stability analysis results with data obtained in the quiet tunnel environment in order to further validate stability analysis as an accurate and useful tool in aerospace vehicle design.

1.8 Effects of Pressure Gradient and Cooling

Wall curvature and cooling affect boundary layer stability (Balakumar and Malik, 1994). The concave wall curvature results in Görtler vortices (Hall, 1982) which destabilize the flow. The adverse pressure gradient, which results from the concave curvature, introduces an inflection point in the streamwise mean velocity profile that is destabilizing. The boundary layer edge Mach number is also reduced and thus the boundary layer thickness decreases (Reshotko, 1994). Wall cooling removes the inflection point in the velocity profile, which stabilizes the first mode. However, a relative supersonic region remains and the second mode disturbances are further destabilized (Stetson *et al*, 1989).

1.9 Objectives and Approach

This work has two main objectives. First, to compare Navier-Stokes mean flow and LST computations to experimental measurements obtained in a quiet tunnel environment. The effects of wall cooling and pressure gradient are examined. Second, to

assess the use of hot-wire anemometry and make recommendations for future quiet tunnel experiments.

Details of the quiet wind tunnel facility, test conditions, model dimensions, and hot-wire measurements are presented in Chapter 2. Chapter 3 discusses grid generation, the Navier-Stokes mean flow solver, the grid refinement study and the LST code. In Chapter 4, comparisons are made between mean flow and LST computations and experimental measurements. Discussions concerning future experiments are also presented. Conclusions and recommendations for future computational work are presented in Chapter 5.

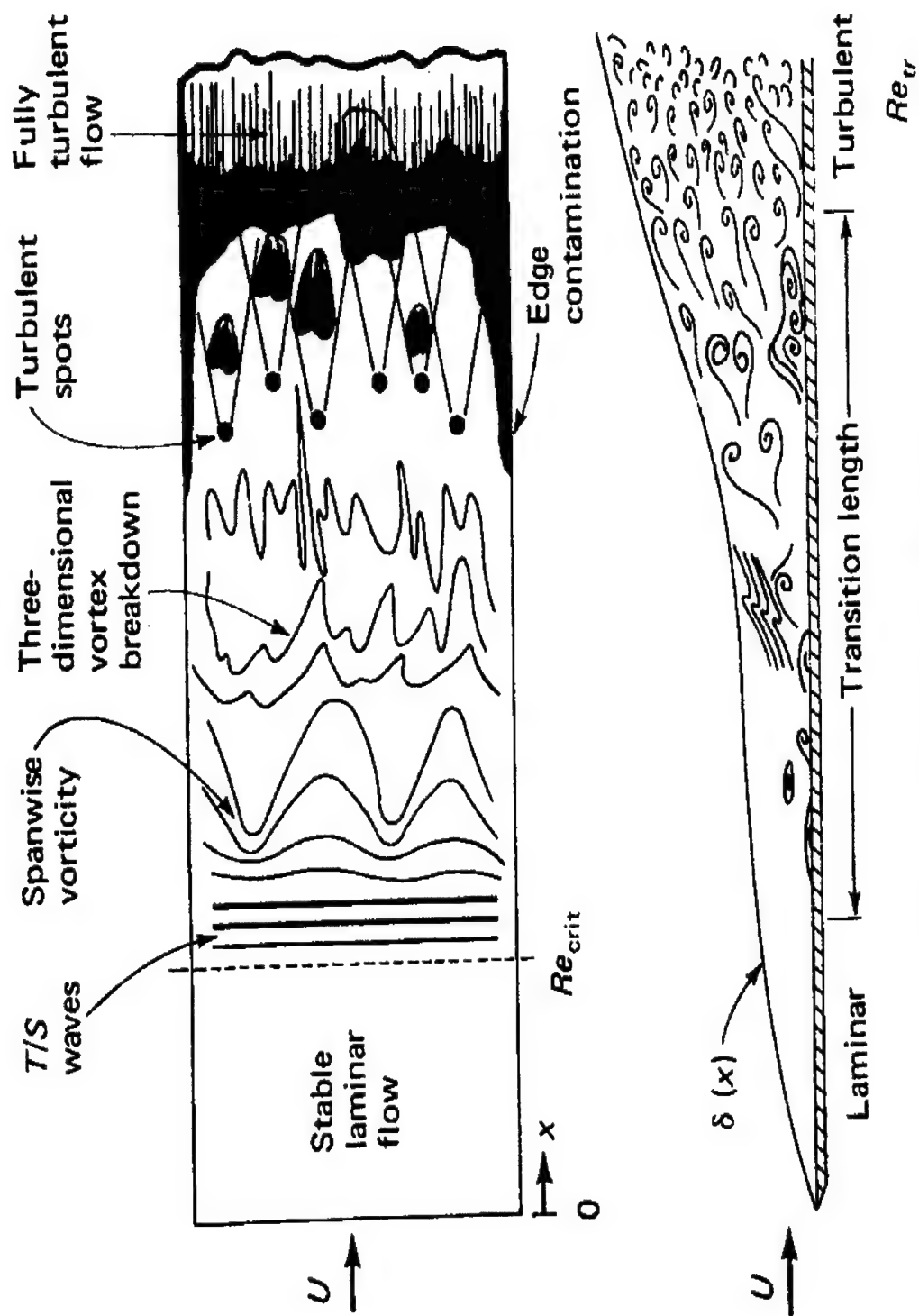


Figure 1.1. Transition Process (White, 1991)

Sym	Facility	M_δ	T_w/T_{aw}	θ_c , deg	Source	Method of Detection
○	VKF Range K	4.3	≈ 0.18	10	Potter (1969)	Shadowgraph - Schlieren
△	VKF Tunnel D (12 by 12 in.)	4.3	≈ 1.0	5	Pate (1971)	Schlieren
□	VKF Tunnel A (40 by 40 in.)	4.3	≈ 1.0	5	Pate (1971)	Surface Probe Peak Pressure Value Adjusted to Schlieren Location $(Re_t)_{schlieren} \approx$ $0.82 (Re_t)_{p,peak}$
---	PWT Tunnel 16S (16 by 16 ft)	4.3	≈ 1.0	5	Pate (1971)	Estimated Using $(Re_t)_{\delta}$ Correlation

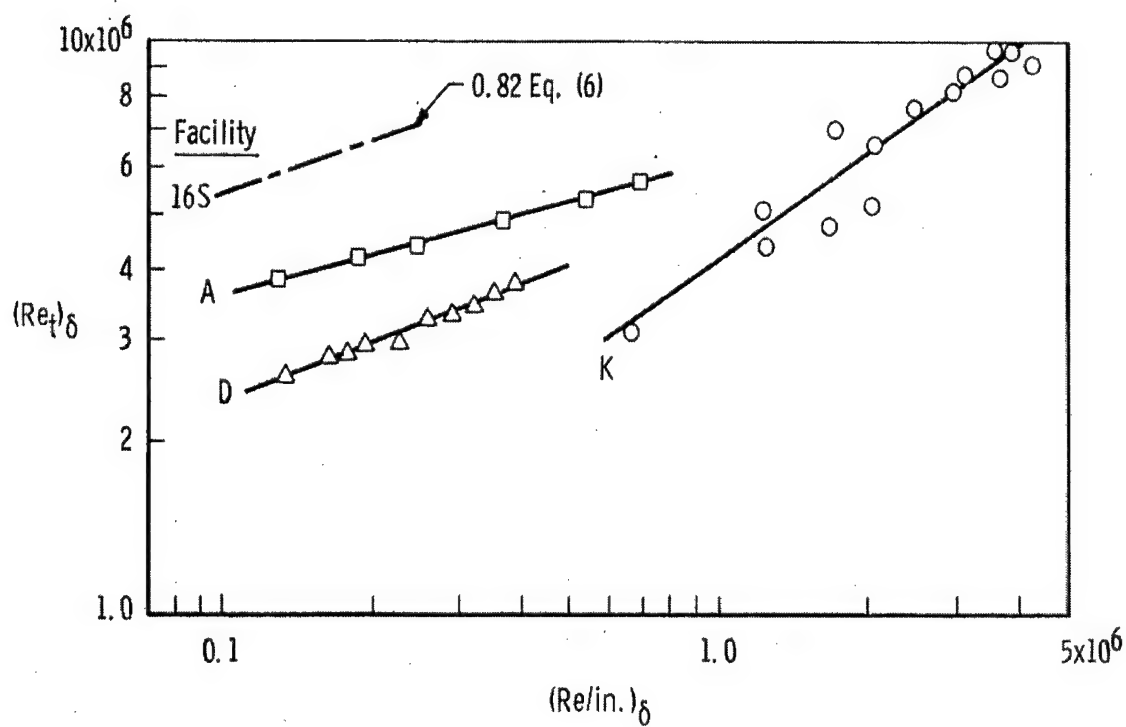


Figure 1.2. Comparison of Sharp Cone Transition Reynolds Numbers from Wind Tunnels and an Aeroballistic Range (Pate, 1971)

	<u>Model</u>	<u>Mach no.</u>	<u>Wind tunnel</u>
○	Cone	3.5	LaRC low disturb.
□	Flat plate	3.5	
---	Flat plate	3.0	AEDC
—	Flat plate	3.7	JPL 20 in.

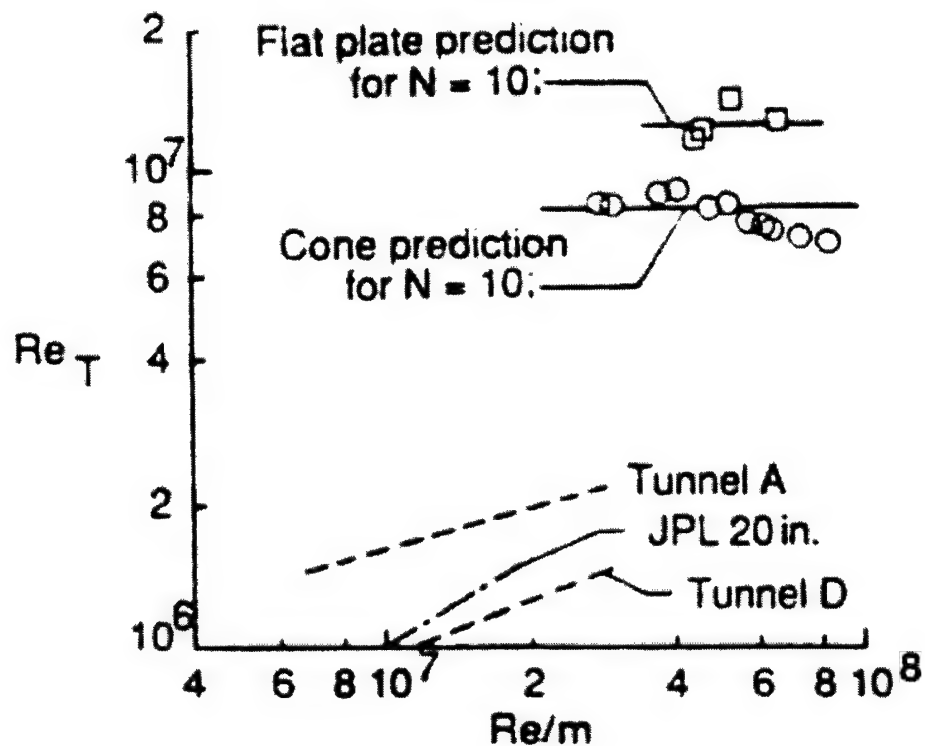


Figure 1.3. Comparison of Transition Onset Reynolds Numbers on a Cone and Flat Plate (Chen *et al.*, 1989)

CHAPTER 2

WIND TUNNEL EXPERIMENTS

2.1 Introduction

Wind tunnels with very low freestream disturbance levels comparable to free flight conditions are required for boundary layer stability and transition research and to ultimately provide reliable transition predictions for hypersonic flight vehicles. Numerical methods assume an ideal, noiseless flow (except for computational round-off errors) similar to that found in free flight. However, experimental high-speed flows in conventional wind tunnels generally have a measurable disturbance field at large unit Reynolds numbers. The high freestream disturbance levels in conventional wind tunnels can cause premature boundary layer transition on test models. Wind tunnels with very low comparable freestream disturbance levels, so called quiet tunnels, are therefore needed to obtain reliable transition experiment results.

The relationship of the freestream external disturbance field environment to the boundary layer disturbances that are ultimately responsible for transition are significant to the boundary layer transition problem (Reshotko, 1997). The disturbances in high speed wind tunnel flow are composed of three types: 1) velocity, or vortical disturbances, 2) temperature, or entropy disturbances, and 3) pressure, or acoustic disturbances (Pate and Schueler, 1969). Valve noise in the stagnation chamber and flow non-uniformities contribute to vorticity disturbances. Particles and temperature fluctuations in the flow within the stagnation chamber produce entropy disturbances. In most wind tunnels, vorticity and entropy disturbances are attenuated through the use of flow conditioning filters placed upstream of the stagnation chamber, and meshes and screens within the

stagnation chamber. Entropy disturbances are usually negligible downstream of the screens. Vorticity disturbances are further reduced by the large contraction ratio between the stagnation chamber and nozzle throat. Acoustic disturbances are the primary source of freestream disturbances in conventional high speed wind tunnels. These disturbances radiate along Mach lines from convecting eddies generated by the turbulent boundary layer on the nozzle wall, Figure 2.1a, and are wind tunnel specific. The acoustic disturbances interact with the boundary layer on the model and contribute to early transition. To reduce the amplitude of the acoustic disturbances, laminar boundary layer flow on the nozzle walls is desired.

The NASA Langley Research Center pioneered the development of the so-called quiet nozzle. The slow-expansion nozzle contour, obtained by inserting a radial-flow, straight-wall section upstream of the inflection point, extends the laminar boundary layer flow farther downstream. Therefore, the initiation of Görtler vortices is delayed until the beginning of the concave wall and the growth of Görtler vortices is decreased by the larger radii of curvature of the concave wall (Chen *et al*, 1993). A high-quality nozzle surface finish is essential to minimize the transition promoting effects of roughness, which can lead to early boundary layer transition and degrade nozzle performance. The Mach 6 quiet nozzle was incorporated into the Test Chamber Facility in the early 1990's. The freestream disturbance noise level in a quiet tunnel is further brought to low-levels by a number of features designed to maximize the region of laminar flow over the nozzle wall as shown in Figure 2.1b. High-density meshes and screens are used to attenuate vorticity and entropy disturbances in the settling chamber so that they are negligible in the test section. An annular boundary layer suction slot upstream of the nozzle throat is

used to bleed off the upstream turbulent boundary layer and initialize a new boundary layer on the downstream nozzle wall. As a result of the quiet wind tunnel modifications, laminar boundary layer flow is extended downstream on the nozzle walls and low freestream acoustic disturbance levels are achieved in the test section. A series of three hypersonic boundary layer stability experiments were performed; two of these experiments are studied in this work. Lachowicz and Chokani (1996) detailed the growth of disturbances on a flared-cone at zero degree angle of attack. Blanchard and Selby (1996) examined wall cooling on a flared-cone to describe the evolution of disturbances into a nearly turbulent flow. When taken together, these experiments provide the opportunity to examine the effect of an adverse pressure gradient and wall cooling on boundary layer stability. Throughout this chapter only the first author's name, Blanchard or Lachowicz, will be used to reference their experiments.

2.2 Mach 6 Axisymmetric Quiet Nozzle Facility

The Langley low disturbance tunnel is a small open-jet blow-down facility with a slow-expansion, axisymmetric, quiet, Mach 6 nozzle. Figure 2.2 shows the overall layout of the wind tunnel facility. The nozzle has a throat diameter of 1.00in, exit diameter of 7.49in and length from throat to exit of 39.76in. A tunnel stagnation temperature of $810^{\circ}R \pm 3^{\circ}R$, a total pressure of $130psia \pm 2psia$ and a free-stream Mach number is 5.91 ± 0.08 are used. These conditions correspond to a unit Reynolds number of $2.82 \times 10^6/ft$. At this Reynolds number, quiet flow exists over the majority of the model surface. The facility is first preheated, that is run in a subsonic mode with the models in place prior to

hypersonic testing. After preheat, the typical run times at hypersonic flow conditions are 30 to 60 minutes.

2.3 Models

Two flared cone configurations are examined in this work. Both models have a straight, 5° half-angle section that tangentially merges into a flared region. The stainless steel model surfaces are smooth with a less than $8 \times 10^{-6} \text{ in}$ surface finish; thus, roughness-induced transition effects are minimal. The tangent circular arc flare produces a nearly linear adverse pressure gradient, which results in measurable disturbance growth in the boundary layer over a short length (Wilkinson, 1997). Without the pressure gradient, transition would not have been attained within the limited quiet flow Reynolds number range of the facility (Beckwith, 1974). The flare curvature also maintains an approximately constant boundary layer thickness over the flare region, which allows second mode disturbances of nearly constant frequency to grow.

The model used by Blanchard (1996) consists of a 6 in straight portion followed by a 12 in outward flared region with a 91.44 in radius of curvature, Figure 2.3. This configuration is denoted as 91-6 referring respectively to the approximate radius of the circular flare arc and the location of the tangency point. The model is instrumented with 51 thermocouples along one ray of the cone and 30 pressure ports of diameter 0.020 in located 180° from the thermocouple ray. The cone has a wall thickness of 0.080 in and is equipped with internal passages for active surface cooling as shown in Figure 2.4. The cone tip is not cooled. Further details regarding the active cooling system are found in

Blanchard's report (1996). Adiabatic and cooled-wall (465 °R) temperature conditions are examined for the 91-6 model.

The cone model used by Lachowicz (1996) consists of a 10*in* straight portion followed by a 10*in* flared region with a 93.07*in* radius of curvature, denoted 93-10, and is shown in Figure 2.5. This cone-flare configuration results in a slightly smaller adverse pressure gradient applied over a smaller extent of the model than for the 91-6 model. Although Lachowicz examined nose bluntness effects, only the results obtained for the model with a sharp tip are examined in this research. The model is instrumented with 29 pressure orifices and 51 thermocouple gages placed along diametrically opposite rays. The skin thickness is 0.03*in* along the thermocouple ray and 0.06*in* elsewhere. The model is considered thin-skinned for the purpose of thermocouple measurements. Only adiabatic wall conditions are examined for the 93-10 model.

The relevant details of the model placement in the tunnel are shown in Figure 2.6. No universal pitch and yaw system existed for the wind tunnel, so both models were manually positioned at a nominally zero degree angle of attack. The aft 3.5*in* of the 93-10 and aft 3*in* of the 91-6 model extended downstream of the nozzle exit plane. Wilkinson (1997) and Lachowicz (1996) examined spectra of the freestream disturbances to which the models are exposed. Examination of the normalized hot-wire output for a probe in the centerline plane of the nozzle show a growing low frequency disturbance field radiating from the nozzle wall boundary layer, Figure 2.7. The radiated noise region intersects the models at roughly 13*in* (Wilkinson, 1997) to 14.25*in* (Lachowicz, 1996) from the sharp nose tip. Therefore, the first 13 to 14.25*in* of the models are located in a

quiet freestream flow environment. However, the entire lengths of the models were located within a region of uniform mean flow.

2.4 Measurements

Hot-wire anemometry is used to characterize the evolution of the pre-transitional boundary layer disturbances. Although the hot-wire yields only a single point measurement, and is intrusive, it is the preferred measurement technique in hypersonic stability experiments (Kendall, 1993). The hot-wire can sense a wide range of frequencies, and with a suitable calibration can yield fluctuations of two independent flow variables. The measurement principle of the hot-wire is based on the convective heat loss into the flow from the heated wire. An electric current heats the wire and the electrical resistance of the wire depends on its temperature

$$R_w = R_{ref} [1 + \alpha(T_w - T_{ref})] \quad (2.4.1)$$

where α is the temperature coefficient of resistivity. The heat transfer (and hence incident flow) may be inferred from the wire's resistance.

Constant-current (CCA) and constant-temperature (CTA) hot-wire anemometers have long been used in the study of fluid flows. The CCA was used by Stetson *et al* in their experiments, which were conducted in conventional wind tunnels (1983, 1984, 1986, 1989). The CCA is laborious to use and must be adjusted for any change in wire temperature, velocity or external temperature. Additionally, both the CTA and CCA have deficiencies with respect to signal-to-noise ratio and sensitivity at the high frequencies that are characteristic of hypersonic boundary layers. Lachowicz reported that no measurable signals could be obtained in the Mach 6 tunnel using the CCA or CTA

(1996). A hot-wire operated by a constant voltage anemometer (CVA) was used by Lachowicz (1996) and Blanchard (1996). Sarma conceived the CVA to provide an anemometer system without the shortcomings of the CCA and CTA systems (1998). At the time of the experiments the CVA was a newly developed instrument, and thus the understanding of its behavior was limited (Wilkinson, 1997). However, the CVA was the only anemometer that was insensitive to the electromagnetic interference that emanated from the electric arc heaters of the Mach 6 facility. Furthermore, unlike the CTA and the CCA, the constant voltage anemometer's operation was unaffected by the long cable lengths between the hot-wire, located in the tunnel, and anemometer, located in the test cell.

The basic CVA circuit is shown in Figure 2.8. Its three basic elements are 1) a stable, low noise, DC power supply; 2) an operational amplifier; and 3) a T-resistor network. The voltage, V_w , at the center node of the T-resistor network is constant and independent of the value of the wire resistance. A change in wire resistance due to a change in the convective heat conditions results in a change in the wire current. This change in current is measured as a change in the output voltage, V_s , of the CVA. The resistor R_2 provides the proportionality constant between the wire current and output voltage. If this resistance is large, a small change in wire current is translated into a large change in the output of the CVA.

In a hypersonic flow, the hot-wire operated by a CCA, CTA or CVA responds to a mixed mode, that has both mass flux and total temperature components:

$$\frac{\Delta e}{e} = S_{\rho u} \frac{\Delta \rho u}{\rho u} + S_{T_o} \frac{\Delta T_o}{T_o} \quad (2.4.2)$$

The sensitivity coefficients are known to be a function of the mean flow (Morkovin, 1956) and are determined through hot-wire calibration. Lachowicz *et al* (1996) observed that similar to the CCA and CTA, the CVA is more sensitive to mass flux when the hot-wire is operated in high overheat mode and more sensitive to total temperature when the hot-wire is operated in low overheat mode.

In linear stability theory, all flow variables of a perturbation are assumed to grow or decay in the same manner. Kimmel and Kendall (1991) stated that in the linear growth region, the amplification rate can be determined from the logarithmic growth or decay of the voltage fluctuation. Kimmel (2001) observes that if the mean flow does not vary greatly then the hot-film probe sensitivities do not change greatly. Similarly, Lachowicz (1996) stated that for the CVA, the changes in the wire sensitivity due to changes in the mean flow should be small relative to the exponential growth of the disturbances. In the absence of an independent measurement, it is of interest to examine if the changes in mean flow are small in the experiments of Blanchard (1996) and Lachowicz (1996).

In Blanchard's experiment (1996), the CVA is operated in a constant high overheat mode such that the hot-wire is primarily sensitive to mass flux fluctuations and minimally sensitive to total temperature fluctuations. Uncalibrated hot-wire data are obtained and thus, the amplification rate can be determined, but the fluctuating voltages cannot be decomposed into mass flux and total temperature fluctuations. For Lachowicz's study (1996), the majority of the hot-wire measurements were also uncalibrated. However, a calibration was performed for the hot-wires used to obtain the freestream measurements. The primary purpose of this calibration was to measure mean mass flux and mean total temperature profiles through the boundary layer at various

streamwise locations. A second objective was to obtain root mean square (RMS) mass flux and RMS total temperature profiles to quantify the nature of the boundary layer disturbances. Lachowicz's wire calibration is assessed in this work. For more details on the calibration procedure, see Lachowicz's report (1996).

The hot-wire probe used in the experimental measurements is shown in Figure 2.9. A 0.0001in diameter platinum-rhodium (10%) wire spot welded between the ends of two needle broaches was the sensing element. A small distance beneath the wire, a needle broach was attached to determine when the probe contacted the model wall. Hot-wire measurements were obtained at 31 streamwise stations over the range $9.0\text{in} \leq x \leq 16.5\text{in}$ on the 91-6 model afterbody at 0.25in increments. For the 93-10 model, hot-wire measurements were obtained at 0.5in increments over the range $10.97\text{in} \leq x \leq 14.97\text{in}$ and at 0.25in increments over $14.97\text{in} \leq x \leq 18.97\text{in}$. For both cases, x is measured with respect to the tip of the model. Further details about the traversing and data acquisition systems are available in (Blanchard, 1996) and (Lachowicz, 1996).

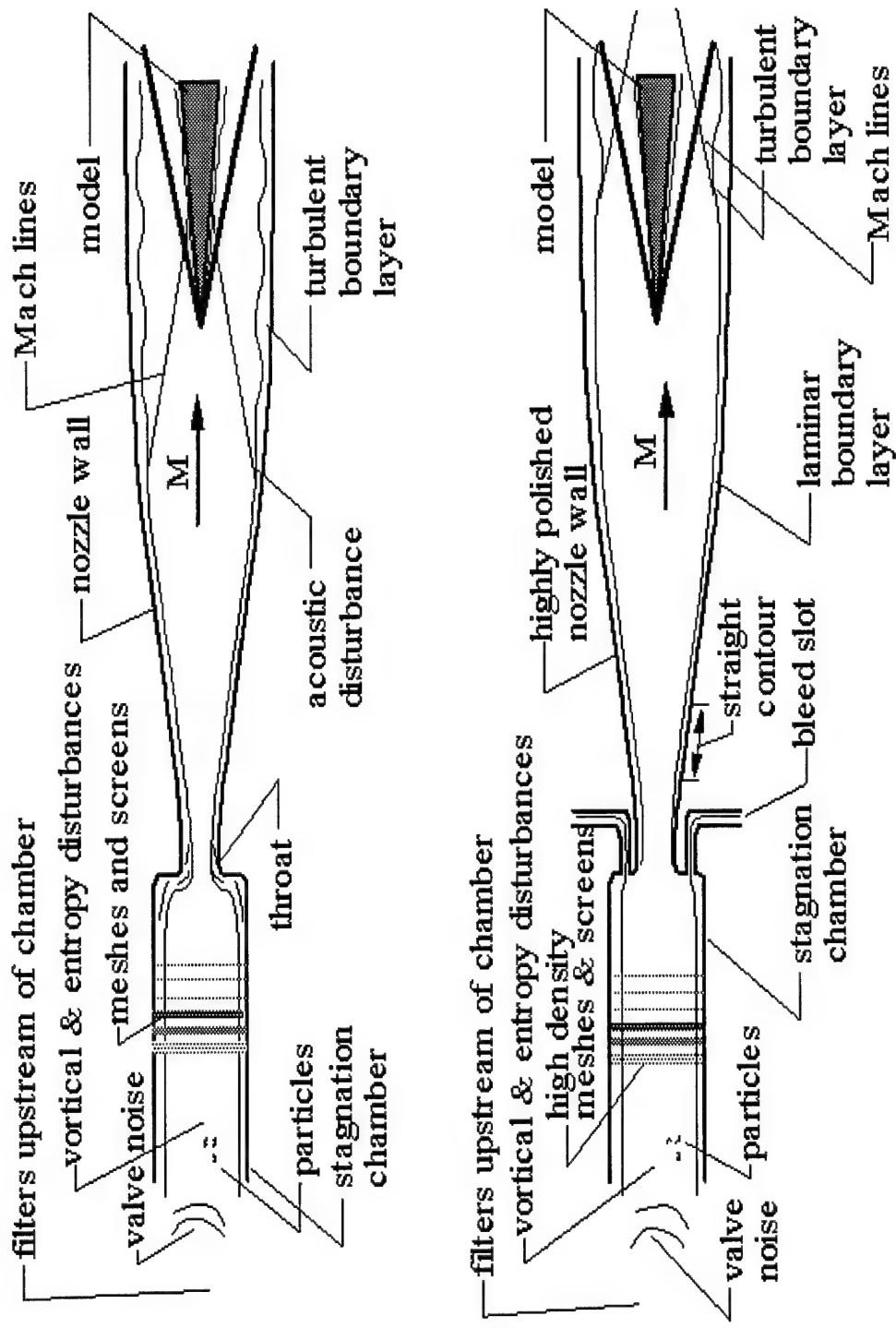


Figure 2.1. a) Disturbances in a Conventional Wind Tunnel; b) Quiet Wind Tunnel Design (Lachowicz, 1996)

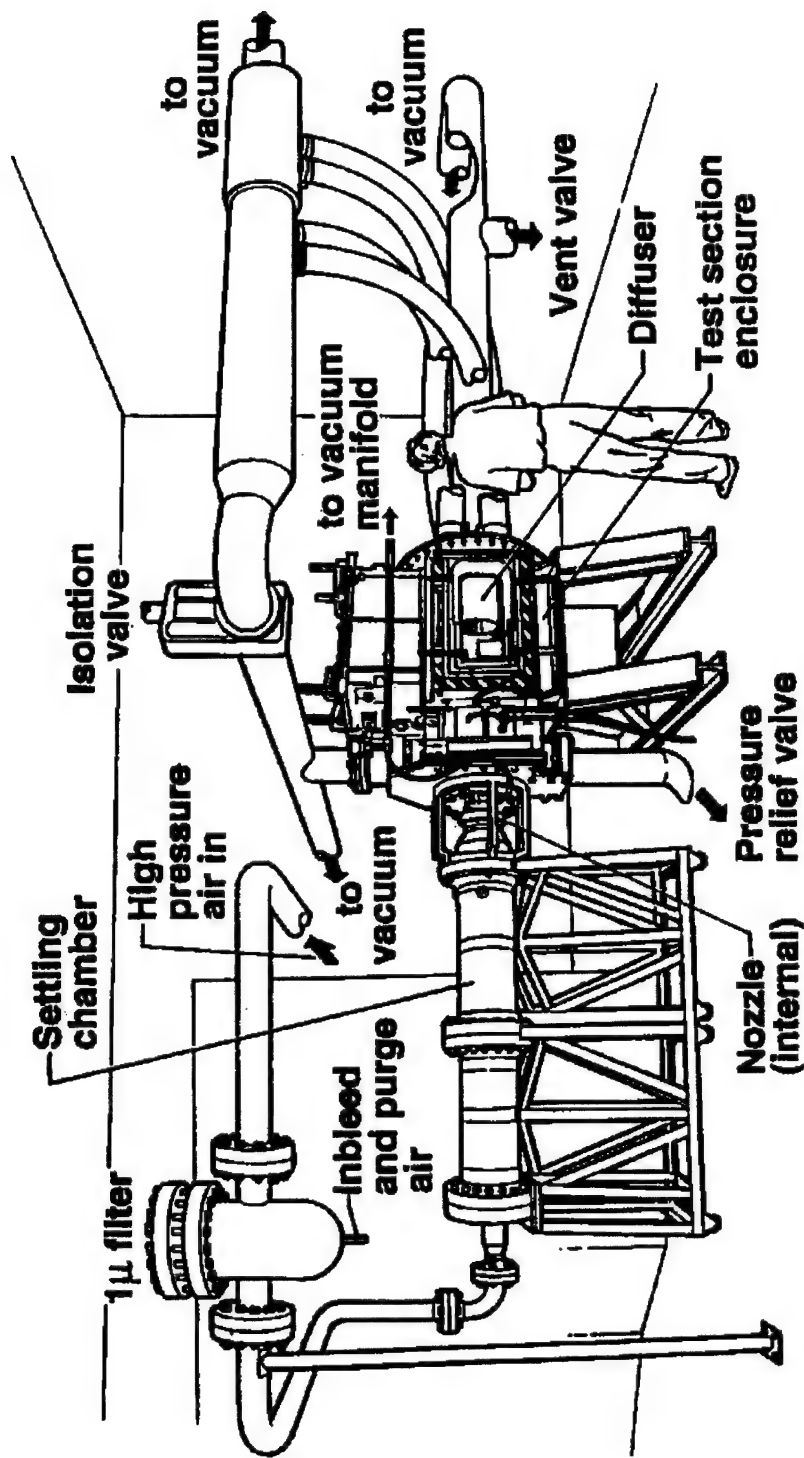


Figure 2.2. NASA Langley Quiet Wind Tunnel Facility

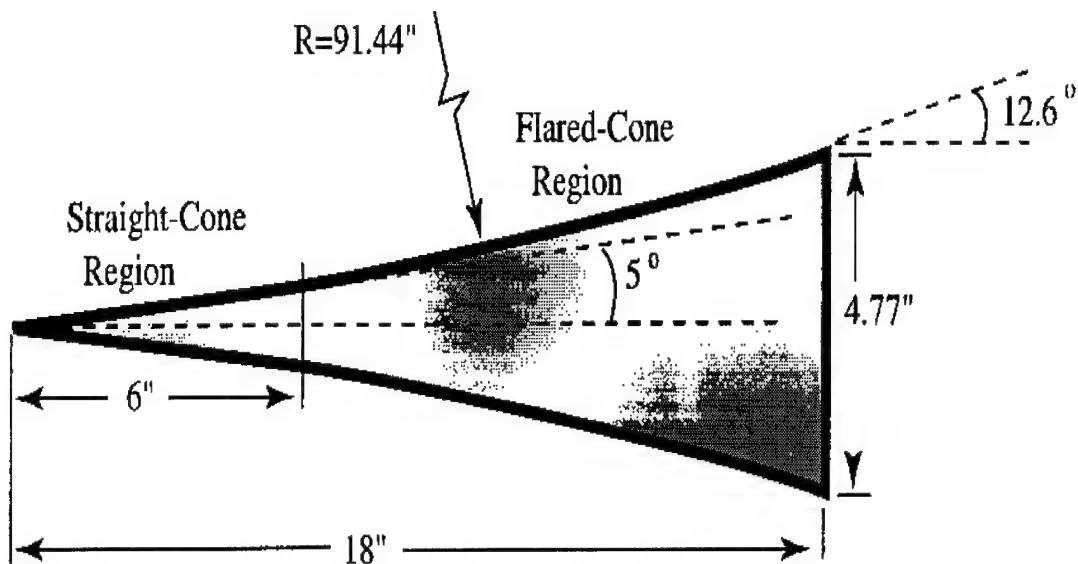


Figure 2.3. 91-6 Cone-Flare Model and Dimensions

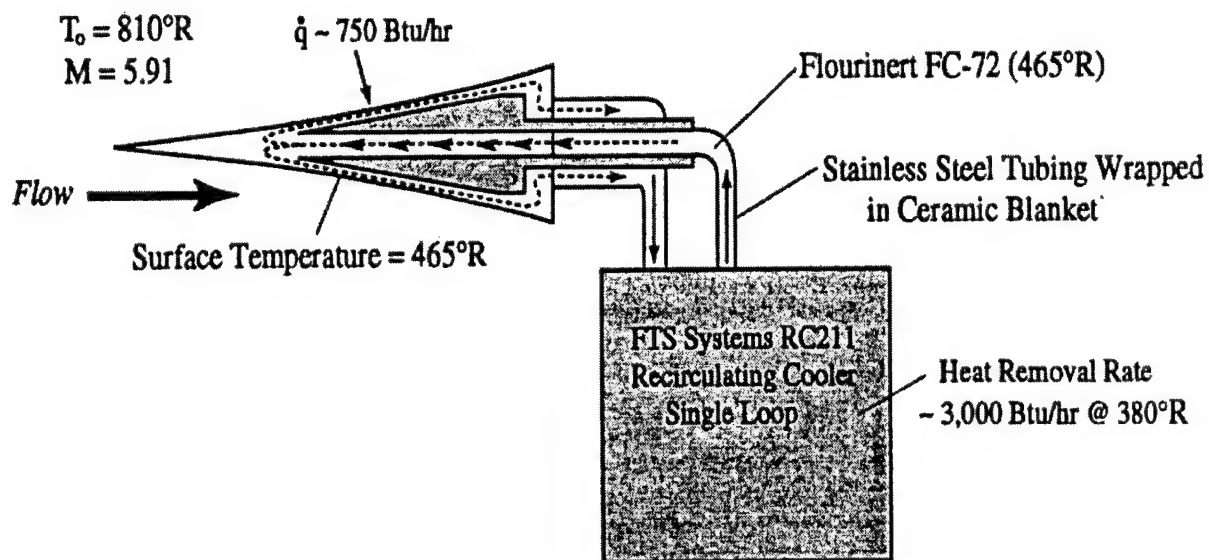


Figure 2.4. Active Cooling System for 91-6 Cooled Cone (Blanchard & Selby, 1996)

$R=0.00010, 0.03125, 0.06250, 0.09375, 0.12500$
 $D=\text{sharp}, 0.32730, 0.65460, 0.98190, 1.30920$

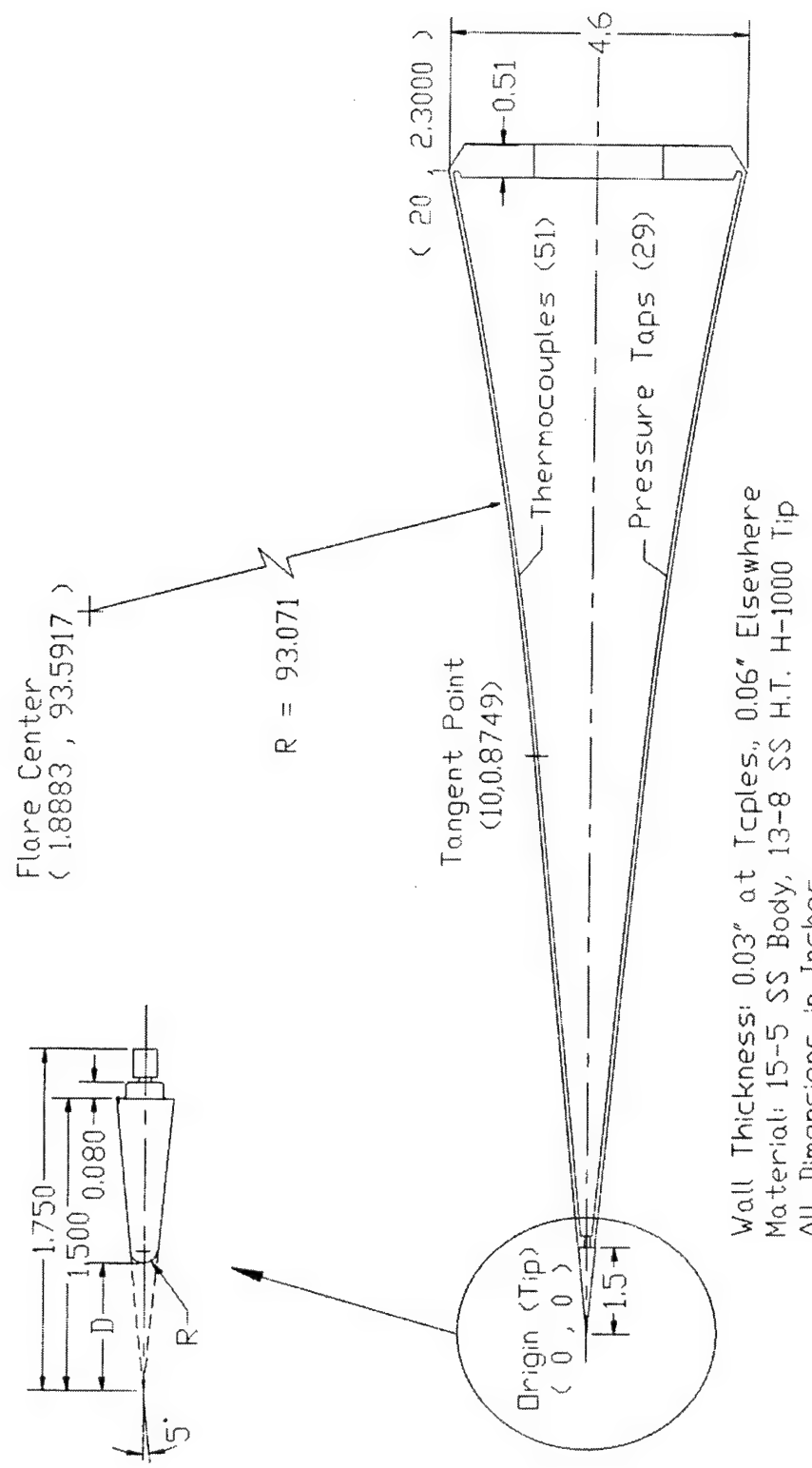


Figure 2.5. 93-10 Cone-Flare Model and Dimensions

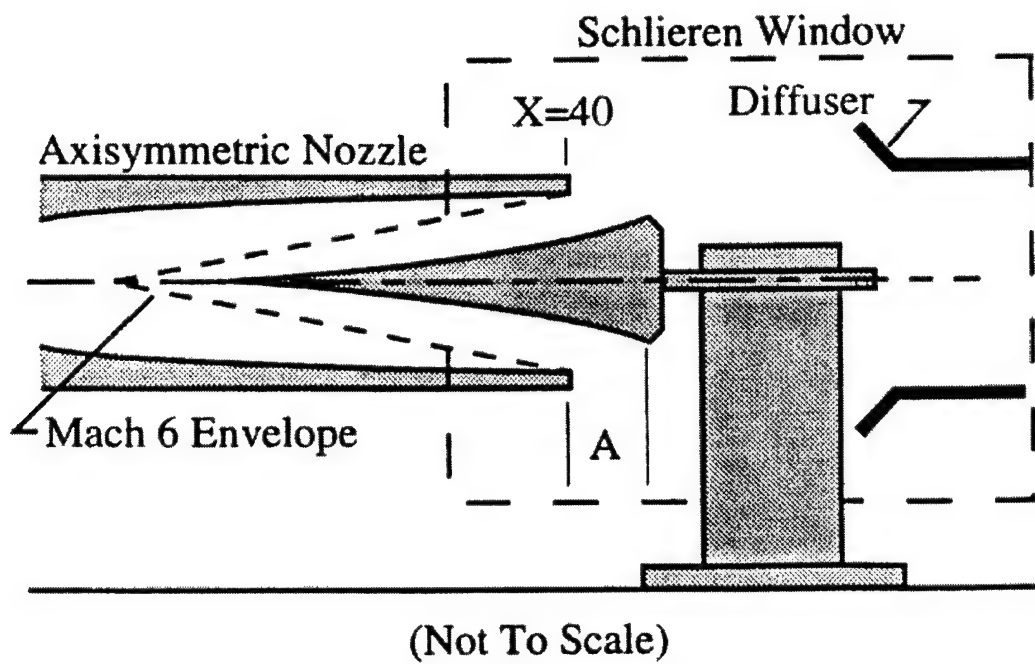


Figure 2.6. Placement of Flared Cone Models in Wind Tunnel; $A=3"$ for 91-6 Model, $A=3.5"$ for 93-10 Model (Wilkinson, 1997)

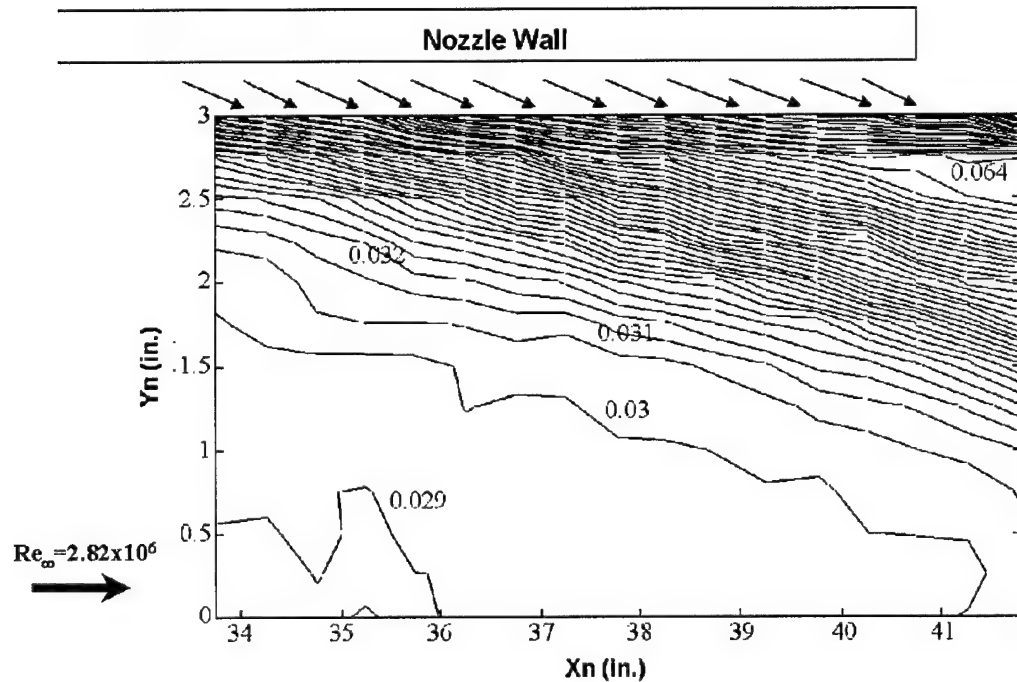


Figure 2.7. Freestream RMS Contours; Contour Increment=0.001 (Lachowicz, 1996)

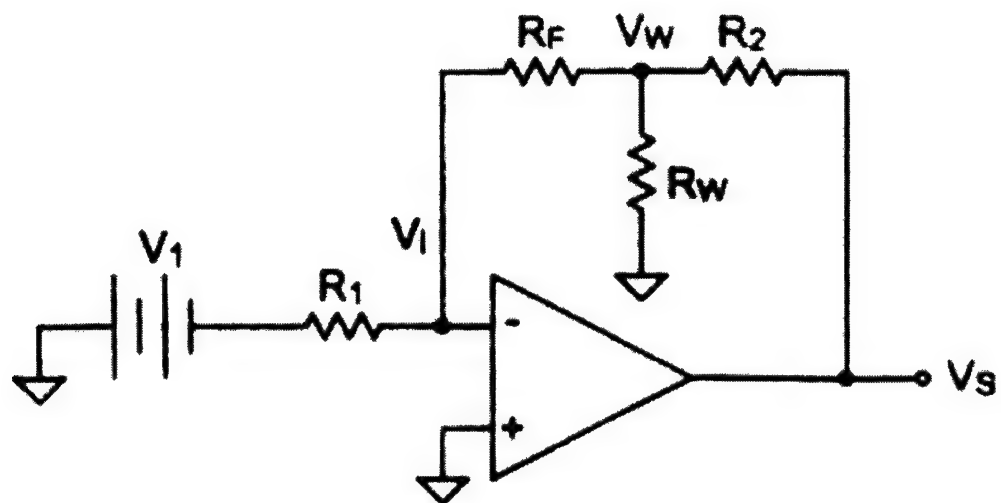


Figure 2.8. Constant Voltage Anemometer Circuit (Sarma, 1998)

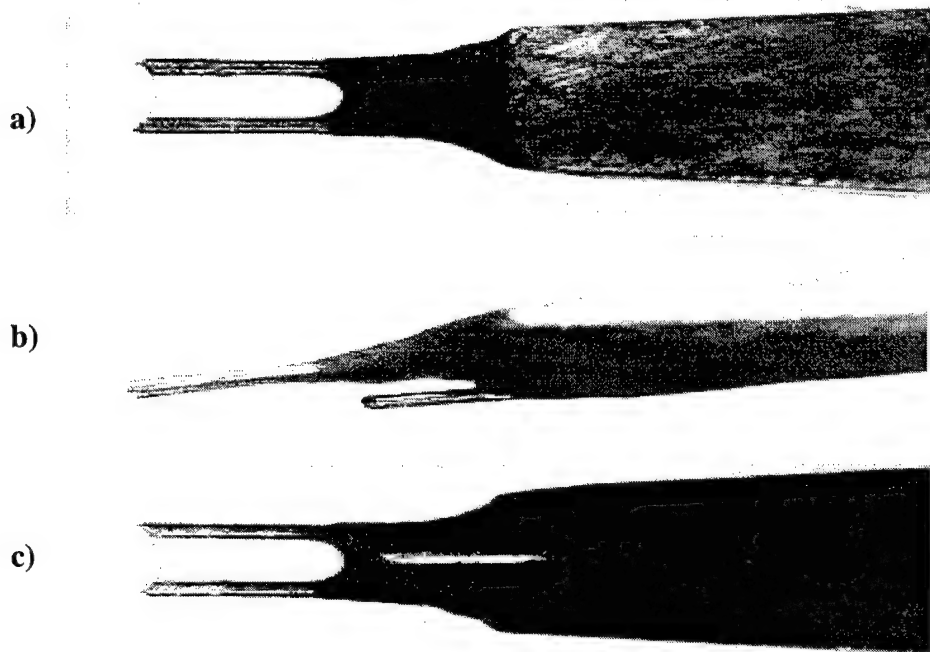


Figure 2.9. Hot-Wire Probe, a) top view; b) side view; c) bottom view

CHAPTER 3

NUMERICAL METHOD

3.1 Introduction

The numerical procedure for this work consists of two parts: calculation of a mean flow solution and linear stability analysis. The smoothness of the mean flow variables in the wall-normal direction has a great influence on the unstable stability modes (Iyer, 1991). Smooth profiles of the first and second derivatives of velocity and temperature must be obtained on a well resolved grid for linear stability analysis to accurately capture instabilities in the flow. Thus, a grid refinement study is conducted to develop a computational grid for which adequate boundary layer resolution and convergence to a smooth solution is assured for the mean flow. Criteria for the grid refinement study include assuring that enough grid points are located in the boundary layer to adequately resolve the mean flow. The mean flow solution is then post-processed and used in the linear stability analysis.

Linear stability theory is derived from the equations governing the mean flow by modeling the instantaneous flow as a mean component plus fluctuating disturbance. All quantities making up the fluctuation are assumed to grow or decay at the same rate. Assumptions of linearity and parallel flow are employed in the derivation of the linear stability equations to allow computational efficiency. These assumptions, however, do have their limitations. Linearity assumes that there are no interactions between the disturbances. The fluctuating disturbances are assumed small relative to the mean components such that the high order fluctuating terms are negligible. Thus, the linear stability equations only predict the second mode and do not predict any higher mode

disturbances. Locally parallel flow assumes that the mean flow only varies normal to the surface, which permits a normal mode solution. The parallel flow assumption is valid for small boundary layer growth over a wavelength. Additionally, the model surface is assumed smooth, and no freestream disturbances are assumed present. All of these conditions are to a large extent met in the quiet wind tunnel experiments analyzed in this work.

3.2 Grid Generation

The grid generation was conducted using the commercially available *Gridgen* software package (1997). A representative grid is shown in Figure 3.1; for the sake of clarity, only every 4th grid point is shown in the streamwise and surface-normal directions. In the streamwise direction, grid points are spaced equally between the model tip and base. A one-sided, geometric progression spacing algorithm is used in the surface-normal direction and the minimum spacing is specified at the wall. Geometric spacing is used in the surface-normal direction because it produces smoother metrics in the boundary layer (Garriz *et al*, 1994). The geometric progression algorithm distributes the grid points from the wall upward in the surface-normal direction such that the ratio of spacing between adjacent grid points is constant. A break point is inserted at the approximate boundary layer height above the wall in the η -direction on the farfield boundary. The number of points between the wall and the break point are specified. Then, grid spacing is specified from the wall to the break point and from the break point to the top of the grid in the η -direction. Using the break point allows the number of points located within the approximate boundary layer height to be specified. A standard

transfinite interpolation algebraic method is used to generate the grid. This method applies blending functions based on the relative spacing of the grid points independently to the (x, y) coordinates of the flow.

3.3 Mean Flow Analysis

The governing equations of interest for the present work are the axisymmetric compressible Navier-Stokes equations. These equations, written in strong conservation-law form in the Cartesian coordinate system are given by

$$\frac{\partial \mathbf{U}}{\partial t} + \frac{\partial \mathbf{E}}{\partial x} + \frac{\partial \mathbf{F}}{\partial y} = \mathbf{S}, \quad (3.3.1)$$

where x is in the streamwise direction and y is in the streamwise normal direction. The vector of conserved variables is composed of the density, momentum in the x - and y -directions and the total energy and is given by

$$\mathbf{U} = \frac{y}{J} \begin{pmatrix} \rho \\ \rho u \\ \rho v \\ E_t \end{pmatrix} \quad (3.3.2)$$

\mathbf{E} and \mathbf{F} are the flux vectors in the x - and y -directions respectively (Tannehill, 1997). For example:

$$\mathbf{E} = \begin{pmatrix} \rho u \\ \rho u^2 + p + \tau_{xx} \\ \rho u v - \tau_{xy} \\ (E_t + p)u - u\tau_{xx} - v\tau_{xy} + q_x \end{pmatrix} \quad (3.3.3)$$

\mathbf{S} is the source vector.

Equations (3.3.1) may be written for a curvilinear coordinate system (ξ, η) according to the following transformation with respect to a Cartesian coordinate system:

$$\begin{aligned}\xi &= \xi(x, y) \\ \eta &= \eta(x, y)\end{aligned}\quad (3.3.4)$$

The Navier-Stokes equations can be written in strong conservation law form using curvilinear, axisymmetric coordinates as

$$\frac{\partial U}{\partial t} + \frac{\partial (E_I - E_V)}{\partial \xi} + \frac{\partial (F_I - F_V)}{\partial \eta} = S \quad (3.3.5)$$

The inviscid flux vectors are given by

$$\mathbf{E}_I = \frac{y}{J} \begin{pmatrix} \rho U_c \\ \rho u U_c + \xi_x p \\ \rho v U_c + \xi_y p \\ (E_t + p) U_c \end{pmatrix}, \quad (3.3.6)$$

and

$$\mathbf{F}_I = \frac{y}{J} \begin{pmatrix} \rho V_c \\ \rho u V_c + \eta_x p \\ \rho v V_c + \eta_y p \\ (E_t + p) V_c \end{pmatrix} \quad (3.3.7)$$

The viscous flux vectors are given by

$$\mathbf{E}_V = \frac{y}{J} \begin{pmatrix} 0 \\ \xi_x \tau_{xx} + \xi_y \tau_{xy} \\ \xi_x \tau_{xy} + \xi_y \tau_{yy} \\ \xi_y (u \tau_{xx} + v \tau_{xy} + q_x) + \xi_x (u \tau_{xy} + v \tau_{yy} + q_y) \end{pmatrix}, \quad (3.3.8)$$

and

$$\mathbf{F}_V = \frac{y}{J} \begin{pmatrix} 0 \\ \eta_x \tau_{xx} + \eta_y \tau_{xy} \\ \eta_x \tau_{xy} + \eta_y \tau_{yy} \\ \eta_y (u \tau_{xx} + v \tau_{xy} + q_x) + \eta_x (u \tau_{xy} + v \tau_{yy} + q_y) \end{pmatrix} \quad (3.3.9)$$

The source vector arising from the axisymmetric transformation is given by

$$\mathbf{S} = \frac{1}{J} \begin{pmatrix} 0 \\ 0 \\ p - \tau_{\theta\theta} \\ 0 \end{pmatrix} \quad (3.3.10)$$

The contravariant velocity components, are given by

$$U_c \equiv \xi_x u + \xi_y v, \quad V_c \equiv \eta_x u + \eta_y v \quad (3.3.11)$$

The perfect gas expressions

$$p = (\gamma - 1) \rho e, \quad (3.3.12)$$

and

$$E_t = \rho \left(e + \frac{1}{2} (u^2 + v^2) \right), \quad (3.3.13)$$

are used in conjunction with Sutherland's law for molecular viscosity to close the Navier-Stokes system. The transformed forms for the stress and heat flux terms are found in Tannehill (1997).

The Navier-Stokes equations are marched in time, using a nonlinear line Gauss-Seidel approach (Edwards, 1993). An implicit full multigrid/full-approximation-storage technique is used to accelerate the convergence to a steady state (Edwards, 1994). The inviscid components of the Navier-Stokes set are discretized using an upwind scheme. A high resolution, low-diffusion flux-splitting approach is employed, which combines the accuracy of flux-difference splitting in the capturing of shear layers with the robustness of flux-vector splittings (Edwards, 1995). In this approach, the inviscid flux at a cell interface is split into a convective contribution, which is upwinded in the direction of the flow, and a pressure contribution, which is upwinded based on acoustic considerations. The monotone capturing of strong oblique shock waves that are not aligned with a mesh line is accomplished by constraining the cell interfaces to behave as a stationary contact discontinuity for vanishing numerical diffusion. The upwind scheme is second order accurate. The viscous components of the Navier-Stokes equations are central-differenced to second order accuracy.

At the cone wall, no slip boundary conditions are applied; in addition either adiabatic or isothermal wall conditions are applied. At the top boundary, freestream conditions are imposed and a zero-gradient condition is imposed on all variables. Supersonic boundary conditions are applied at the inflow and outflow boundaries. Freestream supersonic conditions are applied at the inflow and first order supersonic characteristic boundary conditions are imposed at the outflow. Figure 3.2 shows the convergence history for a typical grid examined. The residual drops by ten orders of magnitude, and the result is fully converged. The run time is less than five minutes of CPU.

3.4 Grid Refinement Study

Stability analysis requires an accurate mean flow resolved on a grid that is fine enough to capture the essential physical aspects of the flow. Balakumar and Malik (1994) noted that stability analysis depends heavily on the accurate computation of the first and second derivatives of mean velocity and temperature profiles. Furthermore, they stated that the grid points inside the boundary layer should be distributed such that the peak in the second derivatives is adequately resolved. A grid refinement study was conducted to assess the sensitivity of the mean flow to the overall grid dimensions and grid clustering within the boundary layer. Evaluation criteria included using enough grid points within the boundary layer such that the mean flow profiles are smooth and that the generalized inflection point and boundary layer thickness are resolved. The discussion that follows pertains to the 91-6 cone. Once the optimal grid was determined for the 91-6 cone, similar grid dimensions and spacings were used for the 93-10 cone.

First, the effect of grid spacing in the streamwise direction is examined. The computed mean flows with 481 and 241 points in the streamwise direction are identical; thus, 241 points in the streamwise direction are used in the grid refinement study. Next, the number of grid points and grid spacing in the surface-normal direction is examined. The minimum and maximum surface-normal spacing at the cone tip ($x=0''$) and base ($x=18''$) are summarized in Table 3.1. The results of the adiabatic wall mean flow calculation obtained for the four cases presented in Table 3.1 are discussed below.

Figures 3.3 and 3.4 show the mean velocity and temperature profiles at $x = 9''$ for the four grid cases. All of the profiles are very smooth and show good agreement over the height of the boundary layer. Over the outer portion of the boundary layer, the results of cases 1 and 2 differ little from the more refined grids. The profiles of the first derivative in velocity and temperature are shown in Figures 3.5 and 3.6 at $x=9''$. These profiles accentuate the differences in the velocity and temperature profiles over the outer portion of the boundary layer and are smooth for all cases. The profiles for cases 3 and 4 are in very good agreement and show no anomalies. Figure 3.7 shows the generalized inflection point profile at $x = 9''$; the generalized inflection point is a measure of the angular momentum, and generally occurs near the edge of the boundary layer for a hypersonic flow. The computed results for cases 3 and 4 are again in very good agreement. For cases 1 and 2, it appears that too few points were located in the boundary layer to fully resolve the peak of the generalized inflection point.

Figure 3.8 compares the predicted boundary layer thickness with the experimentally determined boundary layer thickness. The four cases show the same general trend for the boundary layer thickness, however case 4 is in best agreement with

the experimental data. Overall the assessment of the mean flow profiles within the boundary layer and the comparisons with the available experimental data show that the mean flow solutions obtained on the 241×225 grid of case 4 are optimum.

The dimensions used for the 93-10 grid are described in Table 3.2. Due to convergence limitations for the mean flow code, fewer grid points inside the boundary layer were used. However, the grid spacing was adequate to capture the necessary features of the flow.

3.5 Linear Stability Analysis

Linear stability analysis is performed using a quasi-parallel, spatial stability theory code written by Hudson (1996). The code is used for stability analysis in two- and three-dimensional perfect gas flows and models first- and second-mode T-S disturbances. To formulate the linear stability equations, each flow variable is first separated into mean and fluctuating components

$$\begin{aligned} u &= \bar{U} + u', & v &= \bar{V} + v', & w &= \bar{W} + w', & p &= \bar{P} + p', \\ \rho &= \bar{\rho} + \rho', & T &= \bar{T} + T', & \mu &= \bar{\mu} + \mu', & k &= \bar{k} + k' \end{aligned} \quad (3.5.1)$$

Equations (3.5.1) are substituted into the governing equations, Equations (3.3.1), and the resulting equations are linearized. The mean flow is then subtracted from the linearized equations. A quasi-parallel flow assumption is imposed such that the mean flow quantities at a given location depend only on the surface-normal distance from the wall. The assumption that the fluctuating quantities are given by small amplitude harmonic waveforms yields the following equation

$$q'(\xi, \eta, \zeta, t) = \hat{q}(\eta) \exp [i(\alpha\xi + \beta\zeta - \omega t)] \quad (3.5.2)$$

The spatial growth of a two-dimensional disturbance is examined such that the frequency is real, the streamwise wavenumber is complex, and the spanwise wavenumber is zero. Substituting Equation (3.5.2) in Equation (3.3.1) for the fluctuating quantities, it can be shown that the linear disturbances satisfy the following system of ordinary differential equations

$$\left(\mathbf{A} \frac{d^2}{dy^2} + \mathbf{B} \frac{d}{dy} + \mathbf{C} \right) \boldsymbol{\phi} = 0, \quad (3.5.3)$$

where \mathbf{A} , \mathbf{B} , and \mathbf{C} are 5×5 matrices whose nonzero elements are given in Malik (1990) and

$$\boldsymbol{\phi} = (u', v', p', T', w')^T \quad (3.5.4)$$

The compressible linear stability equations are solved using a boundary value method, which is able to yield eigenvalues when no knowledge of the instability is available (Malik, 1990).

Stability analysis requires boundary conditions for the disturbances at the wall and in the freestream. A no-slip wall is assumed such that the velocity fluctuations are zero at the cone surface. The temperature fluctuations are also assumed to be zero at the wall due to the thermal inertia of the cone. As a result of hypersonic flow over the cone surface, a shock forms between the boundary layer and the freestream. This shock is assumed far away from the boundary layer and thus has little effect of stability (Hudson, 1996). All velocity disturbances except the y -direction and temperature disturbances are assumed to be zero in the freestream (Malik, 1990). Thus, the boundary conditions are given by:

$$\begin{aligned} u' &= v' = T' = w' = 0 \text{ at } y = 0, \\ u' &= T' = w' = 0 \text{ at } y = \infty \end{aligned} \quad (3.5.5)$$

The pressure is calculated using the momentum equation.

The numerical methods used to solve the eigenvalue problem depend on the availability of an initial eigenvalue guess (Malik, 1992). When no guess is available, the “global” approach is employed. The global method uses second order accurate central differences to approximate the first and second derivatives in Equation 3.5.3. The global calculation results in a spectrum of eigenvalues, which is then filtered to determine the most unstable eigenvalue. The “local” approach is then used to improve upon the approximate eigenvalue obtained from the global method. For the local method, a fourth order accurate finite difference scheme is used to approximate the first and second derivatives in Equation 3.5.3; a second order accurate difference is used at the boundaries. The local method is also used if an initial eigenvalue guess is specified; in this case, the global solution method is not employed. For calculations involving successive frequencies, the improved eigenvalue obtained from the local method for the first frequency is used as the initial guess in the local method for the next frequency calculation. Thus, the global method is only employed for the first frequency in the series of frequency calculations. The global solution method is more computationally expensive than the local method. However, global methods are valuable for hypersonic boundary layer stability problems since several modes can lie close together and an extremely good initial eigenvalue guess is needed for the local method to converge. The run time for a global and local solution for one frequency is less than two minutes of CPU.

The e^N prediction criterion is coupled with the stability analysis results to determine the location of transition onset. The N -factor indicates the amplification of disturbances and is based on a correlation of experimental data. Since the e^N method is

based on stability theory, it addresses the physics of the flow and is more reliable than empirical relations. Reshotko (1997) classifies the e^N method as a reliable index of transition behavior for two dimensional and axisymmetric configurations. The strength of the e^N method lies in its flexibility, as it is possible to compare the transition behavior of various vehicles without specific knowledge of environmental distributions.

The amplitude growth of constant frequency disturbances leads to the e^N method. Transition can be evaluated by examining the amplification rates and determining the fastest growing disturbance. The onset of boundary layer transition is predicted by computing the amplitude ratio at the frequency that is growing fastest overall. Thus,

$$e^N = \frac{A}{A_o} = \exp \int_{x_o}^x \left(\frac{1}{A} \frac{dA}{dx} \right) dx \text{ or } N = \int_{x_o}^x \alpha_i dx \quad (3.5.6)$$

The integration is performed at a constant physical frequency. Transition onset is the location where the integrated amplification rate from the neutral point is 10, or the amplitude of the disturbance has increased by a factor of e^{10} (22,026) from the neutral point.

Table 3.1. Case Descriptions for 91-6 Model Grid Refinement Study

Case	Number of Points in Boundary Layer	I × J	Grid Spacing			
			$x=0''$		$x=18''$	
			$\eta_{\min} \times 10^{-6}$	$\eta_{\max} \times 10^{-4}$	$\eta_{\min} \times 10^{-5}$	$\eta_{\max} \times 10^{-3}$
1	40	241×145	9.93	9.80	9.60	9.70
2	45	241×225	9.99	2.10	8.80	1.29
3	90	241×225	9.89	2.10	0.90	2.48
4	105	241×225	9.77	2.12	0.90	5.39

Table 3.2 Grid Spacing for 93-10 Model

Number of Points in Boundary Layer	I × J	Grid Spacing			
		$x=0''$		$x=20''$	
		$\eta_{\min} \times 10^{-7}$	$\eta_{\max} \times 10^{-4}$	$\eta_{\min} \times 10^{-5}$	$\eta_{\max} \times 10^{-3}$
85	241×225	9.91	3.88	4.90	4.53

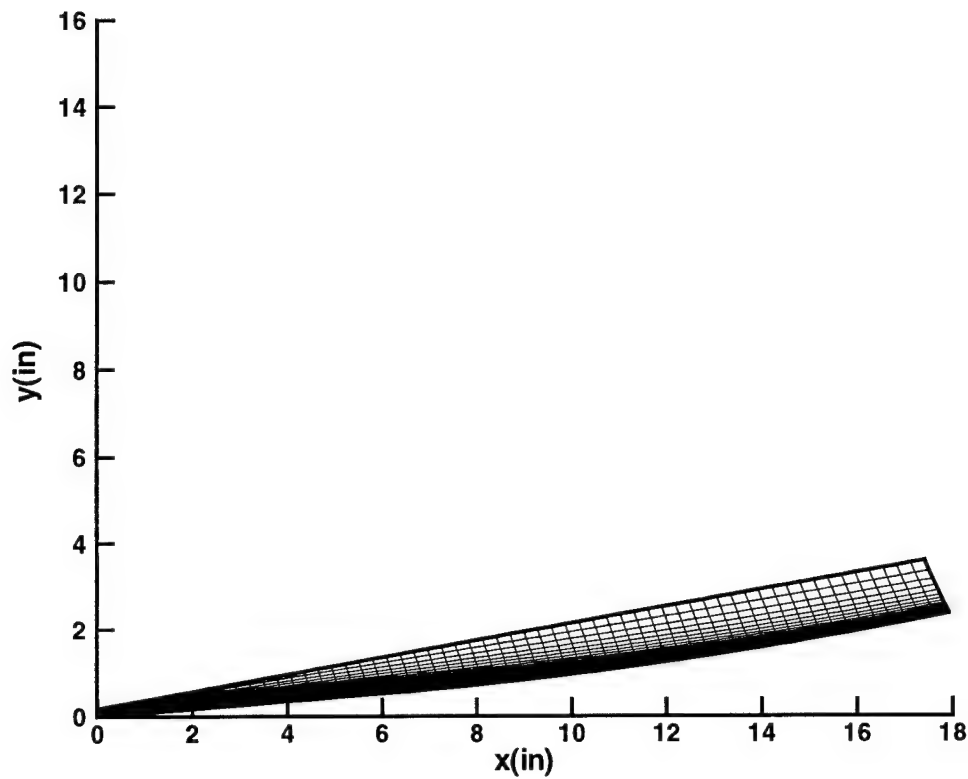


Figure 3.1. Computational Grid, 91-6 Model

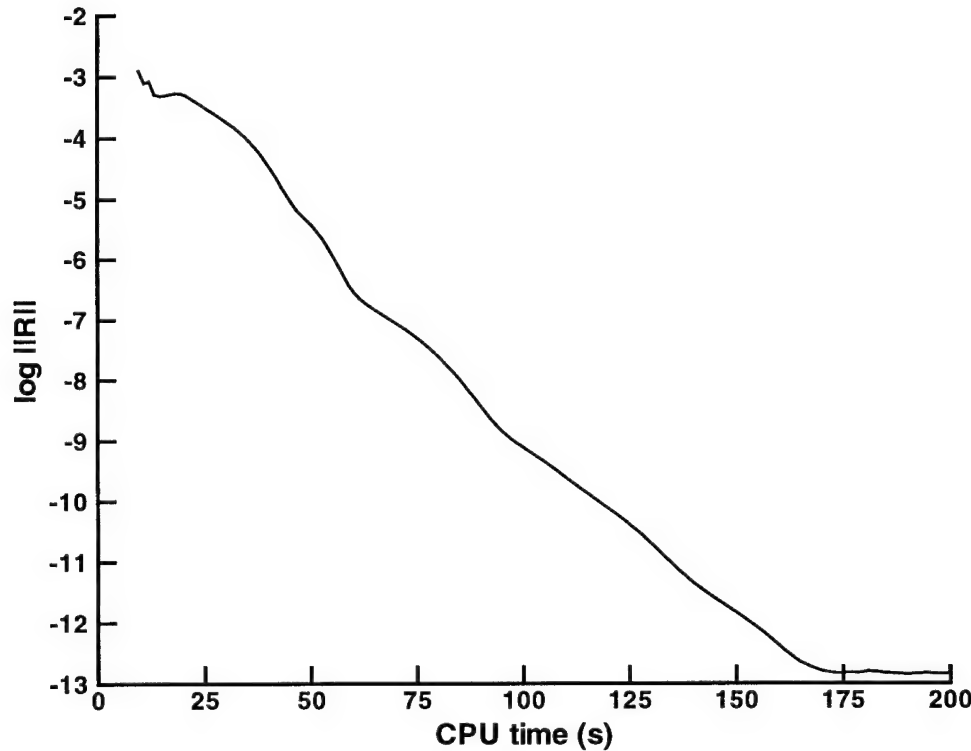


Figure 3.2. Convergence History

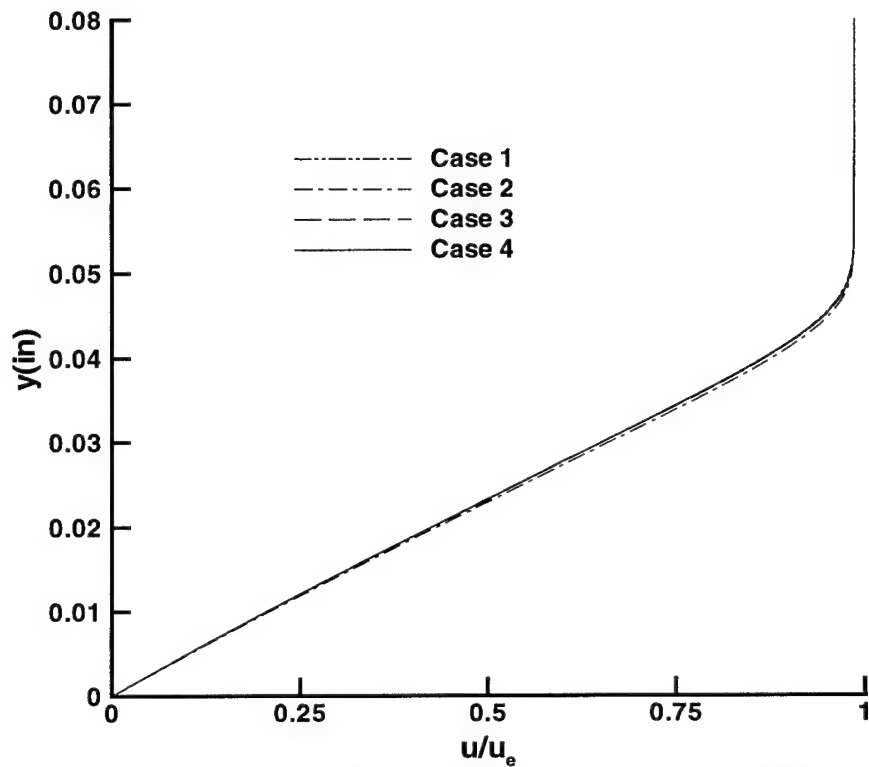


Figure 3.3. Effect of Grid Spacing on Velocity Profiles, $x=9''$

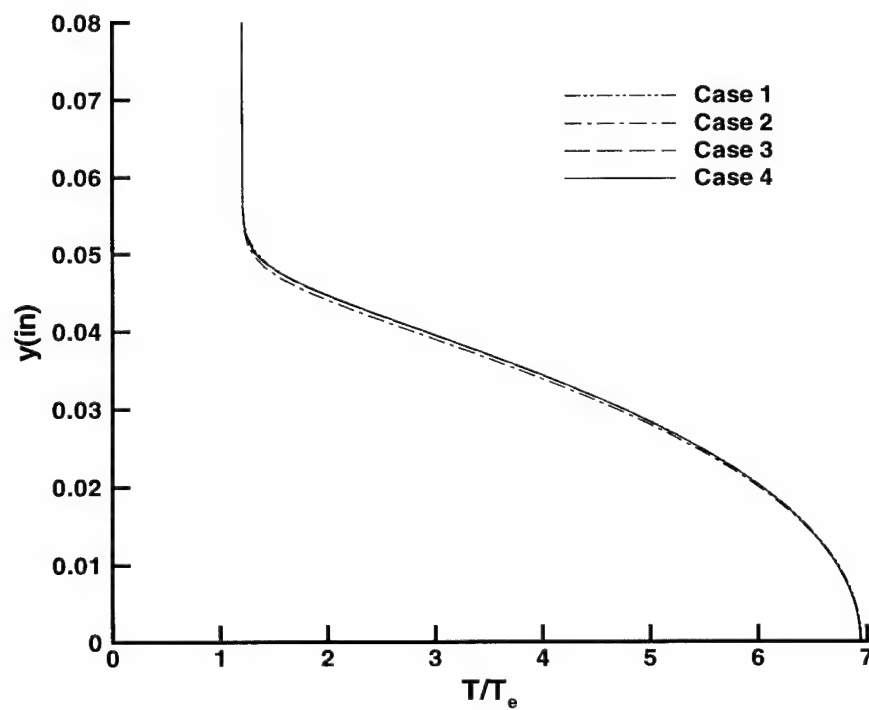


Figure 3.4. Effect of Grid Spacing on Temperature Profiles, $x=9''$

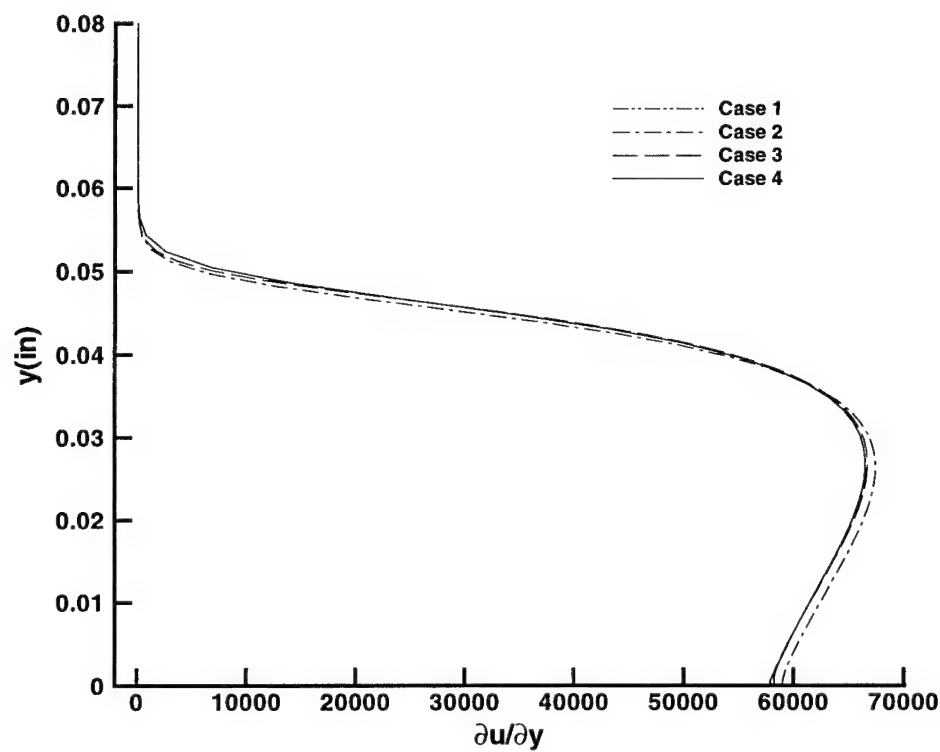


Figure 3.5. Effect of Grid Spacing on First Derivative of Velocity Profiles, $x=9''$

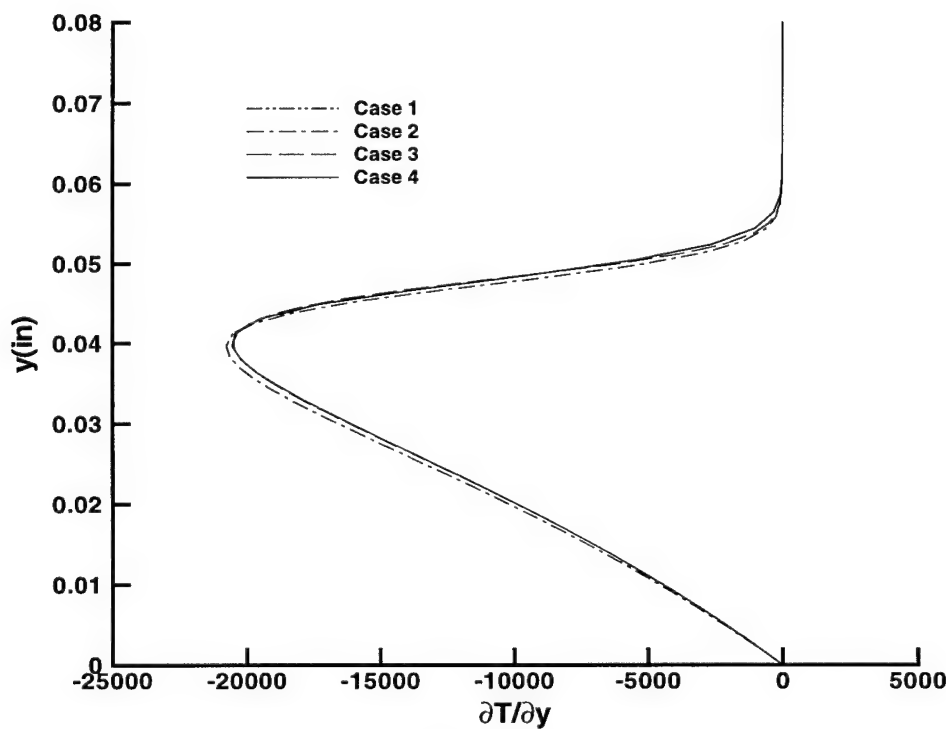


Figure 3.6. Effect of Grid Spacing on First Derivative of Temperature Profiles, $x=9''$

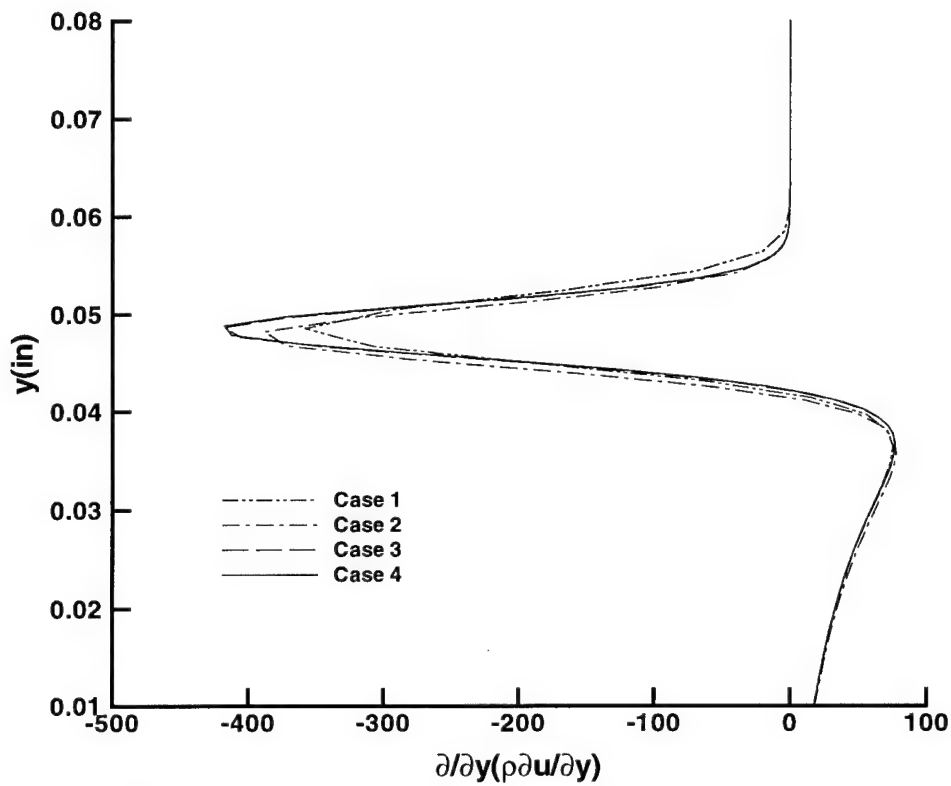


Figure 3.7. Effect of Grid Spacing on Generalized Inflection Point Profiles, $x=9''$

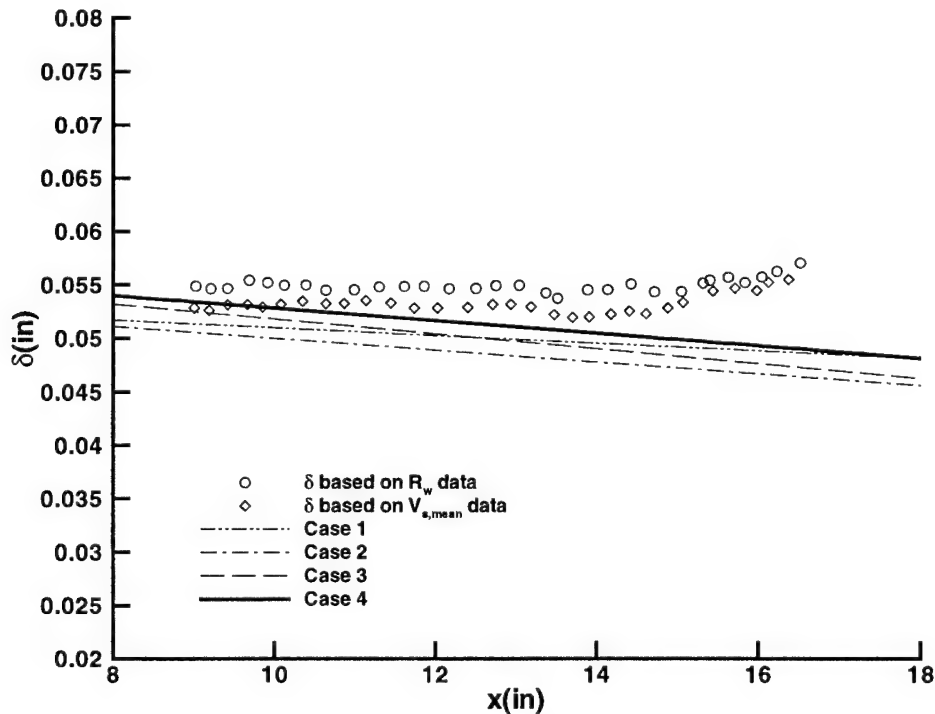


Figure 3.8. Effect of Grid Spacing on Boundary Layer Thickness Distribution

CHAPTER 4

RESULTS AND DISCUSSION

4.1 Introduction

In this chapter, the mean flow and LST computations are compared with the experimental measurements. The effects of wall cooling are examined for the 91-6 model. The effects of adverse pressure gradient are examined by comparing the 91-6 and 93-10 models under adiabatic wall conditions. The 91-6 model has a more adverse pressure gradient over a larger streamwise extent of the cone surface compared to the 93-10 model as seen in Figure 4.1, which shows the Navier-Stokes computed pressure distributions for both models.

Pressure gradient and wall cooling effects are first examined from the computed mean flow profiles of velocity and thermodynamic properties. Then, the mean profiles are compared with available experimental data. Next, amplification rate calculations from LST are presented to examine the effects of pressure gradient and wall cooling. The response of the uncalibrated hot-wire to boundary layer fluctuations are examined. Recommendations for future quiet tunnel experiments are also presented in the discussion.

4.2 Mean Flow Analysis

The effects of wall cooling and pressure gradient can be quantified by examining the mean flow profiles. In Figures 4.2 through 4.13, the mean flow profiles at $x=11''$ are discussed; the solid lines represent the 91-6 adiabatic model, the dashed lines represent the 91-6 cooled model and the dash-dot-dot lines represent the 93-10 adiabatic model.

Figures 4.2 and 4.3 show the mean velocity and temperature profiles. The wall cooling and adverse pressure gradient decrease the boundary layer thickness. The decreased wall temperature for the cooled model is also seen. The mean density profiles, Figure 4.4, show the same trends seen in the velocity and temperature profiles. The hot-wire is sensitive to mass flux and total temperature fluctuations; the sensitivity coefficients of the hot-wire are a function of the mean flow. Thus, hot-wire calibration must account for the total temperature and mass flux range for the measurement region. The value of the mean mass flux profile for the 91-6 model varies from zero to 1.7 over the height of the boundary layer as seen in Figure 4.5; the variation seen for the 93-10 model is slightly smaller. The total temperature profiles for the 91-6 and 93-10 models are shown in Figure 4.6. The total temperature variation through the boundary layer is much larger for the cooled wall than for the adiabatic wall cases. Figures 4.5 and 4.6 illustrate that the hot-wire calibration for measurements through the boundary layer must cover a wide range of mass flux and total temperature. For the case of the cooled wall, the hot-wire must be calibrated over a wider range of total temperature than for the adiabatic wall. Furthermore, for both the adiabatic and cooled wall cases, the overshoot in total temperature at the boundary layer edge necessitates wire calibration at temperatures in excess of the freestream total temperature value.

The first and second derivatives of the velocity, temperature and density mean flow profiles are shown in Figures 4.7 through 4.12. These profiles are smooth over the height of the boundary layer. Thus, the mean flow solutions are well resolved and are considered well suited as input for the stability analysis. Figure 4.13 shows the profiles of the generalized inflection point, which is a measure of the angular momentum of the

flow. The increasingly large peaks illustrate the destabilizing effect of pressure gradient and wall cooling on boundary layer stability. The location of the critical layer is in the outer portion of the boundary layer, which is expected for hypersonic flows.

Figure 4.14 compares the predicted and experimentally determined boundary layer thickness for the 91-6 model. In the experiment the boundary layer thickness was determined using two methods (Blanchard and Selby, 1996). In the first method, the R_w data, the boundary layer thickness is determined as the value of y where the resistance of the hot-wire, operated in its low overheat mode, is the same as the resistance at the outer edge. In the second method, the $V_{s,mean}$ data, the boundary layer thickness is the value of y where the mean voltage of the hot-wire, operated in its high overheat mode, is 99% of its value at the boundary layer edge. Both the velocity, δ_u , and temperature, δ_T , boundary layer thicknesses are calculated. δ_u is specified to be the location where the vorticity is less than 0.04% of the maximum vorticity; this value is then bounded by the criterion that the local velocity is 99.5% of the freestream velocity. δ_T is the location where the total temperature is 99.9% of the freestream value. For the adiabatic wall it is seen that upstream of $x=15''$ the predicted boundary layer thickness (δ_u) and the experimental measurements agree within 3%. Chokani (1999, 2000) has shown that at $x=12''$ nonlinear effects begin to become important and by $x=13''$ dominate the interactions in the boundary layer for the 91-6 model. Downstream of $x=15''$, a difference in trends indicated by the experiment and computation is seen for the adiabatic wall case; for the cooled wall case this difference is observed at $x=13''$. Overall, the computed boundary layer thickness results for the adiabatic wall show slightly better agreement with experimental results than the cooled wall calculations. The difference in trends

downstream of $x=15"$ (adiabatic wall) and $x=13"$ (cooled wall) are thought to occur since the computed flow is wholly laminar while in the experiment the flow is transitional. It may be of interest to examine the predictive capabilities of transitional models (Warren and Hassan, 1998) in regards to the boundary layer thickness distribution.

Figure 4.15 compares the wall static pressure on the 91-6 model. The calculations compare very well with the experimental data. The small differences between the experiment and calculation possibly arise from model misalignment. The predicted surface temperature distribution for the 91-6 model is compared with the experimental measurements in Figure 4.16. The rise in the measured temperature at $x=12"$ for the adiabatic wall is due to the transitional nature of the boundary layer. Upstream of this location, the predictions and experiment are in very good agreement, within 3% of each other. A discrepancy between the experiment and cooled wall computations exists upstream of $x=6"$. The computational results are obtained for a constant wall temperature. However, the tip of the thin-walled cone model is not cooled. Therefore, a temperature gradient exists between the relatively hot tip and the cooler thin wall downstream of the leading edge region. Uniform temperature is not achieved until $x=7"$. In the range of $7 \leq x \leq 12"$, the calculated and experimental results agree within 1%. The differences between the experimental and computational results downstream of $x=12"$ are due to the onset of transition. In addition to the transitional nature of the boundary layer in the experiment, there are other possible sources for the differences between experiment and computation. In the experiment, a preheat procedure is used to bring the nozzle and model into thermal equilibrium. Following preheat, the hypersonic flow is started and the measurements are subsequently taken. If adiabatic wall conditions are not achieved,

this may be a source of some discrepancy. A second possible source of error is that the cone tip is solid whereas the cone wall is thin. Thus for the adiabatic wall case where the wall normal temperature gradient may be negligible (ideally zero) the wall parallel temperature gradient may be significant and heat conduction along the thin-skin wall may contribute some differences. The heat conduction are thought to be some source of the differences seen upstream of $x=6''$ for the cooled wall case. One possible approach to examine this effect is to couple the heat conduction equations for the thin solid wall with the Navier-Stokes equations; the heat conduction equations are used to provide the wall boundary condition for the mean flow. In the present work, this approach could not be employed, as there are insufficient details on the model geometry and material. An alternate approach is instead used.

The sensitivity of the mean flow solution for the 91-6 cooled model to the wall temperature boundary condition was examined by using the experimentally measured wall temperature distribution. A series of polynomials are fit to the data, Figure 4.17, and used as the wall boundary condition for the mean flow calculation. The predicted boundary layer thickness results for this calculation are shown in Figure 4.18 for the range of the experimental measurements. The boundary layer thickness distributions agree within 2% in the linear growth region (upstream of $x=13''$); thus, very little effect of the wall temperature distribution is seen. Figure 4.17 shows a nearly constant temperature over the range of $7 \leq x \leq 12''$ and increasing temperature downstream of $x=12''$. It is of interest to examine the effect of the wall temperature distribution on the mean flow. Profiles of velocity, total temperature and density for constant and variable wall temperature distributions at $x=9''$ and $x=13''$ are shown in Figures 4.19 through 4.24. The

increased wall temperature appears to have little effect on the mean flow profiles. Thus, using a constant wall temperature distribution is sufficient for the 91-6 cooled model mean flow calculations. Kimmel and Poggie, who performed experimental measurements on a cone at $M=6$, have also stated that the presence of a hot nose tip on the model had little effect on the boundary layer stability or transition data (1999).

The calculated and experimentally measured pressure distributions for the 93-10 adiabatic model are shown in Figure 4.25. Good agreement is seen and the difference is within 6%. A possible source for the disagreement is model misalignment; experimental results suggest that the model is at a small angle of attack. The computed and experimentally measured temperature distributions for the 93-10 model are shown in Figure 4.26. Lachowicz and Chokani (1996) observed that nonlinear boundary layer interactions are first observed at $x=15''$ or $R_s=1890$ for the 93-10 model, which corresponds to the sharp rise downstream of this location in the experiment. Upstream of $R_s=1890$, the results agree within 1%. The rise in temperature occurs further downstream on the 93-10 model compared to the 91-6 model ($x=12''$) due to the smaller adverse pressure gradient on the 93-10 model. The effect of the pressure gradient is seen when the computed boundary layer thickness distributions for the 91-6 and 93-10 models are compared, Figure 4.27. Due to the more adverse pressure gradient, the 91-6 model has a thinner boundary layer than the 93-10 model. A comparison between experimental and computed boundary layer thickness distributions for the 93-10 model is shown in Figure 4.28. In the experiment, the boundary layer thickness was determined as the location where the voltage of the hot-wire, operated in low overheat mode, is 99.5% of the value furthest from the wall. Upstream of $R_s=1890$ the agreement between the experimental

measurements and the δ_u calculation is within 1%. Downstream of $R_s=1890$, the computed flow is laminar, whereas the actual flow is now transitional and a larger difference is seen.

Blanchard and Selby's hot-wire measurements were uncalibrated and thus no direct comparisons can be made between mean flow computations and experimental measurements (1996). Lachowicz *et al* (1996) observed that the constant voltage anemometer, like the more conventional CCA and CVA, is more sensitive to mass flux when the hot-wire is operated in high overheat mode and more sensitive to total temperature at when the hot-wire is operated in low overheat mode. Thus, the trends of the hot-wire measurements obtained in high overheat mode can be compared with the computed mean mass flux calculations and the hot-wire measurements obtained in low overheat mode can be compared with the computed mean total temperature. Figures 4.29 and 4.30 show a comparison of the calculated mean total temperature and normalized hot-wire resistance obtained in low overheat mode at $x=9''$ for the 91-6 model with adiabatic and cooled wall conditions respectively. In both cases the measured data show the overshoot at the boundary layer edge that is also observed in the computed total temperature profiles. The magnitudes of the overshoot are also in good agreement. Below the edge of the boundary layer, the difference between the experiment and computation is increasingly larger. One possible reason for the difference is that even though the hot-wire is operated in low overheat mode, it is somewhat sensitive to mass flux and the mass flux is changing quite rapidly near the wall, Figure 4.5. The difference seen in Figures 4.29 and 4.30 may also be a good measure to evaluate the new transition models for mean flow solvers (Warren and Hassan, 1998). Figures 4.31 and 4.32 show

contour plots of the computed total temperature and the experimentally measured hot-wire resistance for the 91-6 adiabatic model. Upstream of $x=12"$ good agreement is seen over the outer portion of the boundary layer; the magnitudes and directions of the contour lines are in good agreement. In the inner portion of the boundary layer, the contours of R_w are more steeply inclined than the contours of T_o . The mean flow computations are wholly laminar, whereas in the experiment, nonlinearities are observed downstream of $x=12"$ (Chokani, 1999). Thus, downstream of $x=12"$, there are significant difference between the computation and experiment. The computation contour lines show the same trends as upstream of $x=12"$, whereas in the experiment the contour lines in the outer portion of the boundary layer are more closely spaced together and in the inner portion even more steeply inclined downstream of $x=12"$. Contour plots of the computed mass flux and the measured hot-wire mean voltage are shown in Figures 4.33 and 4.34 for the 91-6 adiabatic model. Again, good agreement is observed upstream of $x=12"$. However, the laminar mean flow calculation does not capture the complexities of the flow downstream of $x=12"$. Similar results are seen for the 91-6 model with cooled wall conditions in Figures 4.35 through 4.38.

In Lachowicz and Chokani's experiment, a procedure for the calibration of the hot-wire operated by the CVA was examined (1996). At the time of the experiment, the CVA was a novel instrument. The relationship between the CVA output and flow variables was assumed to be

$$V_s = a(\rho u) + b(T_o) + c \quad (4.2.1)$$

where a and b represent the hot wire sensitivities and are given by

$$a = \frac{\partial V_s}{\partial(\rho u)} , \quad b = \frac{\partial V_s}{\partial(T_o)} \quad (4.2.2)$$

Decomposing the output and flow variables into a mean and fluctuation term yields the following for the mean flow

$$\bar{V}_s = a(\bar{\rho u}) + b(\bar{T}_o) + c \quad (4.2.3)$$

The wire was then calibrated by determining the wire sensitivities for a given overheat from a series of known flows. That is,

$$\begin{bmatrix} (\bar{\rho u})_1 & \bar{T}_{o_1} & 1 \\ (\bar{\rho u})_2 & \bar{T}_{o_2} & 1 \\ \vdots & \vdots & \vdots \\ (\bar{\rho u})_n & \bar{T}_{o_n} & 1 \end{bmatrix} \begin{bmatrix} a \\ b \\ c \end{bmatrix} = \begin{bmatrix} \bar{V}_{s_1} \\ \bar{V}_{s_2} \\ \vdots \\ \bar{V}_{s_n} \end{bmatrix} \quad (4.2.4)$$

This procedure was repeated for different wire overheats. Then, boundary layer measurements were conducted with the wire operated at different overheats at each measurement point to determine the mass flux and total temperature. That is,

$$\begin{bmatrix} a_1 & b_1 \\ a_2 & b_2 \\ \vdots & \vdots \\ a_m & b_m \end{bmatrix} \begin{bmatrix} (\bar{\rho u}) \\ \bar{T}_o \end{bmatrix} = \begin{bmatrix} \bar{V}_{s_1} - c_1 \\ \bar{V}_{s_2} - c_2 \\ \vdots \\ \bar{V}_{s_m} - c_m \end{bmatrix} \quad (4.2.5)$$

The flow variables experimentally determined using the calibrated hot-wire are compared with calculations in Figures 4.39 and 4.40 for the 93-10 model. At $x=13.5''$ the agreement between experiment and computation is very good. Lachowicz and Chokani (1996) observed nonlinear interactions in the flow downstream of $x=15''$. Thus, at the more downstream locations only fair agreement is observed between the experiment and computation. Lachowicz and Chokani attribute the differences at the more downstream stations to transition effects, model misalignment and possible minor probe intrusion effects. Kendall (1956) examined the effect of increasing probe diameter on the pitot pressure measurements made in a Mach 5.8 flat plate boundary layer. Three pitot probes

with frontal heights of 0.0025in ($1/24^{\text{th}}$ of the boundary layer thickness), 0.005in ($1/12^{\text{th}}$ δ) and 0.01in ($1/6^{\text{th}}$ δ) were examined, Figure 4.41. The 0.01in probe shows an overshoot in the pitot pressure near the edge of the boundary layer. Pitot probe measurements were not conducted by Lachowicz and Chokani (1996) nor Blanchard and Selby (1996). Computations of the pitot pressure profiles at several stations on the 91-6 cooled model are shown in Figure 4.42. An overshoot in the pitot pressure near the boundary layer is not seen in the computations. This finding is in contrast with the measurements made by Stetson *et al* (1983) and presented in Figure 4.43 (Schneider, 2000), where the pitot probe height varies from $1/12^{\text{th}}$ to $1/20^{\text{th}}$ of the boundary layer thickness. The pressure overshoot is less pronounced at the downstream location where the boundary layer is thicker. As regards to the hot-wire measurement, the hot-wire probe, Figure 2.9, is very small compared to the boundary layer thickness and probe intrusion effects are likely to only be small. However, care should be taken to minimize the frontal height of the probe support and streamline the thickness downstream of the probe tip.

The large bandwidth (that is range of frequencies) is one of the primary reasons for employing hot-wire anemometry in hypersonic stability experiments. The bandwidth of the CVA (as well as CCA and CTA) is dependent on the wire Reynolds number. For example, Sarma (1999) has examined the hot-wire time constant (a measure of the inverse of the bandwidth) as a function of the wire Reynolds number, Figure 4.44. For the $2.5\mu\text{m}$ (0.0001in) hot-wire used in the Blanchard and Selby (1996) and Lachowicz and Chokani (1996) experiments, profiles of the calculated wire Reynolds number across the boundary layer are shown for various streamwise locations in Figures 4.45 through 4.47. For the stability measurement data acquired near the boundary layer edge and over

the range of 0.8δ to δ , the wire Reynolds number varies within the range of 7-20 for the 91-6 model and 19-30 for the 93-10 model. Figure 4.46 suggests that the bandwidth should thus vary little over this portion of the boundary layer.

4.3 Linear Stability Analysis

Linear stability analysis is performed using the quasi-parallel, spatial stability theory code written by Hudson (1996). The effects of pressure gradient and wall cooling on the amplification rates, most amplified frequencies and N -factors are first examined. Then, the density, velocity and temperature eigenfunctions are examined to assess the procedures for hot-wire measurements.

The amplification rates for the 91-6 adiabatic and cooled models and 93-10 adiabatic model at $x=14"$, $15"$ and $16"$ are plotted in Figure 4.48. These results are obtained by determining the range of unstable frequencies in the mean flow at each streamwise location. The results show three expected trends. First, for each test case the amplification rates increase with increasing streamwise distance. Second, the effect of adverse pressure gradient and wall cooling is destabilizing. Third, the range of unstable frequencies increases as the boundary layer thickness decreases; thus, the 93-10 model has the relatively low frequency band of unstable disturbances, whereas the 91-6 cooled model has the relatively high frequency band. For the 93-10 model, the range of unstable frequencies lie in a band between 160 and 240kHz which is centered on a most unstable frequency of 190kHz. Lachowicz and Chokani measured an unstable frequency band of 170 – 275kHz, centered on 230kHz (1996). For the 91-6 adiabatic model, LST predicts an unstable band of 190-285kHz centered on 230kHz and in the experiment, Blanchard and

Selby observe a peak frequency of 275kHz in a band of $225\text{-}345\text{kHz}$. On the 91-6 cooled model, an unstable frequency band of $235\text{-}385\text{kHz}$ centered on a frequency of 306kHz is measured (Blanchard and Selby, 1996); in the LST computation, a peak frequency of 260kHz in an unstable band of $220\text{-}310\text{kHz}$ is predicted. The band of unstable frequencies varies inversely with the boundary layer thickness. This tuning of the most amplified second mode disturbances has been experimentally observed by Stetson *et al* (1983), Lachowicz and Chokani (1996) and Kimmel *et al* (1991, 2000) amongst others, and was first suggested in the linear stability theory analysis of Mack (1984). Doggett *et al* experimentally examined the effect of angle of attack on boundary layer stability (1997). In their experiments, the 93-10 model was tested in the Mach 6 quiet tunnel at 0° and $\pm 2^\circ$ angles of attack. Three dimensional Navier-Stokes analysis was also conducted to assess the effects of small angle variations on the peak frequency. At $x=13''$ ($\text{Re}_s=3.1\times 10^6$) the peak frequency of 238kHz changed by 55kHz with 0.2° change in angle of attack, Figure 4.49. This observation and the LST predicted results indicate that there may be significant angle of attack effects in the experiments. It should be noted also that in linear stability theory the assumption that the disturbances at different frequencies do not interact is employed. However, as Reshotko observed, the boundary layer behaves like a nonlinear oscillator and this may be a source of some discrepancy (1994). Another source of error may be the parallel flow assumption in the LST approach; Herbert *et al* (1993) and Stuckert and Lin (1995) noted a shift in growth rate curves when nonparallel terms are excluded. In the experiment the hot-wire measurements were conducted along one streamwise plane. In future experiments, it may be useful to conduct measurements along the 180° out-of-phase streamwise plane to

resolve uncertainties with regards to the most unstable band of frequencies, Figure 4.50. The effect of the variable wall temperature distribution, Figure 4.17, on the amplification rates is shown in Figure 4.51. The comparisons are shown for three streamwise locations for the 91-6 cooled model. The boundary layer is slightly thicker for the variable wall temperature calculation, Figure 4.18, thus, the range of unstable frequencies for the variable wall temperature distribution are 5 kHz smaller than for the constant wall temperature distribution. Figure 4.51 however shows that the temperature distribution has very little effect on the amplification rates and thus the boundary layer stability (Kimmel and Poggie, 1999).

In Figure 4.48, the frequencies of the most amplified disturbances change little with increasing streamwise distance because the boundary layer thickness varies little. The streamwise evolution of the amplification rates for the most amplified disturbances are shown in Figure 4.52. In contrast to a zero pressure gradient flow where there is a decay of the most amplified disturbance after an initial unstable region, the pressure gradient on the 91-6 and 93-10 models result in a nearly constant boundary layer thickness and thus, the most amplified disturbances grow over the length of the flare. The stability Reynolds number is plotted along the abscissa in Figure 4.52 to enable a more meaningful examination of the effects of pressure gradient and wall cooling. It is evident that the increasing adverse pressure gradient and wall cooling are destabilizing.

The N -factor distributions for the peak frequencies are shown in Figure 4.53. A value of 9 to 10 is commonly considered indicative of transition onset (Malik, 1992). However, Balakumar and Malik (1994) used a N -factor of between 7.5 and 8.5 to determine the transition location. The 91-6 cooled model reaches an N -factor of 9 at

$x=18''$. The flow over the 91-6 and 93-10 models with adiabatic wall conditions reach peak values of $N=7$ at $x=18''$ and $N=3.5$ at $x=20''$ respectively.

The density eigenfunctions of the most amplified disturbances for the 93-10 and 91-6 models at $x=13''$ are shown in Figure 4.54. Two peaks in the density eigenfunction are seen at approximately 30% of boundary layer thickness and at the boundary layer edge. The velocity eigenfunctions are shown in Figure 4.55. The peak in the velocity eigenfunction is at about 25% of the boundary layer thickness. The hot-wire anemometer is sensitive to mass flux and total temperature. The mass flux eigenfunctions, given by the following equation

$$(\rho u)' = \rho u' + \rho'u + \rho'u' , \quad (4.3.1)$$

are shown in Figure 4.56. The mass flux eigenfunctions show two primary peaks at 25% of the boundary layer thickness and at the boundary layer edge that arise from the dominant peaks in the density and velocity eigenfunctions. A third peak is also observed at 60% of the boundary layer thickness and is thought to result from the density and velocity mean flow profiles, Figures 4.2 and 4.4. The peak at 60% of the boundary layer is most pronounced for the 91-6 adiabatic model and least pronounced for the 91-6 cooled model. The total temperature eigenfunctions are shown in Figure 4.57. A small peak is seen at 10% of the boundary layer thickness and a larger peak is located at approximately 75% of the boundary layer thickness. As no initial amplitude of the disturbance is specified in LST, the effects of pressure gradient and wall cooling in Figures 4.54-4.57 cannot be compared. However, for a given case it is evident that a hot-wire traversed through the boundary layer will give a changing output due to the variations in the mass flux and total temperature eigenfunctions.

Uncalibrated hot-wire measurements on the 91-6 model were obtained with the hot-wire operated at a high overheat mode; thus, the hot-wire was most sensitive to mass flux fluctuations. Figures 4.58 and 4.59 show the hot-wire RMS output measured at $x=9"$. The RMS output is a measure of the RMS energy in the disturbances. Two peaks are seen in the measured profiles, one at approximately 85% of the boundary layer thickness and a second one at approximately 55% of the boundary layer thickness. Pruett and Chang performed a Direct Numerical Simulation (DNS) for Mach 6 flow over the 93-10 adiabatic model (1998). Their normalized RMS mass-flux fluctuations are shown in Figure 4.60. (Note that the variables x^* and η in Figure 4.60 have different meanings than the variables used in this work.) The $x^*=1.167$ station in Figure 4.60 corresponds to $x=14.5"$ on the 93-10 model. At this station, Pruett and Chang observe a double peak in their results. Furthermore, the y -locations of the peaks in Figure 4.60 correspond to the locations of the peaks seen in the experimental RMS energy measurements in Figures 4.58 and 4.59.

There are several possible explanations for the double peak seen in the experimental data and the differences between the experimental and LST results. In the experiment, the wire is traversed across the boundary layer while the wire voltage is kept constant. As the recovery temperature and wire Reynolds number vary through the boundary layer, the wire's sensitivity to mass flux and total temperature vary through the boundary layer. In Figures 4.45-4.47, the wire Reynolds number changes significantly over the boundary layer and as seen in Figure 4.44 at low wire Reynolds numbers the wire has a very nonlinear response. This complex mixed mode response of the wire and the variation of the sensitivity coefficients emphasize the need for calibrated hot-wire

measurements. It is also important to note the observation of Pruett and Chang (1998) in regards to their DNS computations. They noted that in the experiment the energy of the second mode is distributed over the range of frequencies of the amplified disturbances, whereas the computation is performed only for one frequency – in the present case, the most amplified disturbance. Similarly, Demetriades (1977) observed that the amplitude of the hot-wire signal persisted until 1.5 times the boundary layer thickness; in the eigenfunctions, the boundary condition of the LST analysis require that there is no disturbance amplitude outside the boundary layer.

The contour plots of the mass flux and total temperature eigenfunctions of the most amplified disturbances on the 91-6 adiabatic model at 230 kHz are shown in Figures 4.61 and 4.62 respectively; the range $x=9''$ to $x=16.5''$ corresponds to the measurement range. These plots can be compared with the experimental RMS contours seen in Figure 4.63 for the 91-6 adiabatic model. Contour plots of mass flux and total temperature eigenfunctions at 260kHz for the 91-6 cooled model are shown in Figures 4.64 and 4.65 and can be compared with the RMS contours in Figure 4.66. Over the range of measurement, the experiment and computation both show that the maximum peak moves closer to the wall with increasing x . The second peak that is located closer to the wall is also seen in Figures 4.62 and 4.65 over the range $x=9''$ to $x=14''$. In their hot-wire measurements Lachowicz and Chokani surveyed along the path of maximum RMS energy (1996). Similarly, Stetson (1989) using a CCA conducted his measurements along the path of maximum RMS energy. In the Blanchard and Selby experiment (1996), the measurements were conducted at a constant distance from the wall; this is shown as the hot-wire survey path in Figures 4.62 and 4.65. It is clear that this does not coincide

with the maximum in the RMS contours and this may be a potential source of error in the comparison of experimentally and computationally determined disturbance amplification rates.

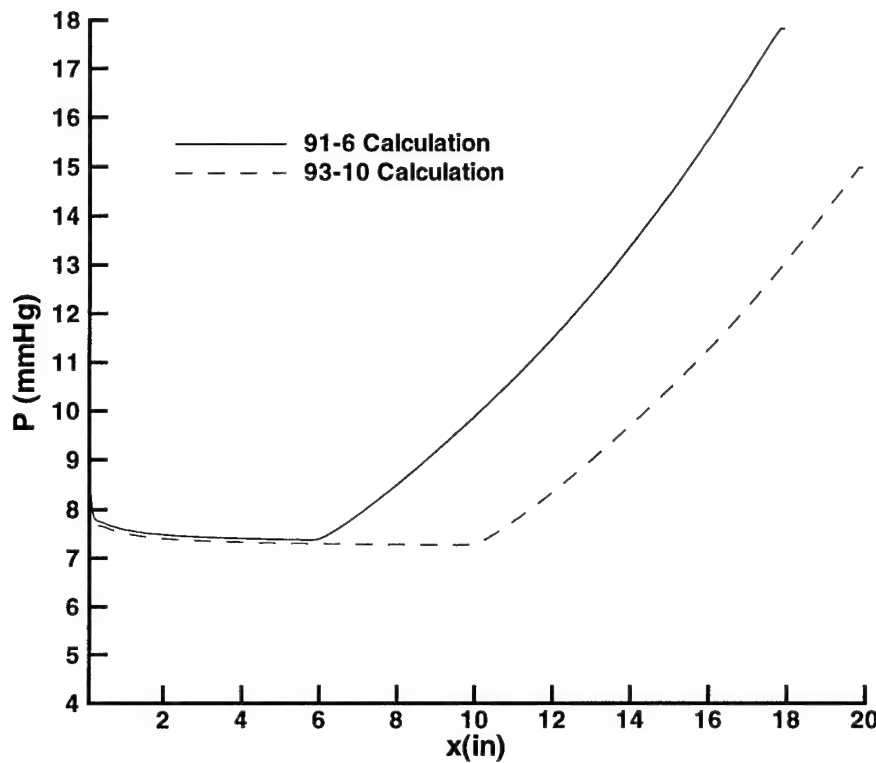


Figure 4.1. Pressure Distribution on 93-10 and 91-6 Models

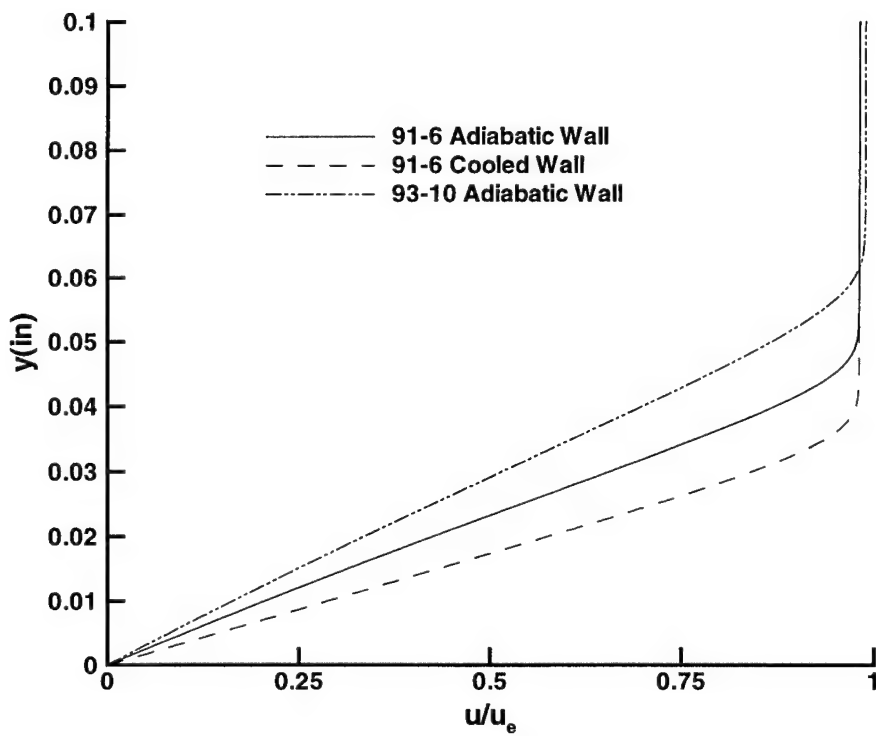


Figure 4.2. Velocity Profiles at $x=11''$

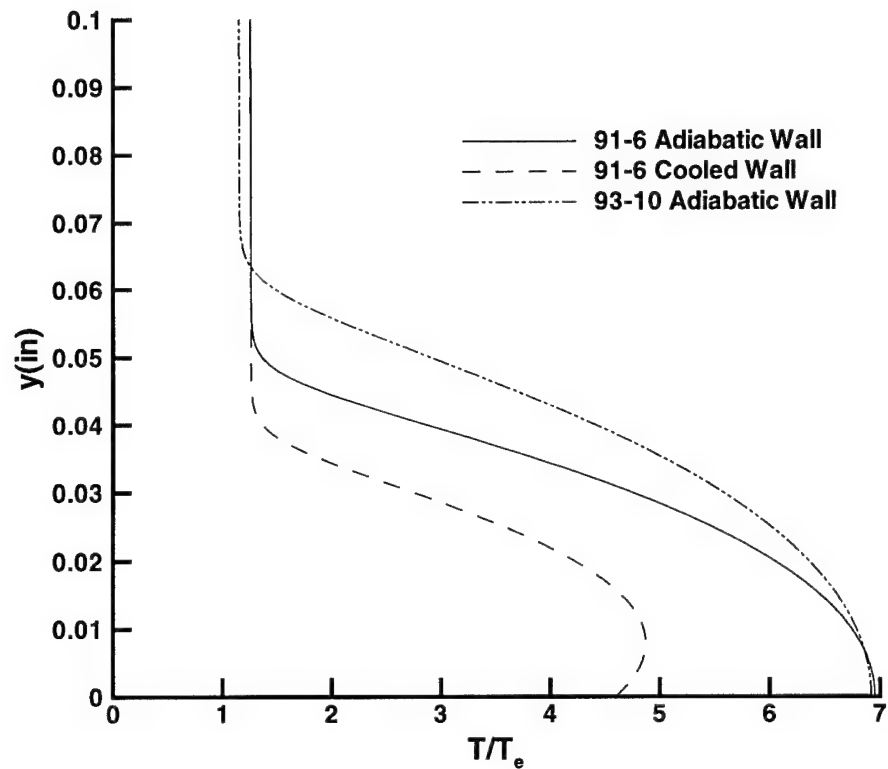


Figure 4.3. Temperature Profiles at $x=11''$

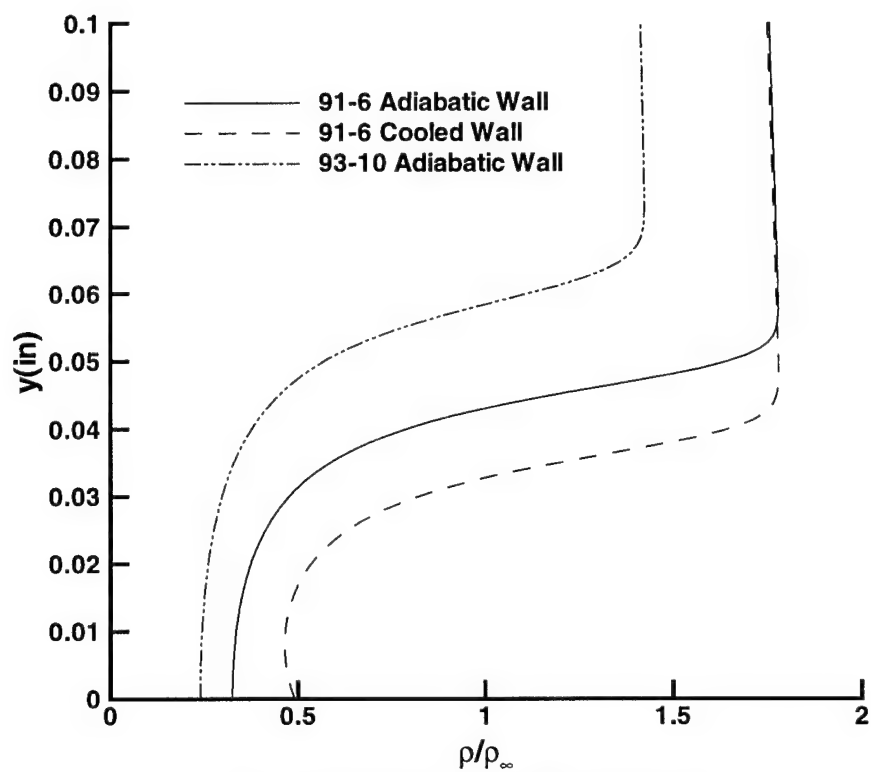


Figure 4.4. Density Profiles at $x=11''$

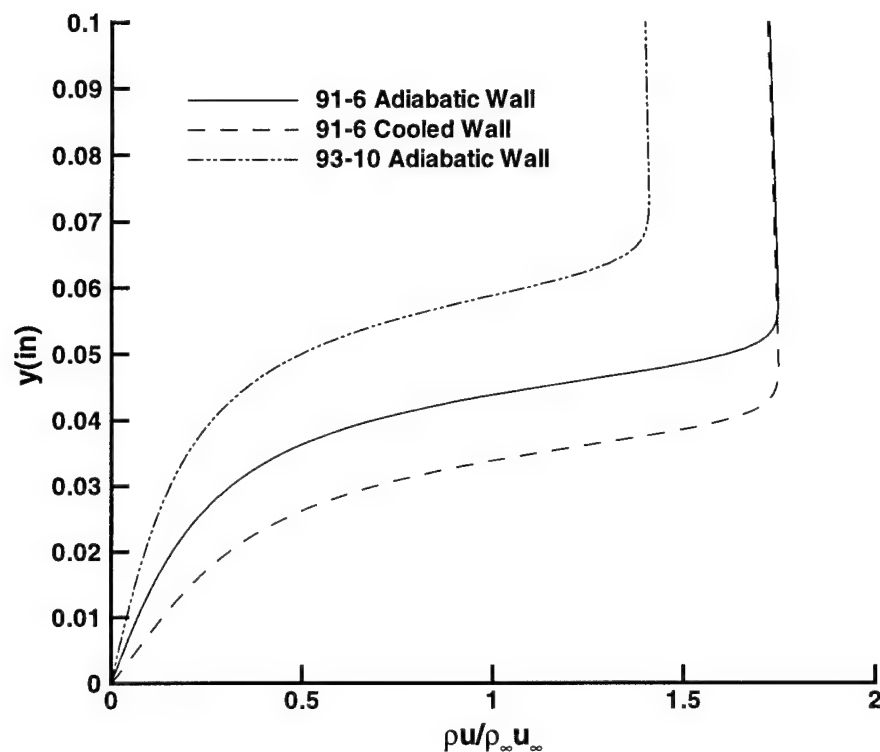


Figure 4.5. Mass Flux Profiles at $x=11''$

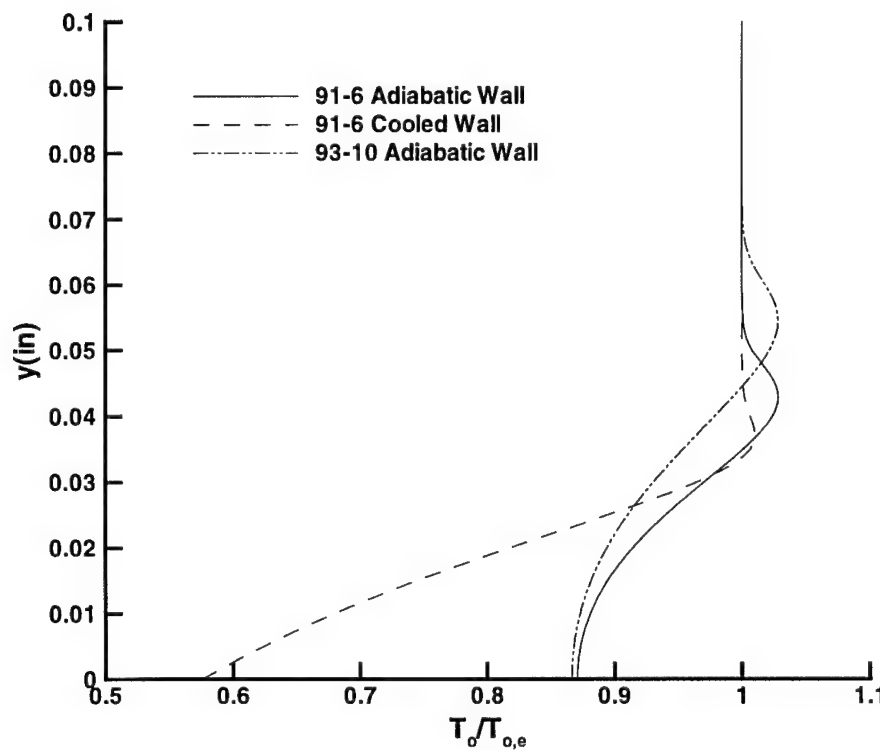


Figure 4.6. Total Temperature Profiles at $x=11''$

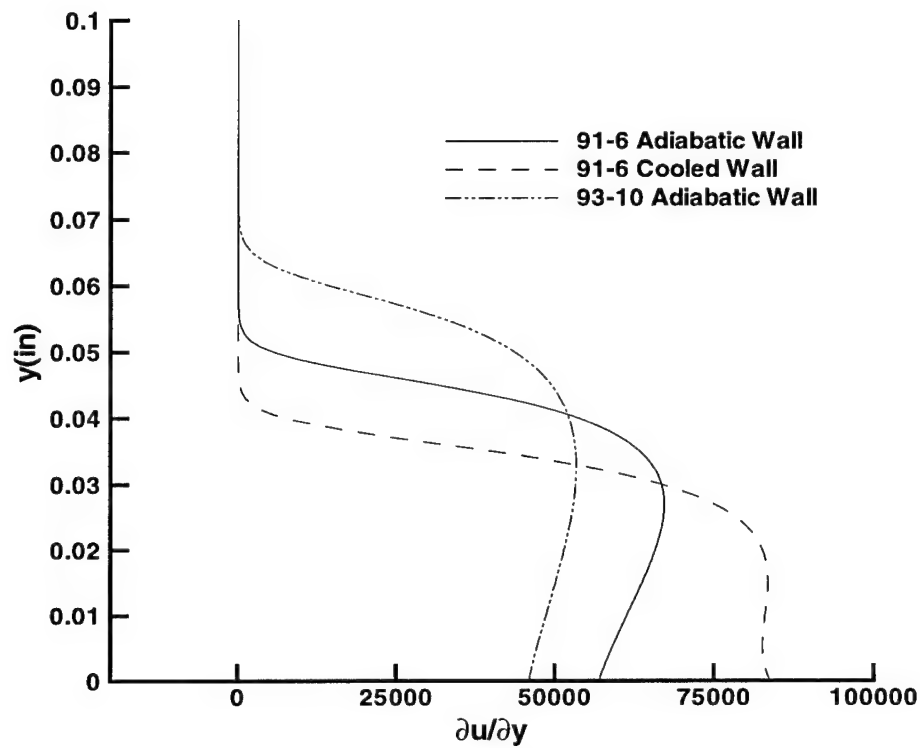


Figure 4.7. First Derivative of Velocity Profiles at $x=11''$

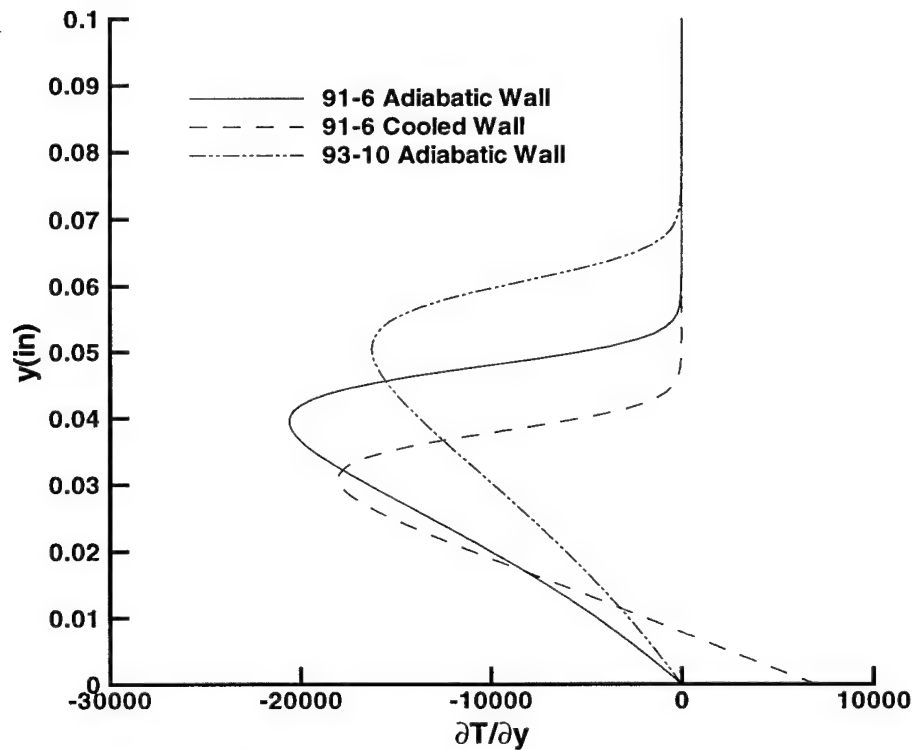


Figure 4.8. First Derivative of Temperature Profiles at $x=11''$

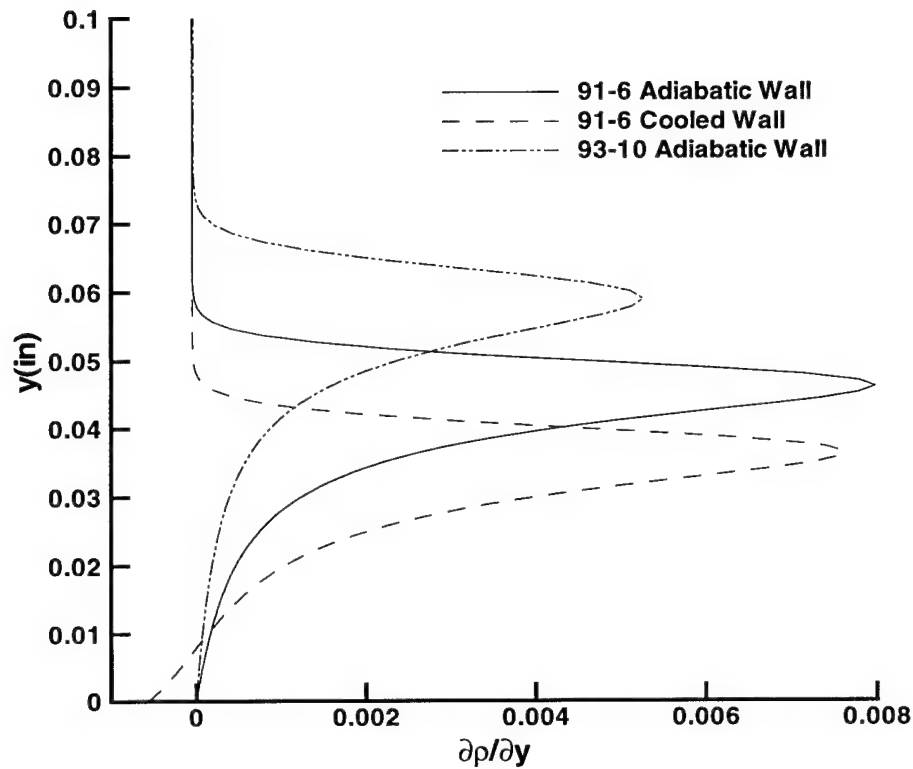


Figure 4.9. First Derivative of Density Profiles at $x=11''$

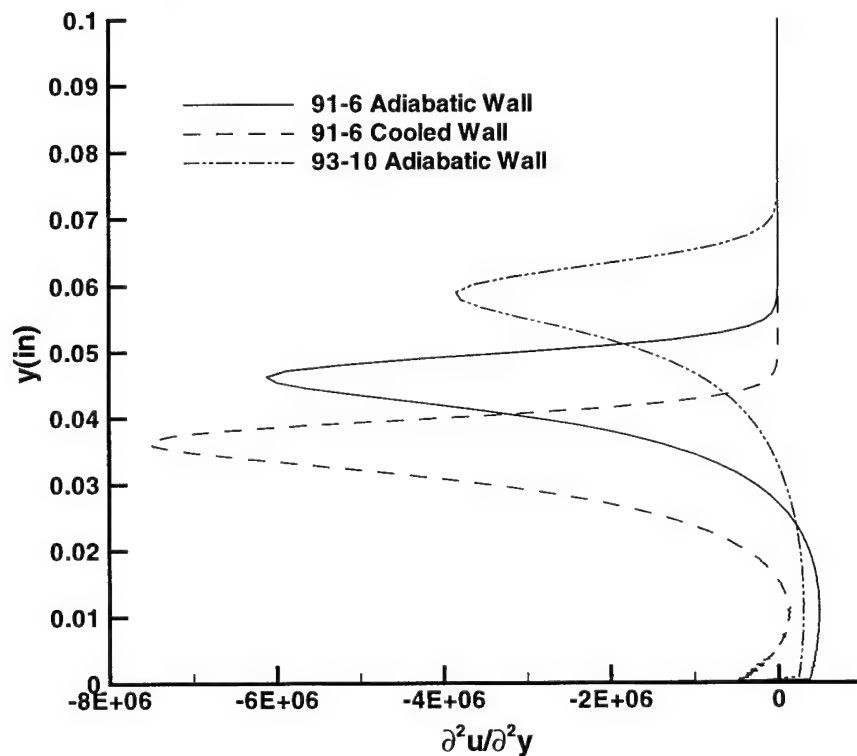


Figure 4.10. Second Derivative of Velocity Profiles at $x=11''$

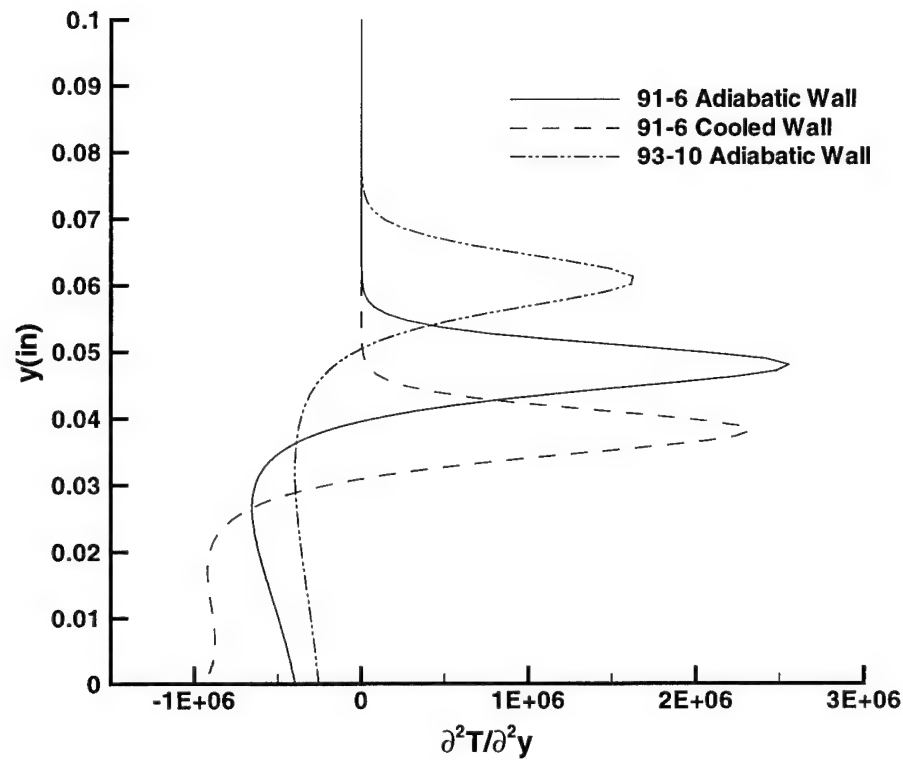


Figure 4.11. Second Derivative of Temperature Profiles at $x=11''$

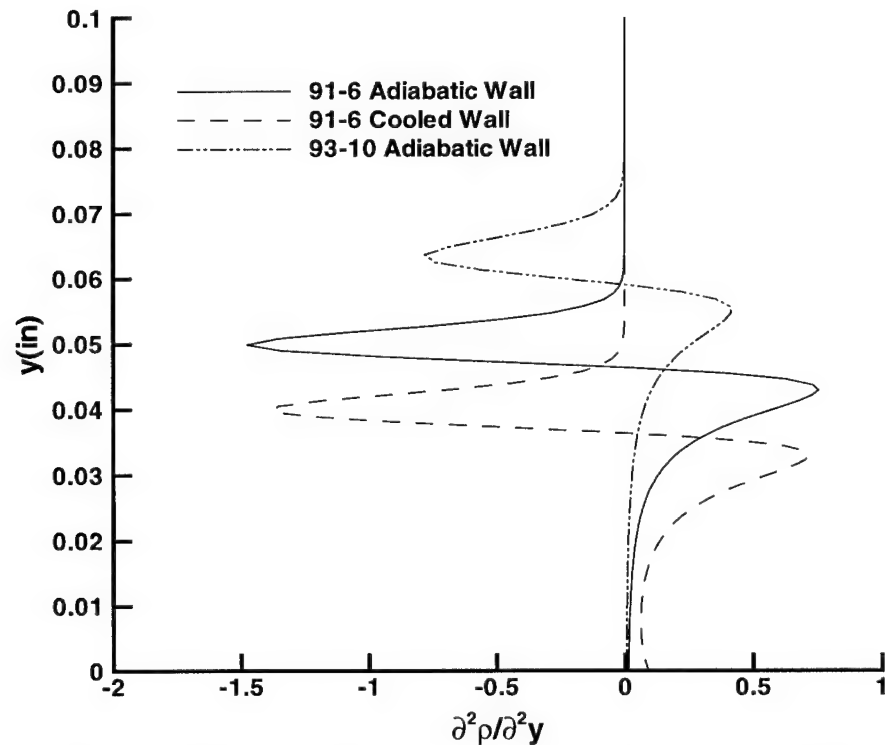


Figure 4.12. Second Derivative of Density Profiles at $x=11''$

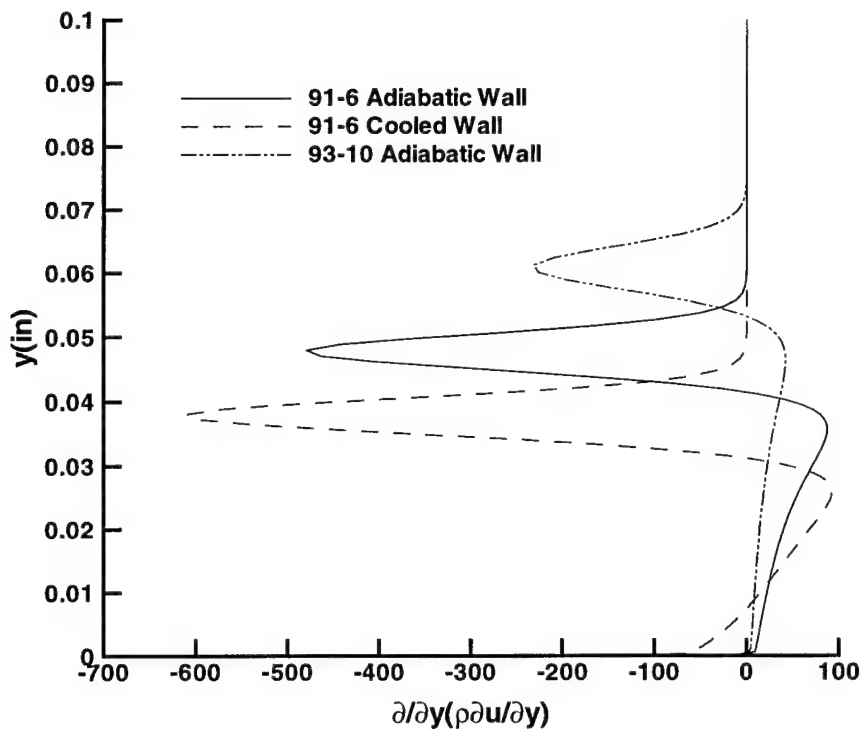


Figure 4.13. Generalized Inflection Point Profiles at $x=11''$

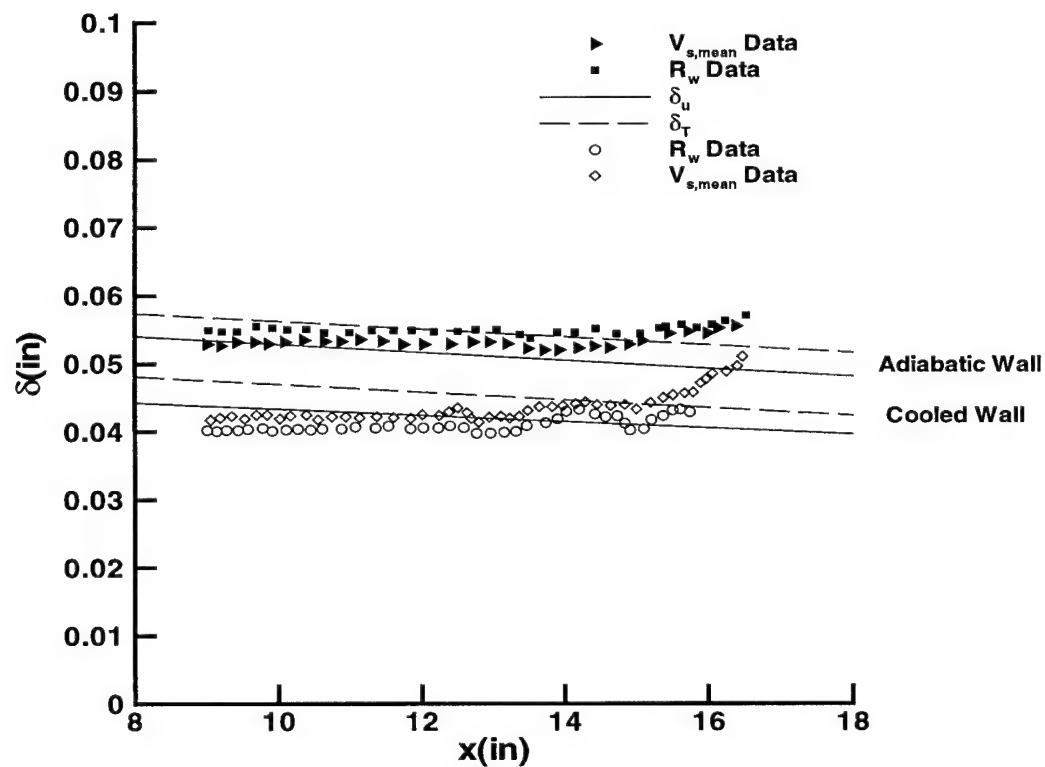


Figure 4.14. Effect of Wall Cooling on Boundary Layer Thickness Distribution, 91-6 Model (Solid Symbols are Adiabatic Wall, Hollow Symbols are Cooled Wall)

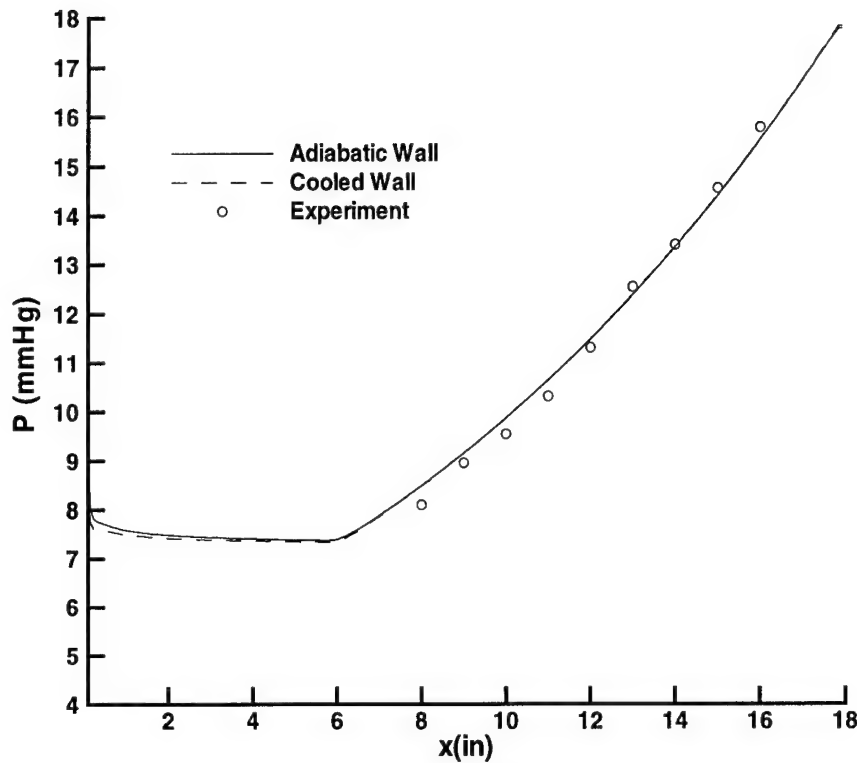


Figure 4.15. Surface Pressure Distribution, 91-6 Model

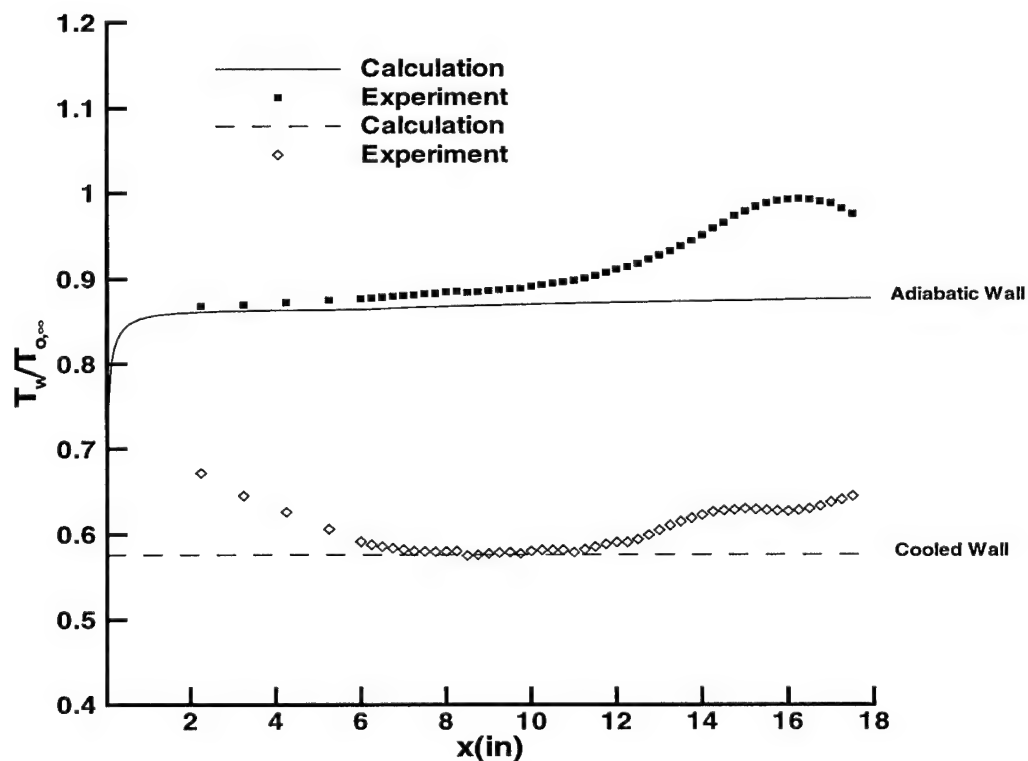


Figure 4.16. Effect of Wall Cooling on Surface Temperature Distribution, 91-6 Model

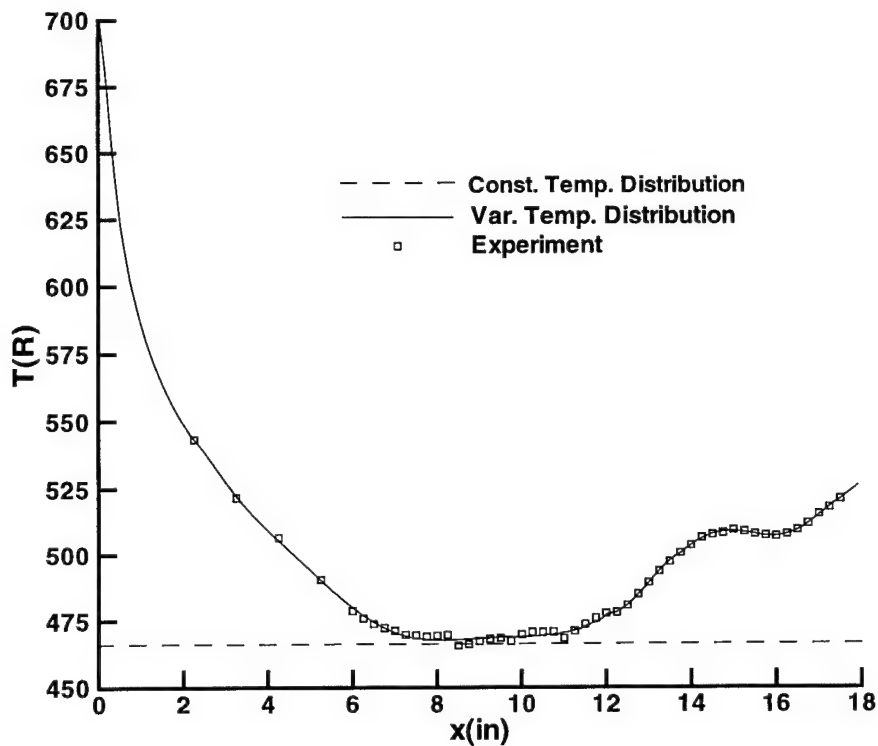


Figure 4.17. Curve Fit to 91-6 Cooled Model Experimentally Measured Surface Temperature Distribution

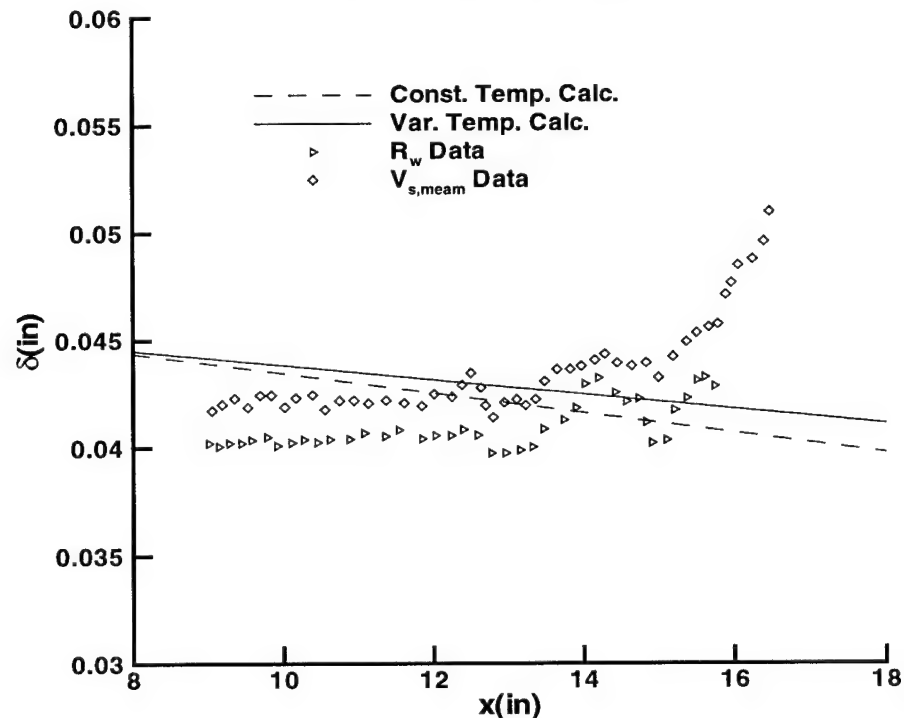


Figure 4.18. Effect of Initial Temperature Profile on Boundary Layer Thickness Distribution for 91-6 Cooled Model

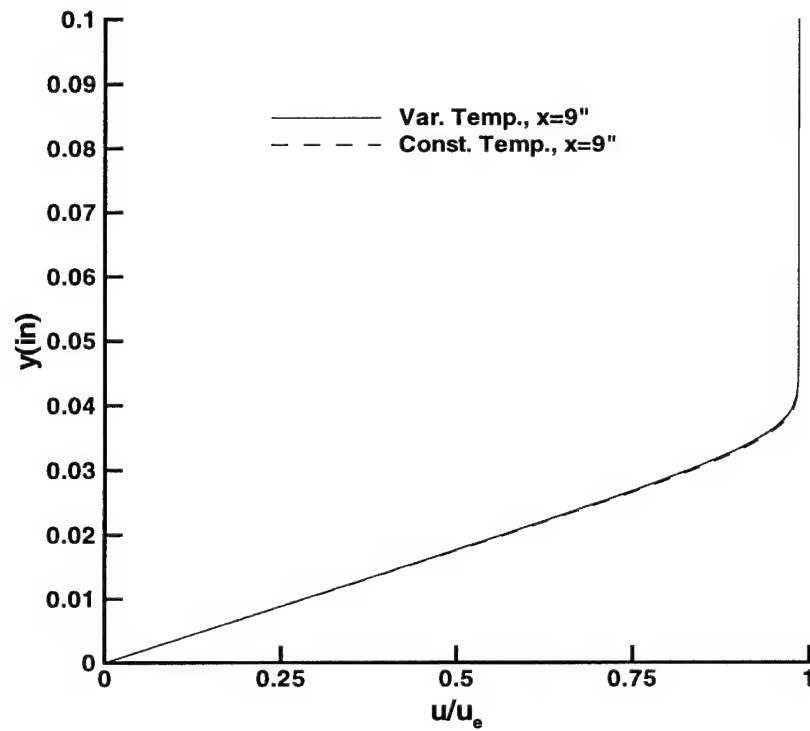


Figure 4.19. Velocity Profiles at $x=9"$ for 91-6 Cooled Model with Constant and Variable Wall Temperature Boundary Conditions

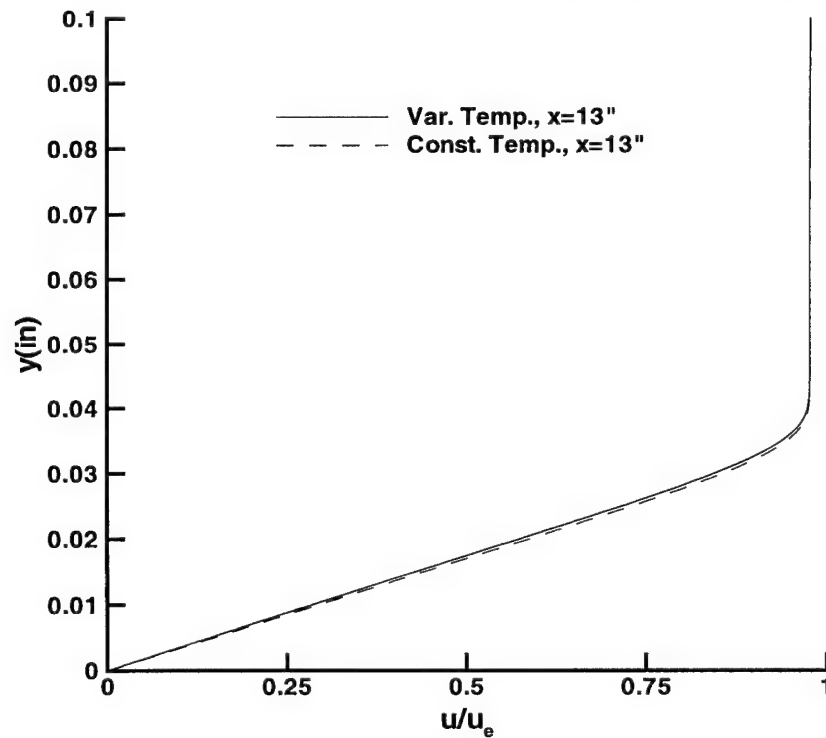


Figure 4.20. Velocity Profiles at $x=13"$ for 91-6 Cooled Model with Constant and Variable Wall Temperature Boundary Conditions

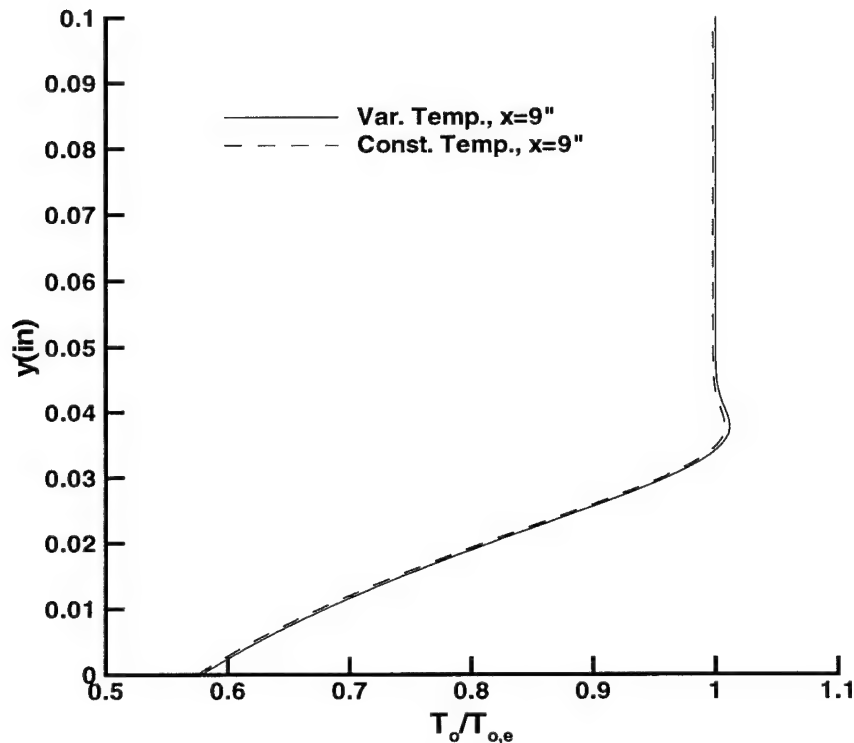


Figure 4.21. Total Temperature Profiles at $x=9"$ for 91-6 Cooled Model with Constant Variable Wall Temperature Boundary Conditions

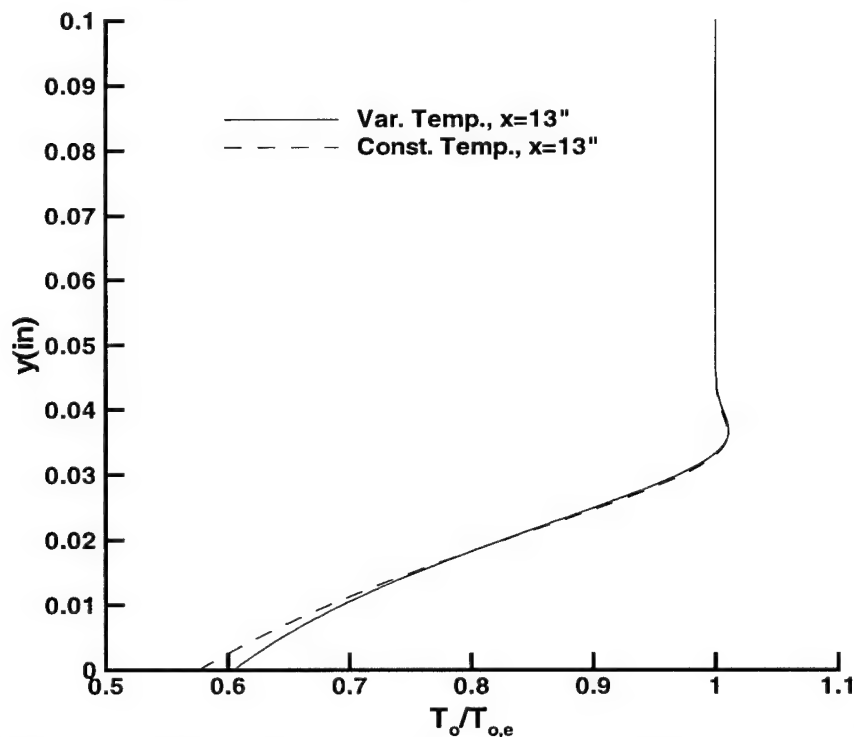


Figure 4.22. Total Temperature Profiles at $x=13"$ for 91-6 Cooled Model with Constant Variable Wall Temperature Boundary Conditions

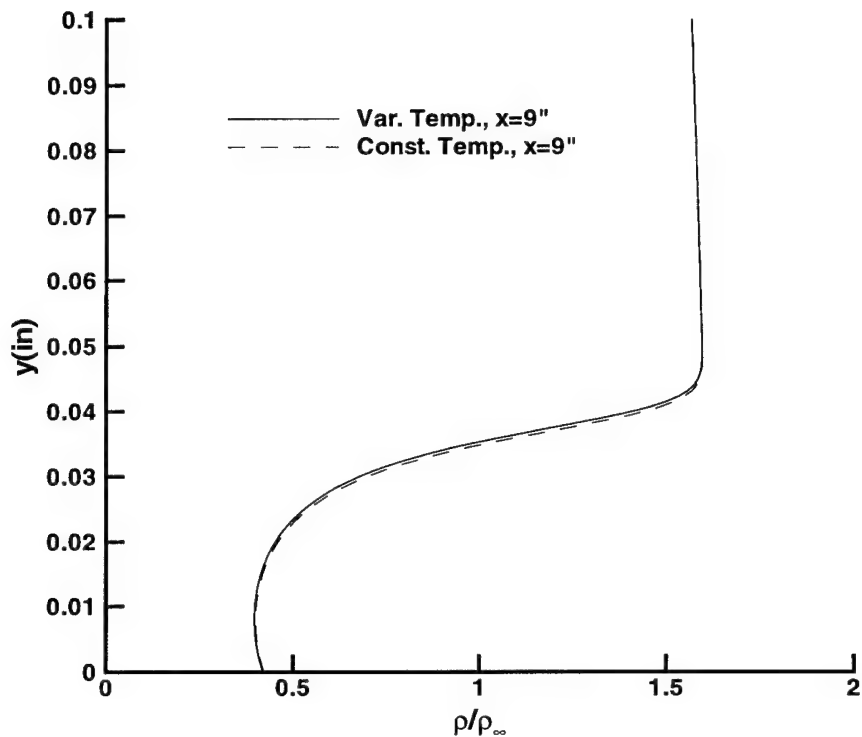


Figure 4.23. Density Profiles at $x=9''$ for 91-6 Cooled Model with Constant and Variable Wall Temperature Boundary Conditions

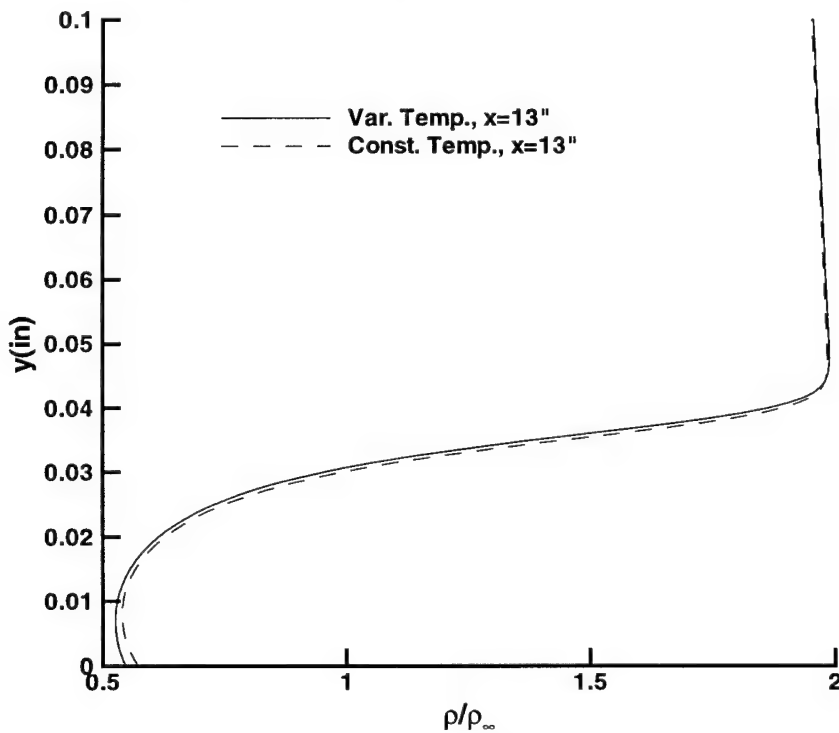


Figure 4.24. Density Profiles at $x= 13''$ for 91-6 Cooled Model with Constant and Variable Wall Temperature Boundary Conditions

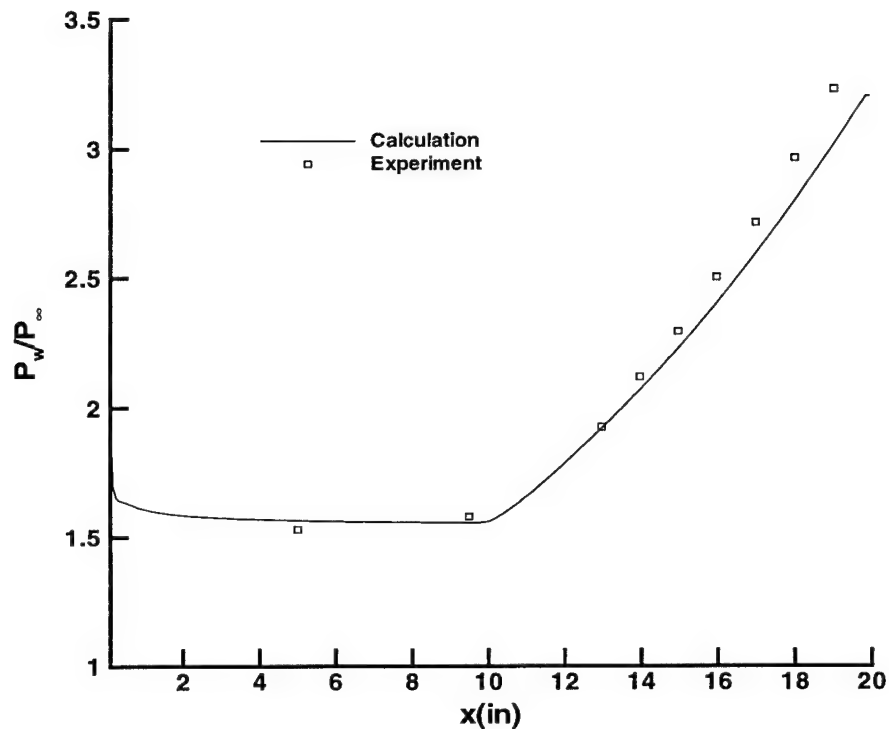


Figure 4.25. Pressure Distribution for 93-10 Adiabatic Model

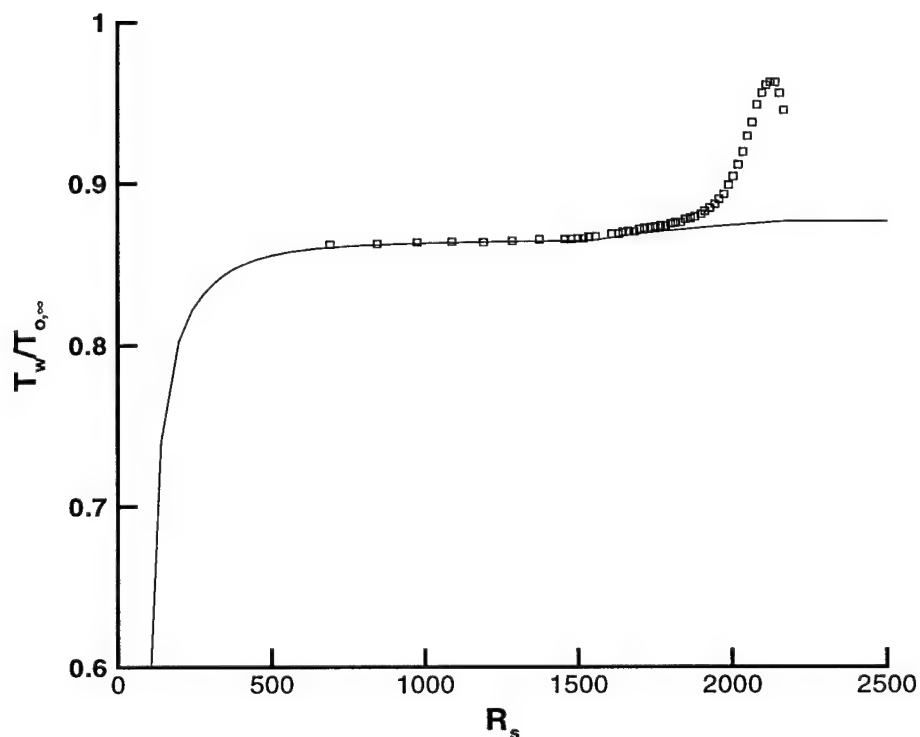


Figure 4.26. Temperature Distribution for 93-10 Adiabatic Model

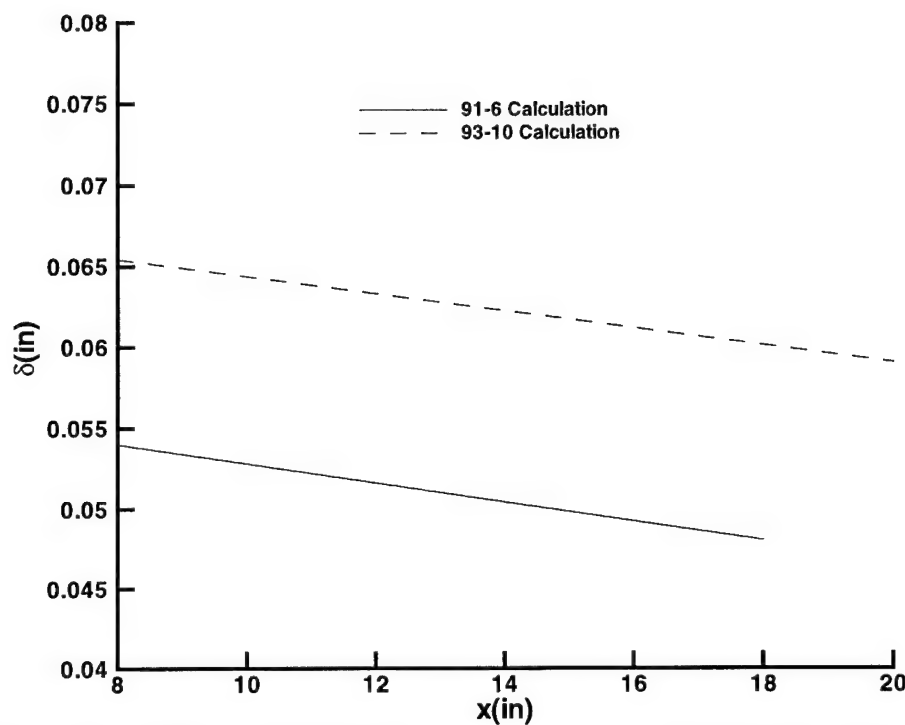


Figure 4.27. Effect of Adverse Pressure Gradient on Boundary Layer Thickness Distribution

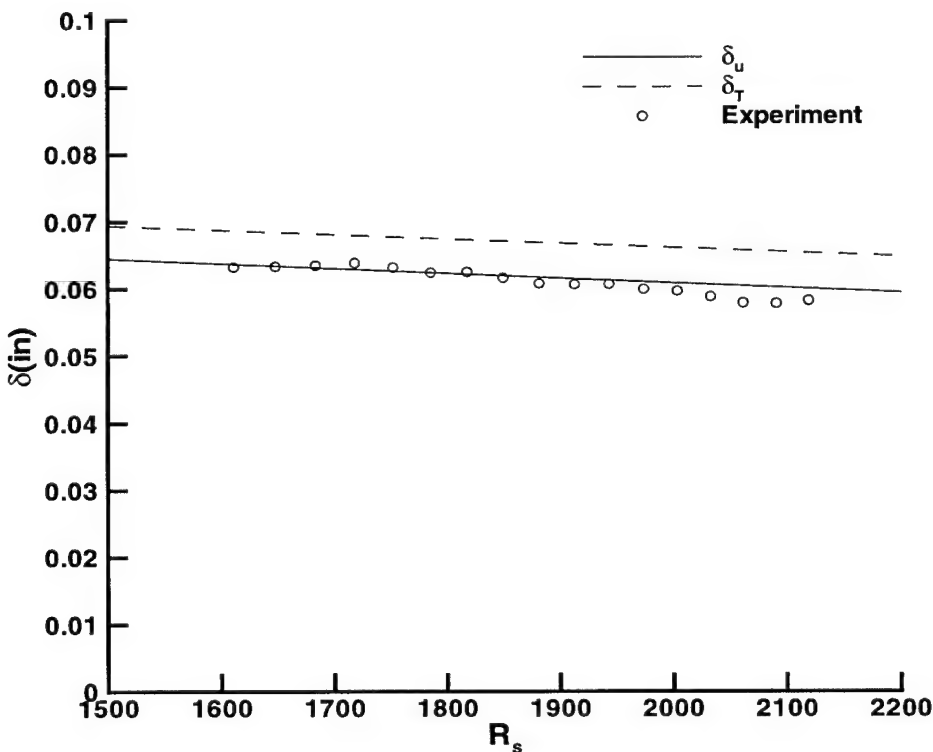


Figure 4.28. Boundary Layer Thickness Distribution for 93-10 Adiabatic Model

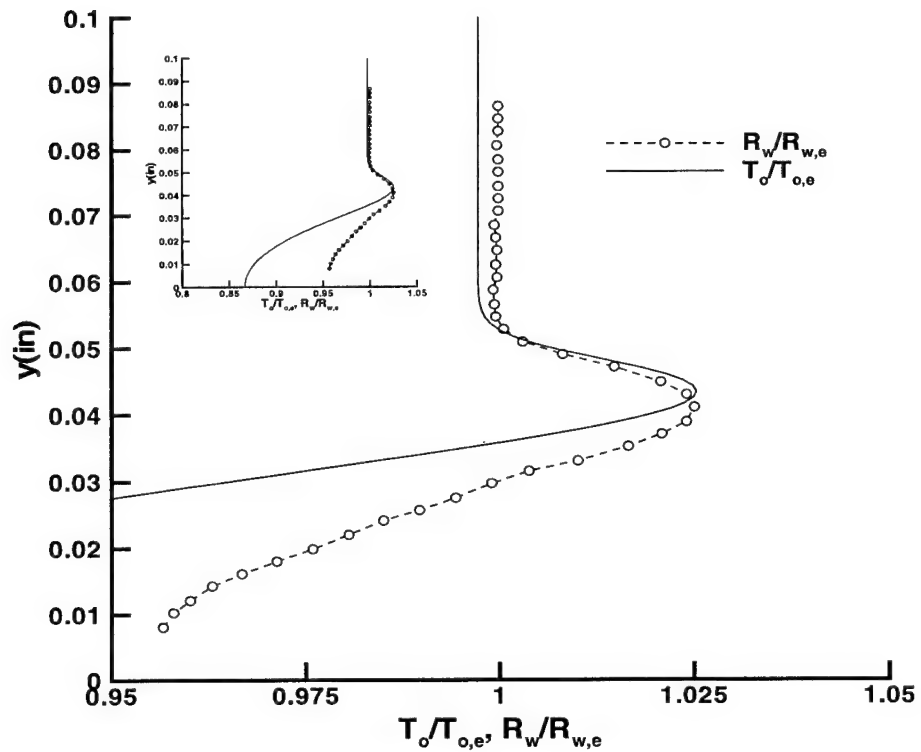


Figure 4.29. Comparison of Calculated Total Temperature and Normalized Wire Resistance Obtained in Low Overheat at $x=9''$, 91-6 Adiabatic Model

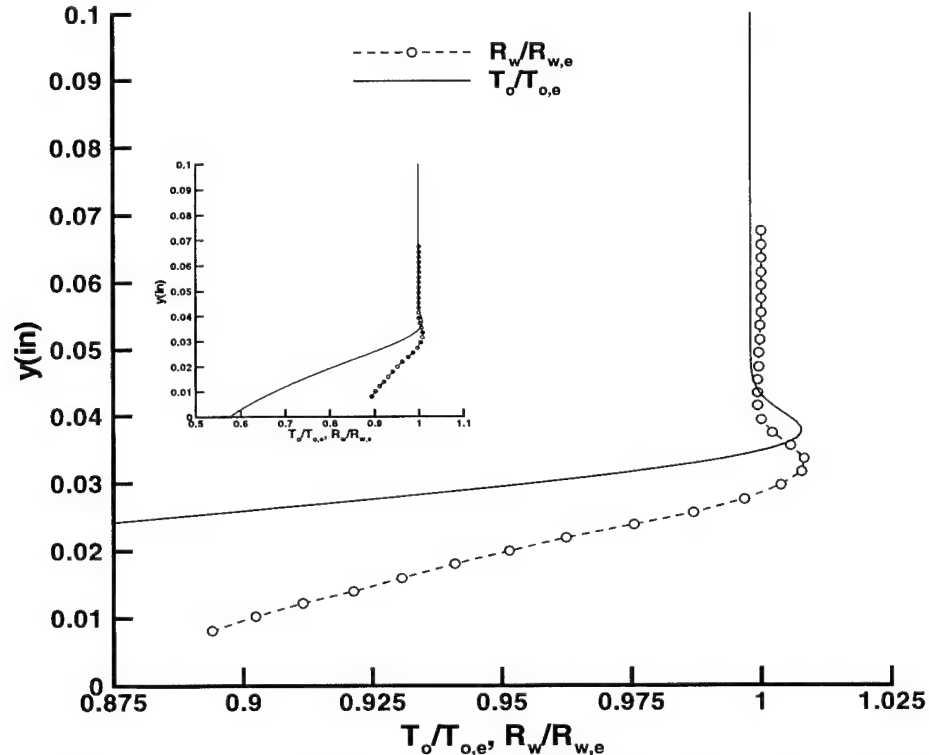


Figure 4.30. Comparison of Calculated Total Temperature and Normalized Wire Resistance Obtained in Low Overheat at $x=9''$, 91-6 Cooled Model

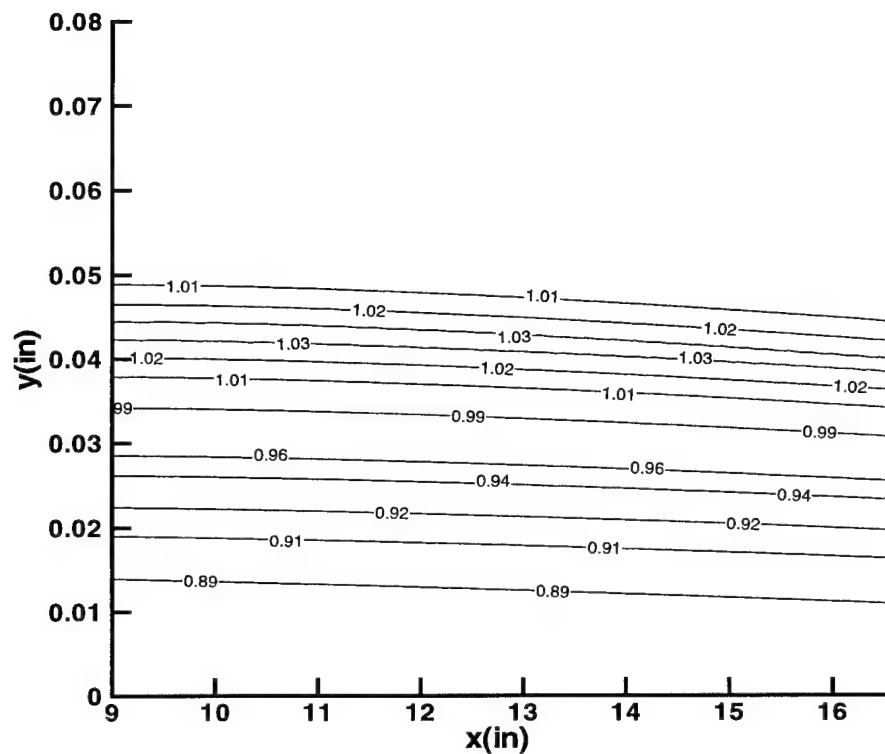


Figure 4.31. Normalized Total Temperature Contour Plot, 91-6 Adiabatic Model

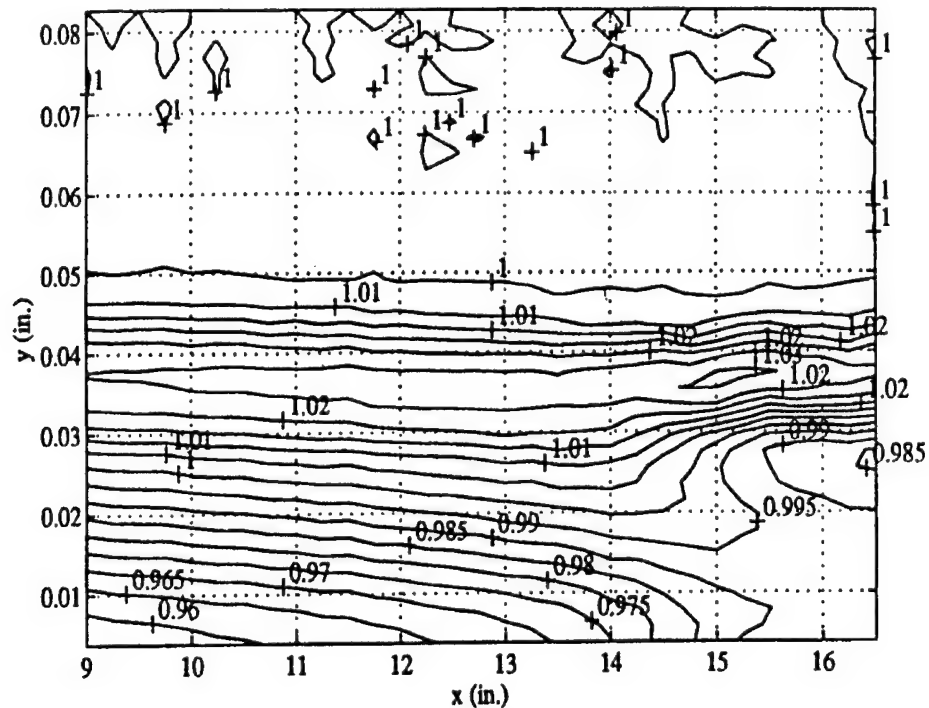


Figure 4.32. Contour Plot of Normalized R_w Obtained in Low Overheat, 91-6 Adiabatic Model (Blanchard and Selby, 1996)

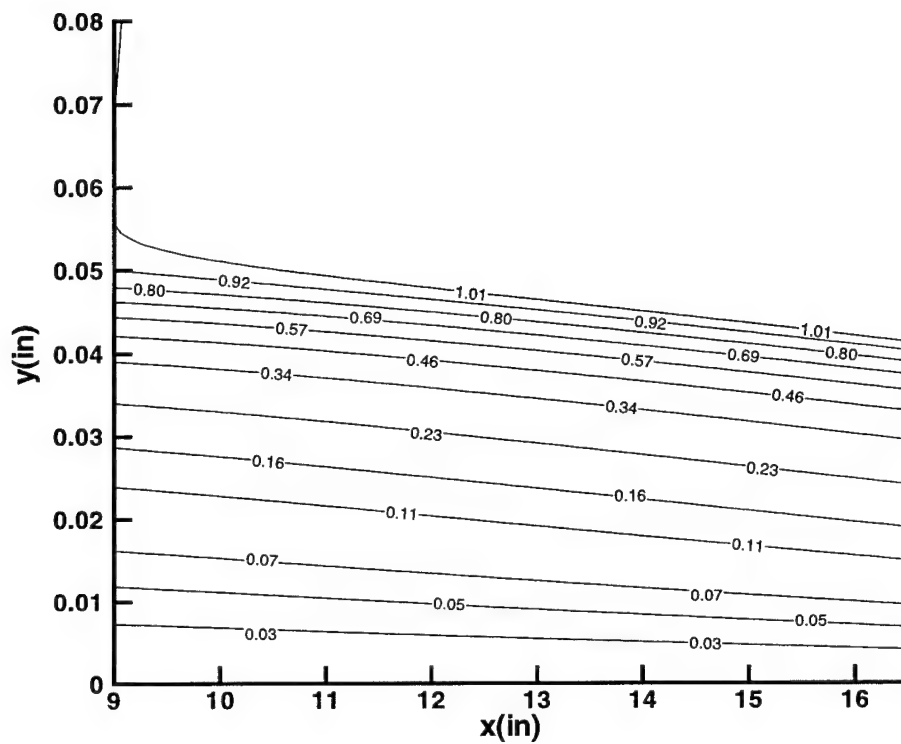


Figure 4.33. Normalized Mass Flux Contour Plot, 91-6 Adiabatic Model

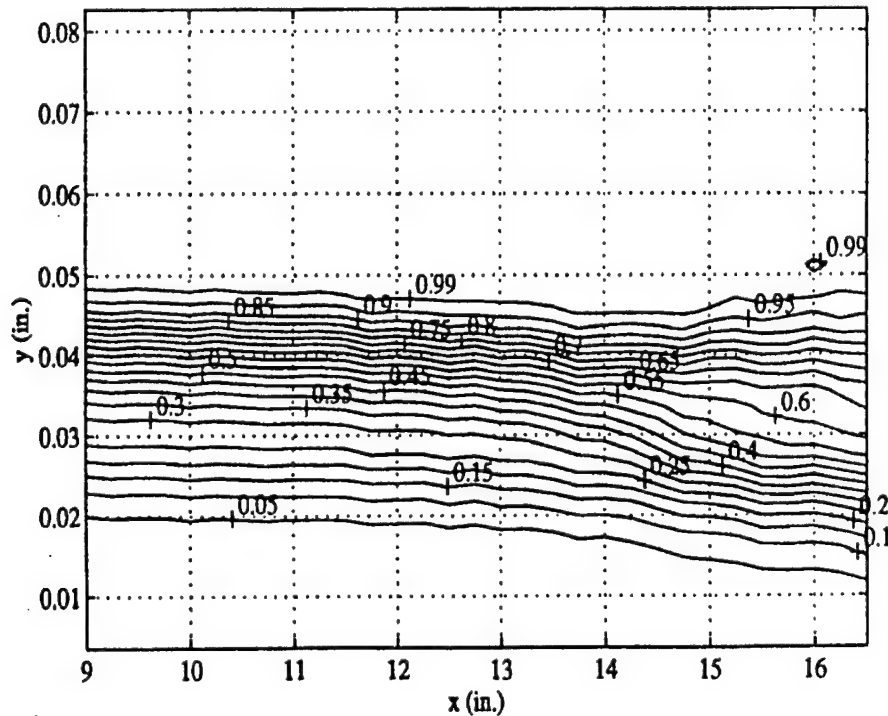


Figure 4.34. Contour Plot of Normalized $V_{s,mean}$ Obtained in High Overheat, 91-6 Adiabatic Model (Blanchard and Selby, 1996)

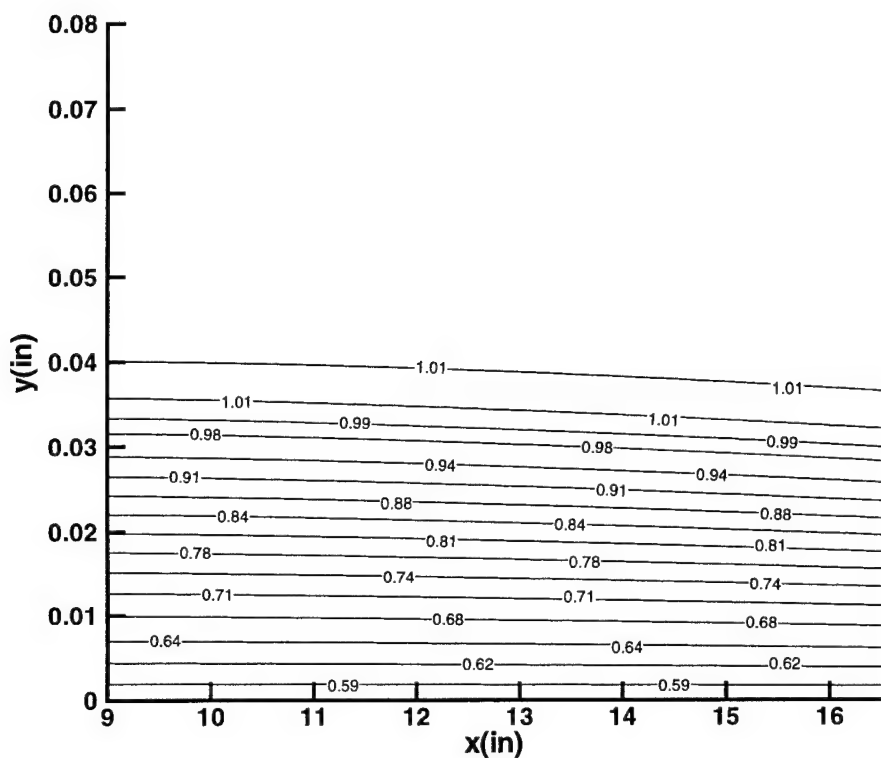


Figure 4.35. Normalized Total Temperature Contour Plot, 91-6 Cooled Model

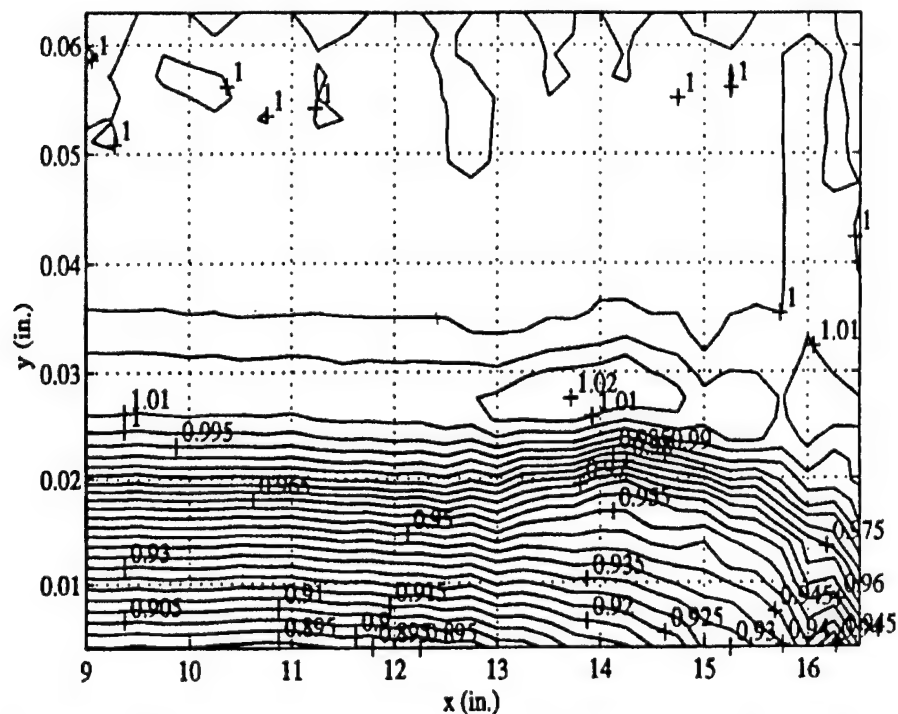


Figure 4.36. Contour Plot of Normalized R_w Obtained in Low Overheat, 91-6 Cooled Model (Blanchard and Selby, 1996)

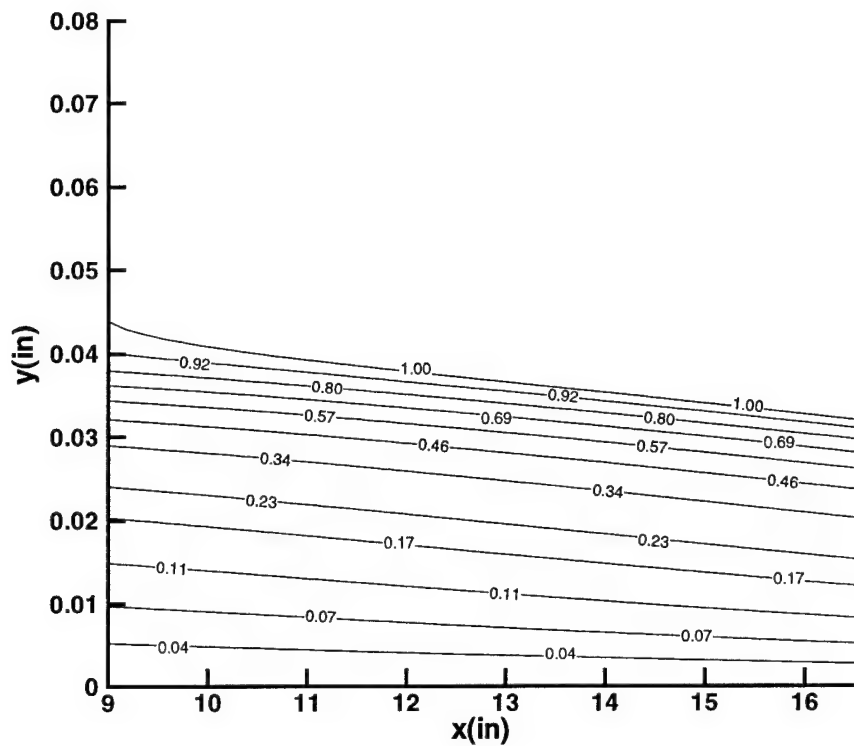


Figure 4.37. Normalized Mass Flux Contour Plot, 91-6 Cooled Model

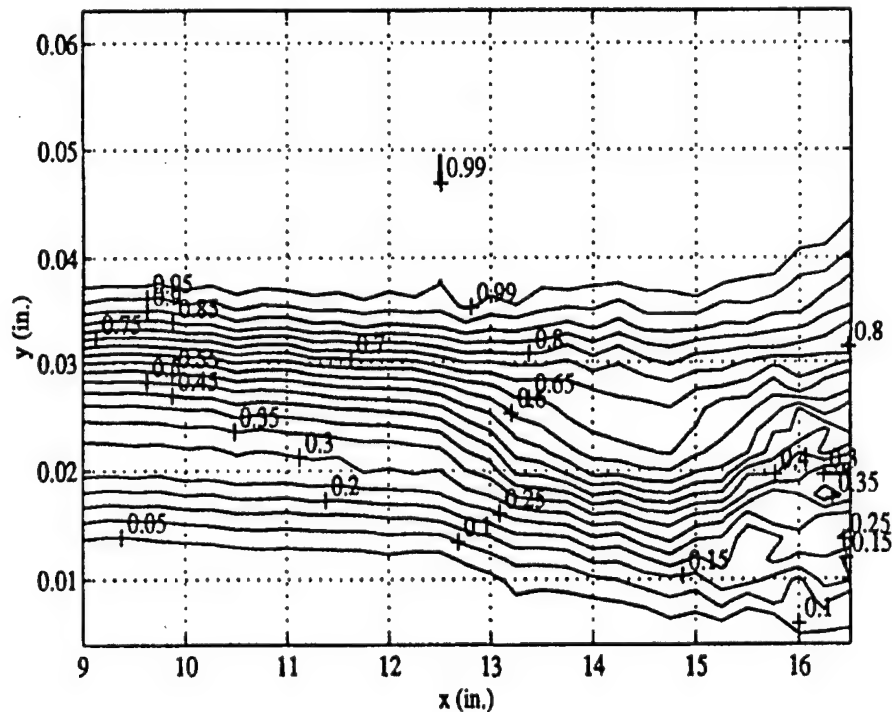


Figure 4.38. Contour Plot of Normalized $V_{s,\text{mean}}$ Obtained in High Overheat, 91-6 Cooled Model (Blanchard and Selby, 1996)

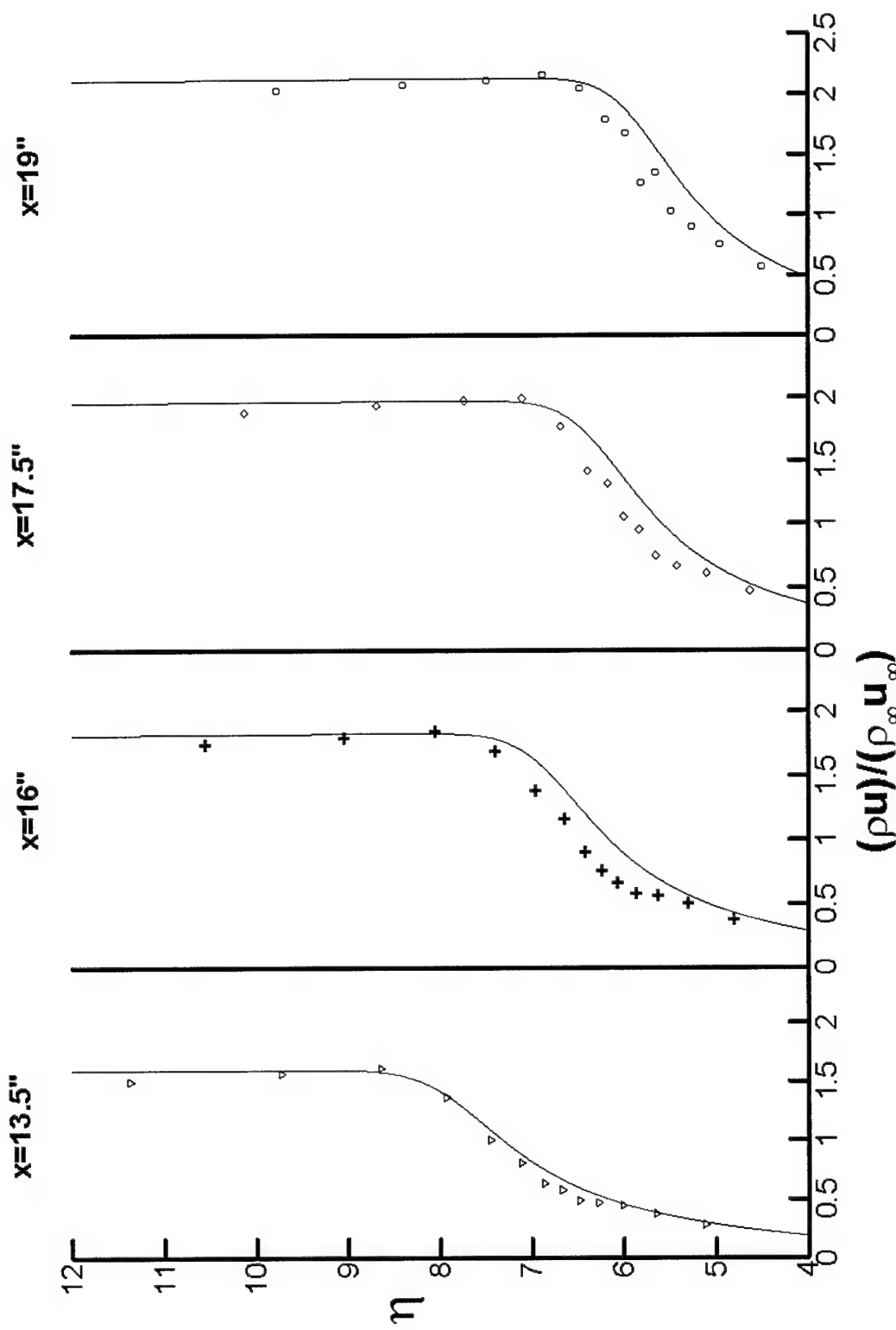


Figure 4.39. Mass Flux Profiles at Select Streamwise Locations, 93-10 Adiabatic Model
 (Lines are Computational Data, Symbols are Experimental Data)

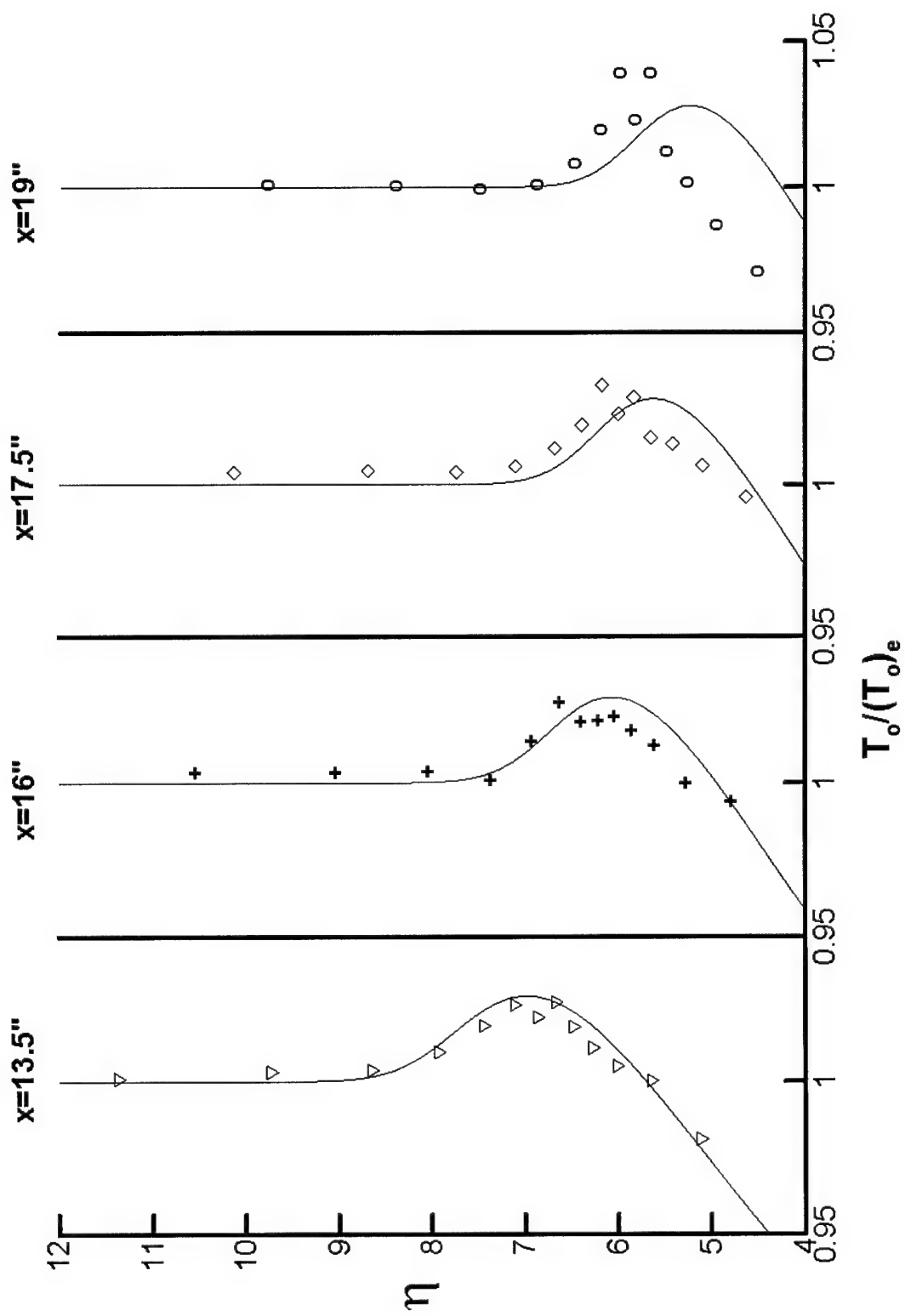


Figure 4.40. Total Temperature Profiles at Select Streamwise Locations, 93-10 Adiabatic Model
(Lines are Calculated Data, Symbols are Experimental Data)

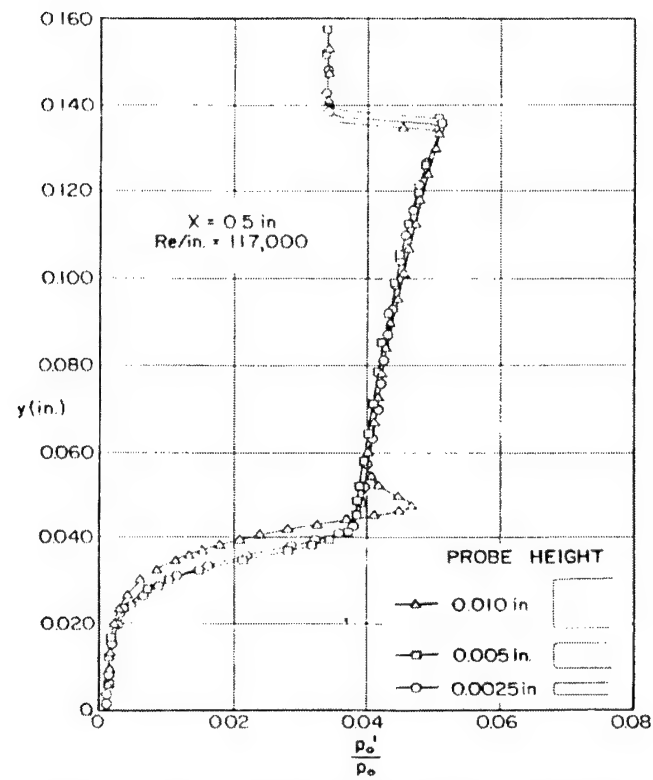


Figure 4.41. Pitot Pressure Profiles (Kendall, 1956)

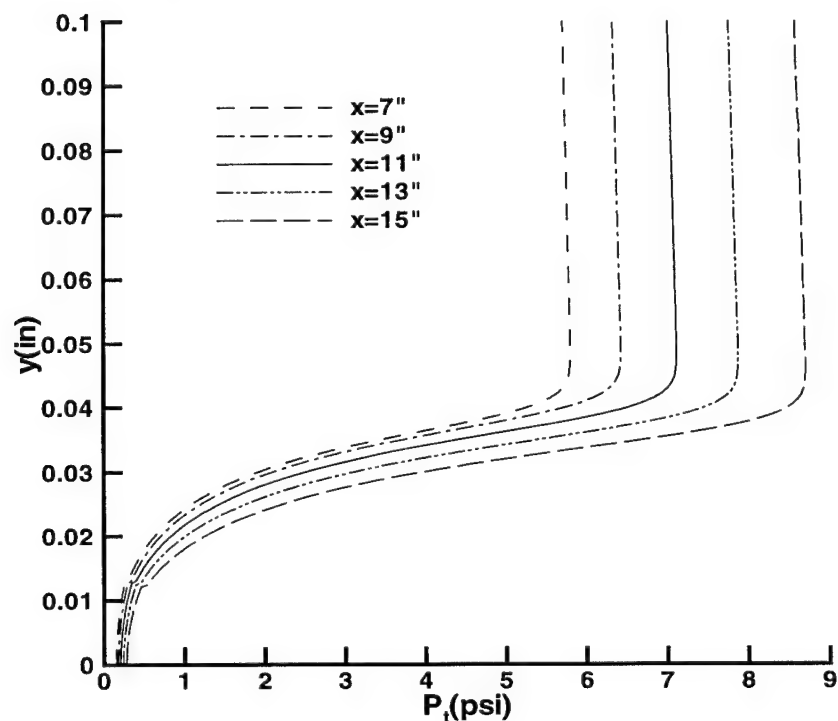


Figure 4.42. Pitot Pressure Distribution for Various x -locations Along 91-6 Cooled Model Surface

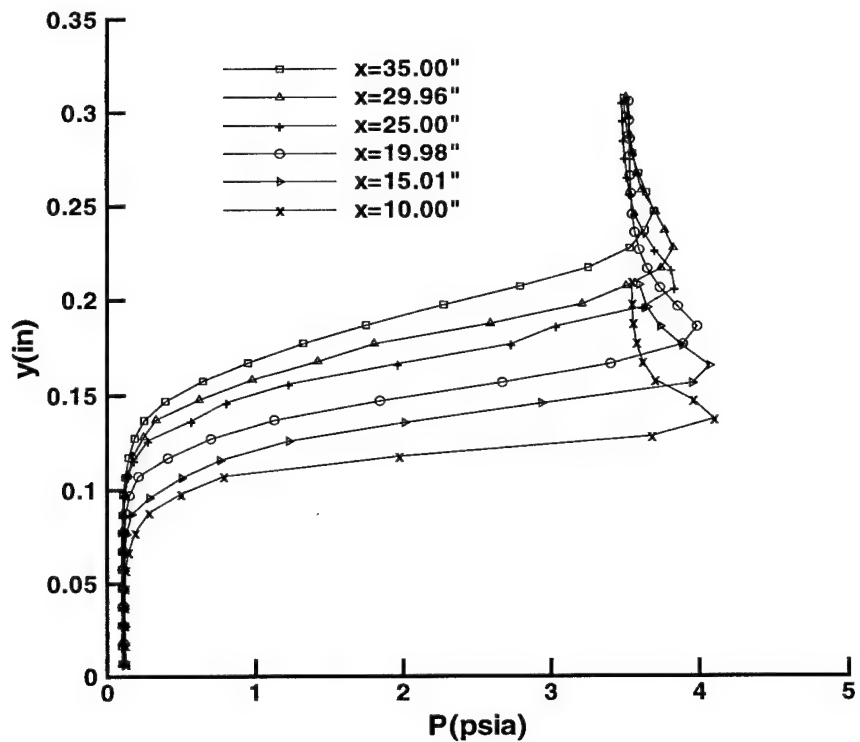
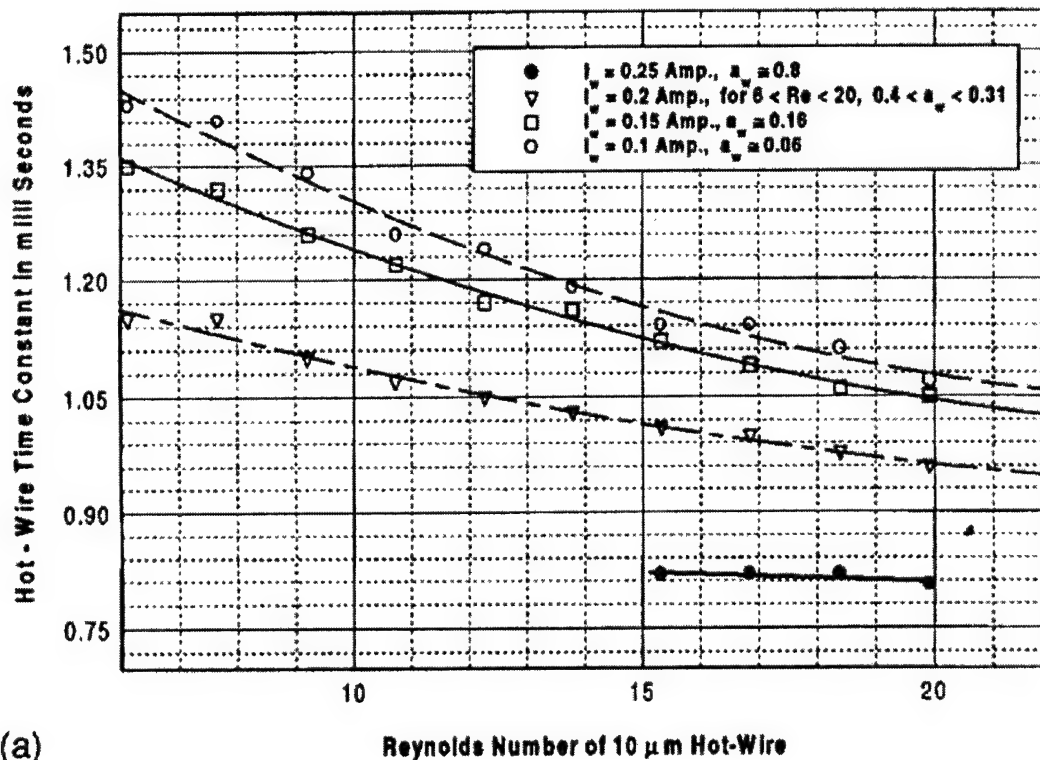
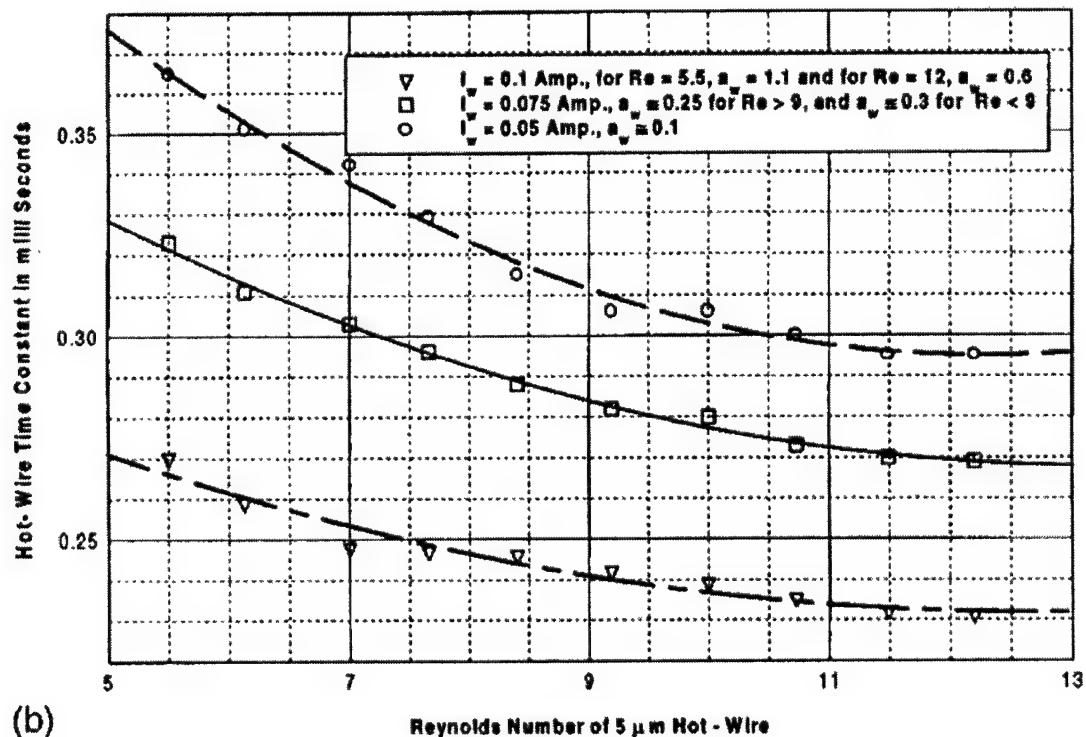


Figure 4.43. Pitot Pressure Distribution for Various x -locations for Stetson's Experiments (1983), (Schneider, 2000)



(a)



(b)

Figure 4.44. Time Constant Values as a Function of Hot-Wire Reynolds Numbers and Currents for a) 10 and b) $5 \mu\text{m}$ Hot-Wire (Sarma, 1999)

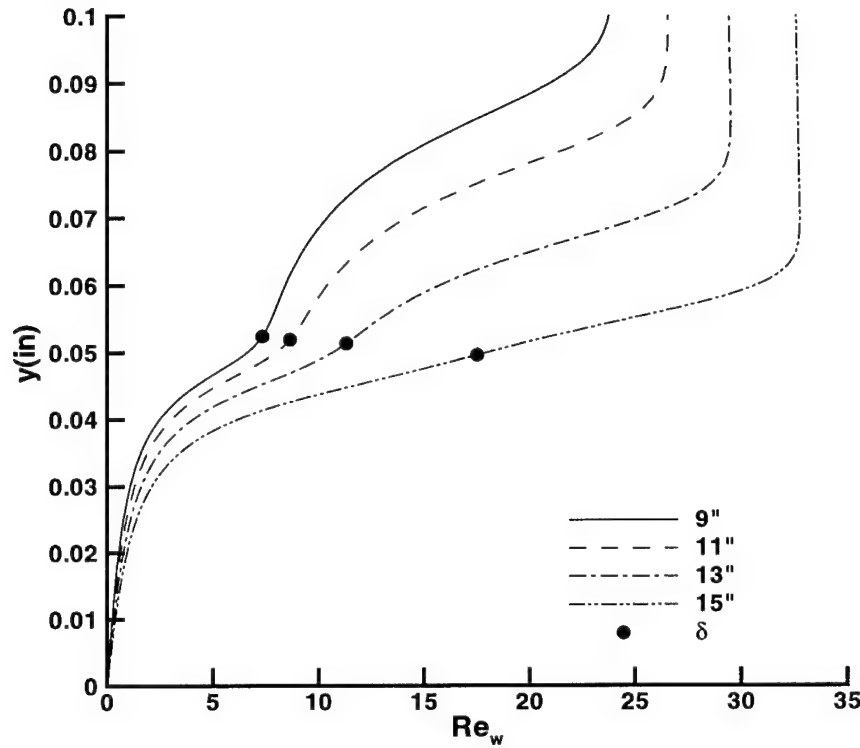


Figure 4.45. Wire Reynolds Number for 0.0001in Wire at Various Streamwise Locations, 91-6 Adiabatic Model

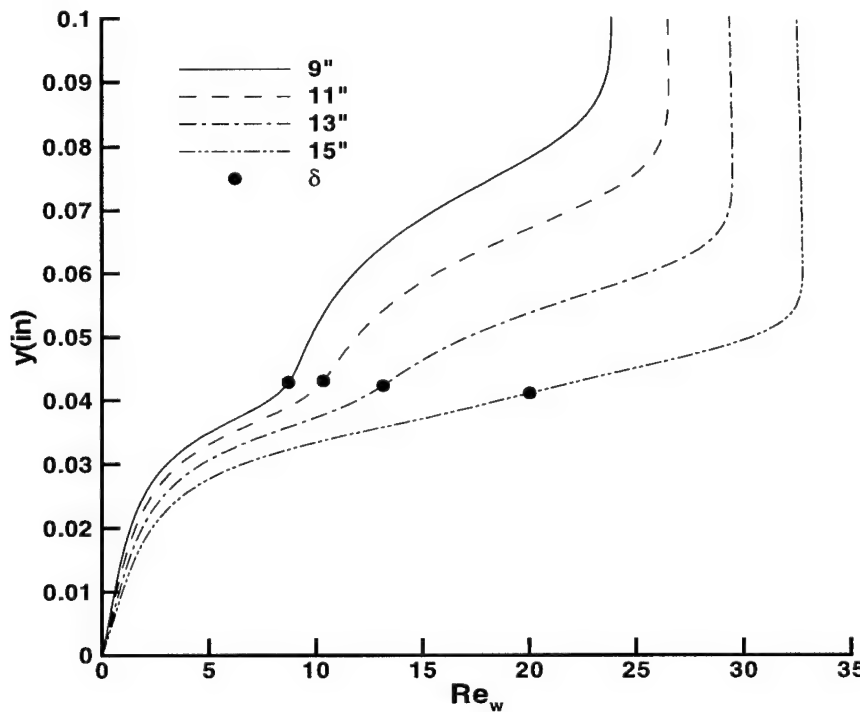


Figure 4.46. Wire Reynolds Number for 0.0001in Wire at Various Streamwise Locations, 91-6 Cooled Model

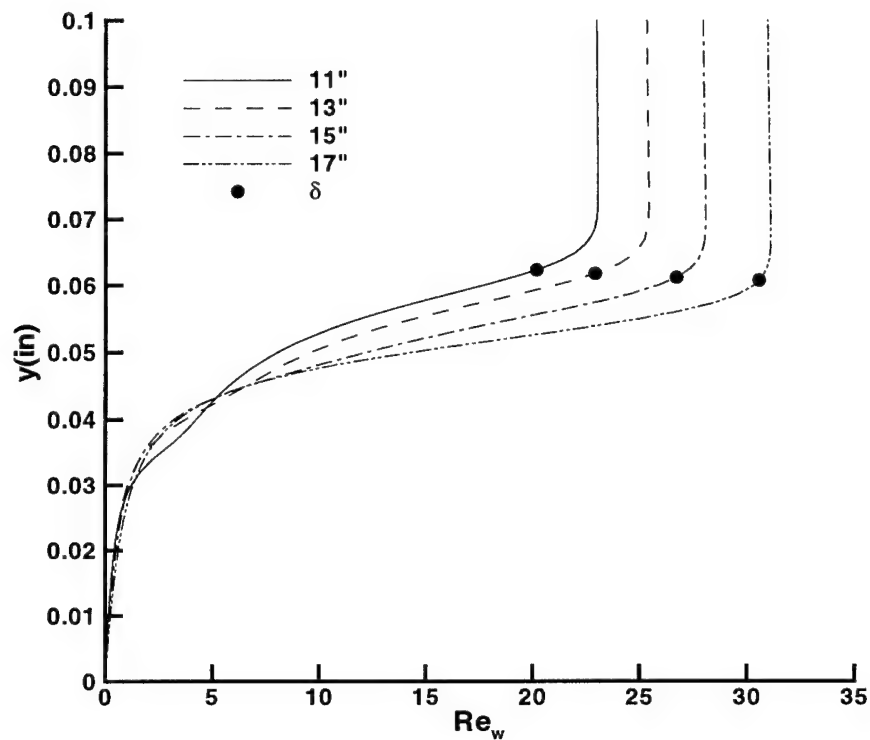


Figure 4.47. Wire Reynolds Number for 0.0001in Wire at Various Streamwise Locations, 93-10 Adiabatic Model

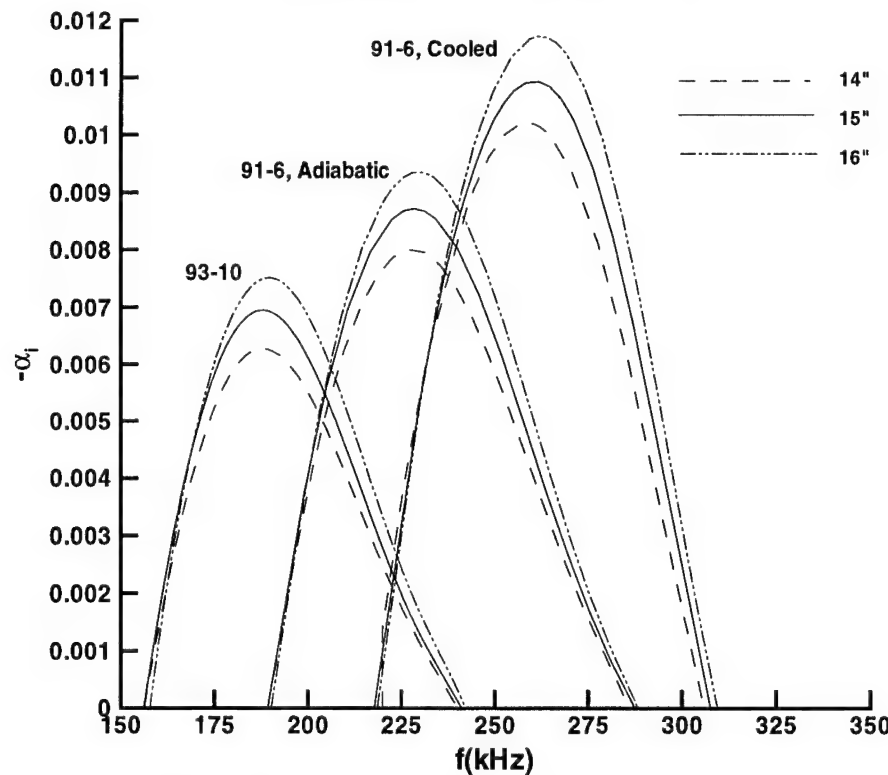


Figure 4.48. Amplification Rates for 91-6 and 93-10 Models

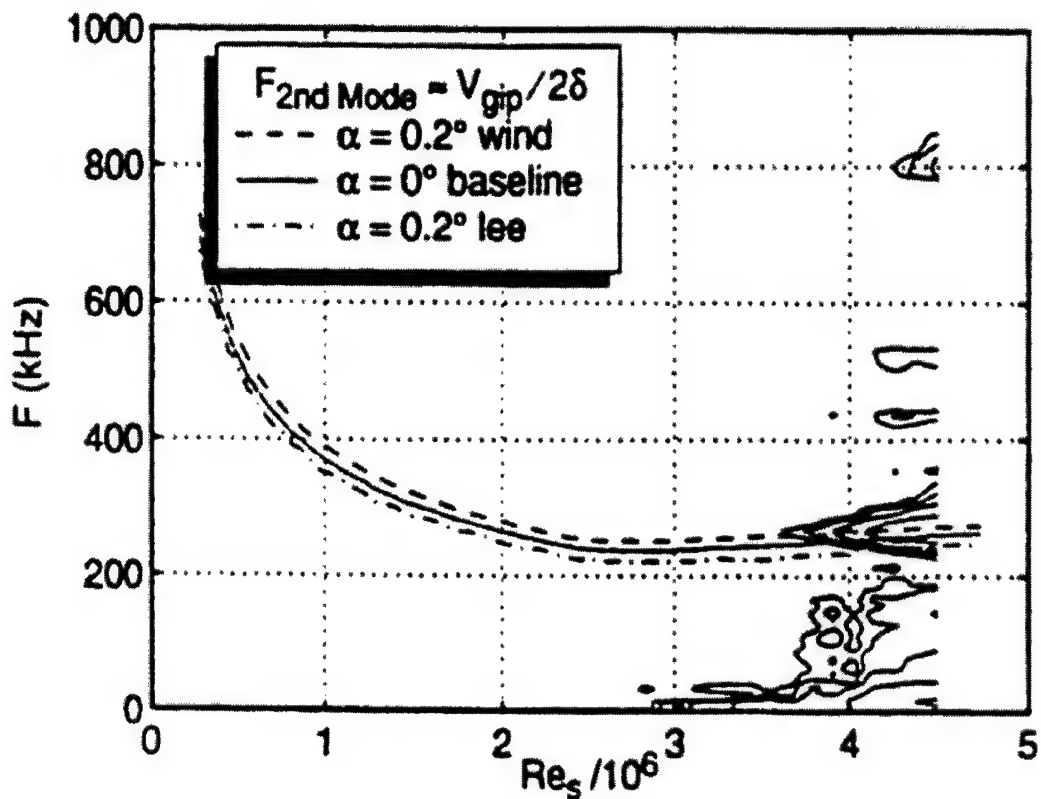


Figure 4.49. Estimated Second-Mode Disturbance Frequency with Measured N -Factor Contours for 0° Baseline Case (Doggett *et al*, 1997)

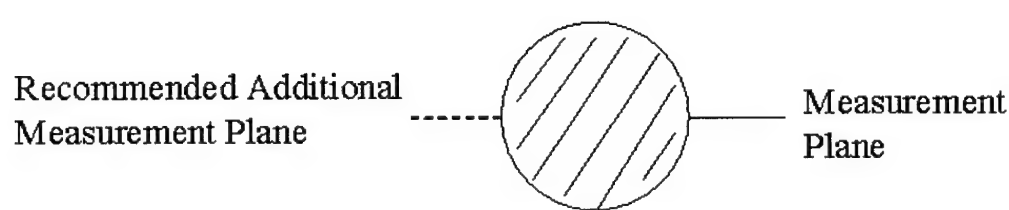


Figure 4.50. Hot-wire Measurement Location, Front View of Model

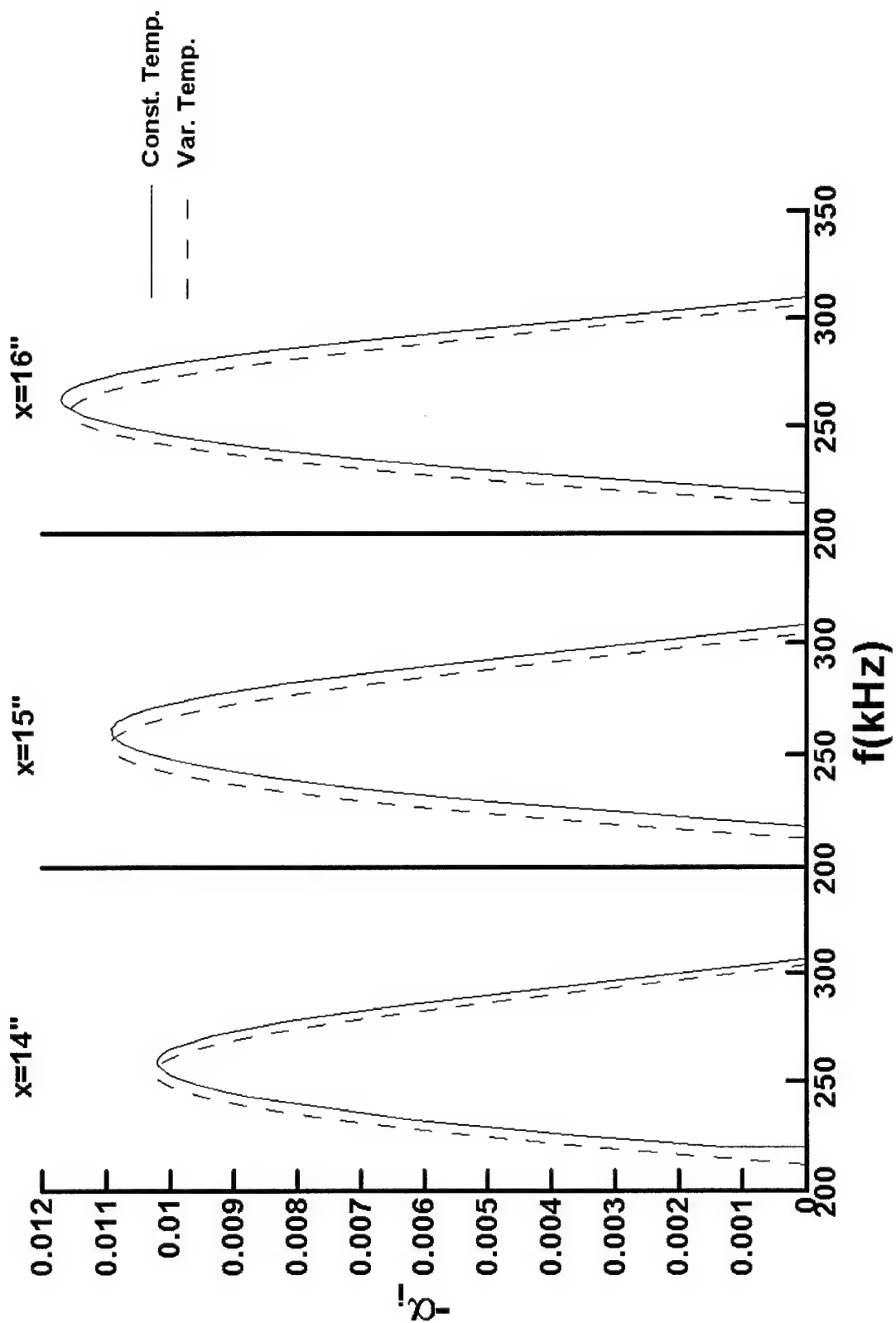


Figure 4.51. Effect of Variable Temperature Distribution on Amplification Rates, 91-6 Cooled Model

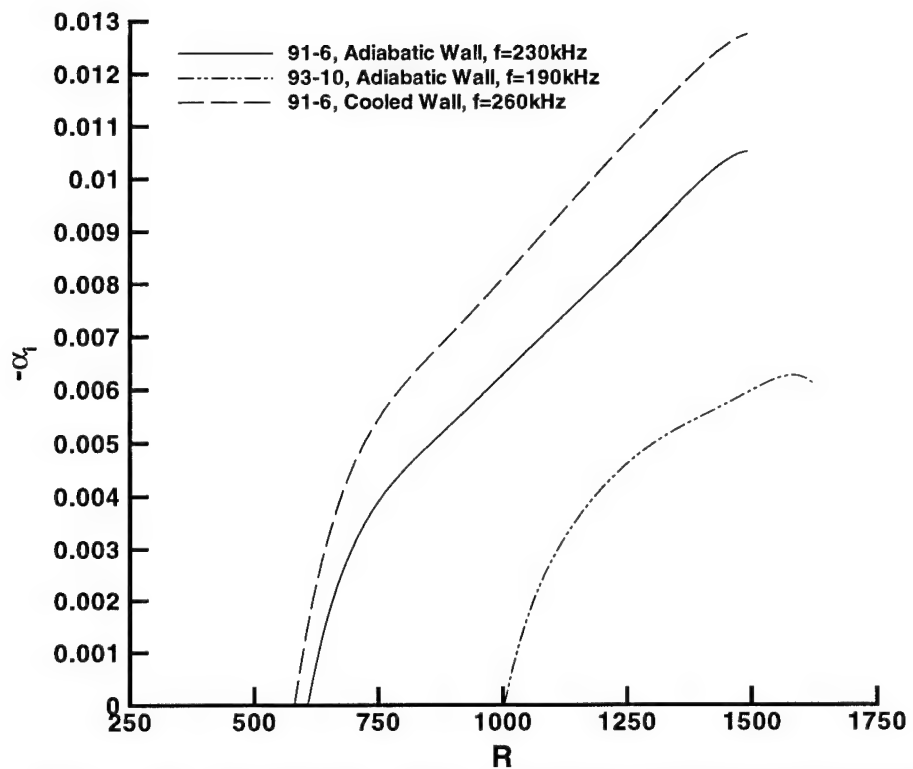


Figure 4.52. Amplification Rates for Peak Second Mode Frequencies

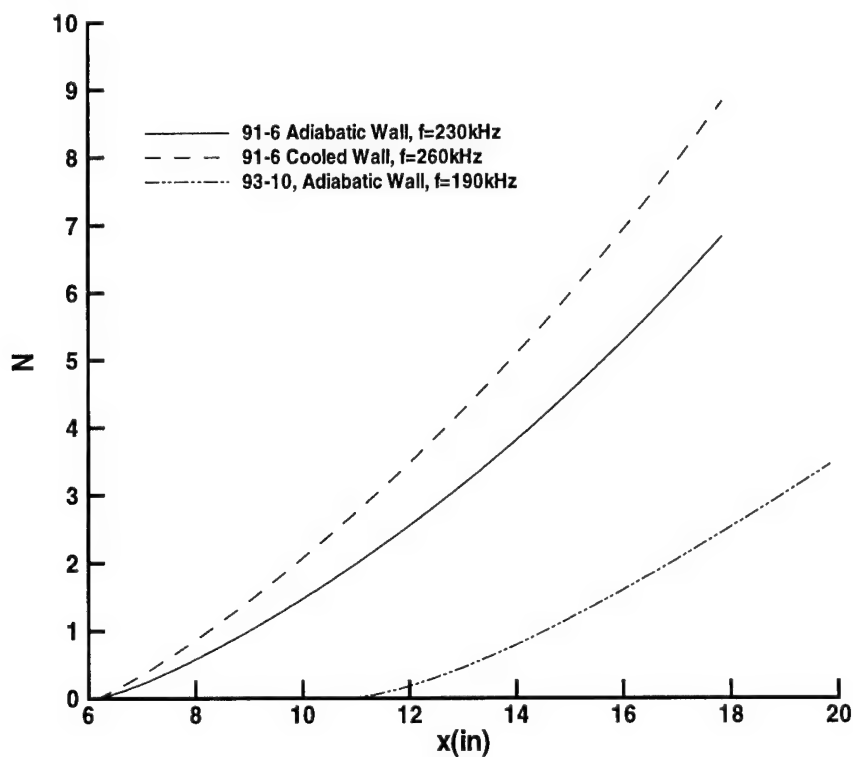


Figure 4.53. N-Factor Variation for Peak Second Mode Frequencies

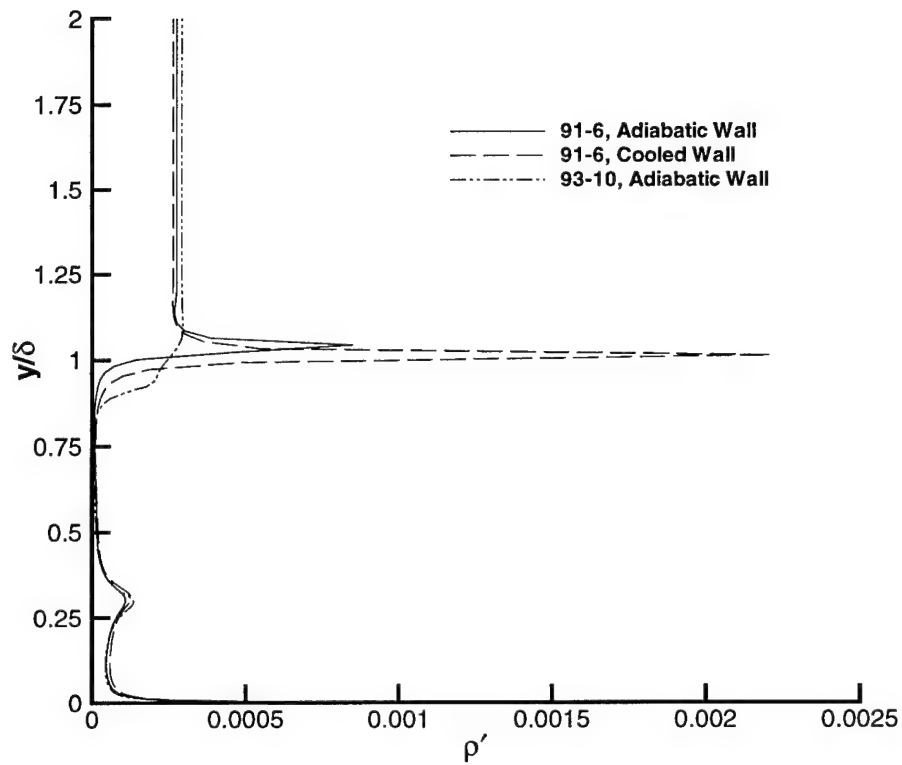


Figure 4.54. Density Eigenfunctions for 91-6 and 93-10 Models, $x=13''$

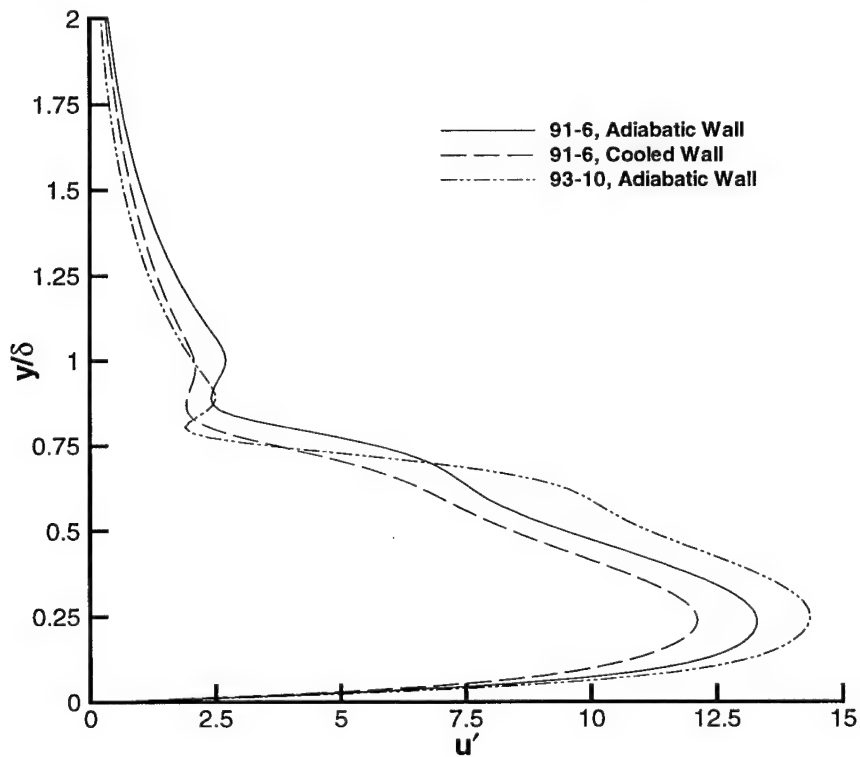


Figure 4.55. Velocity Eigenfunctions for 91-6 and 93-10 Models, $x=13''$

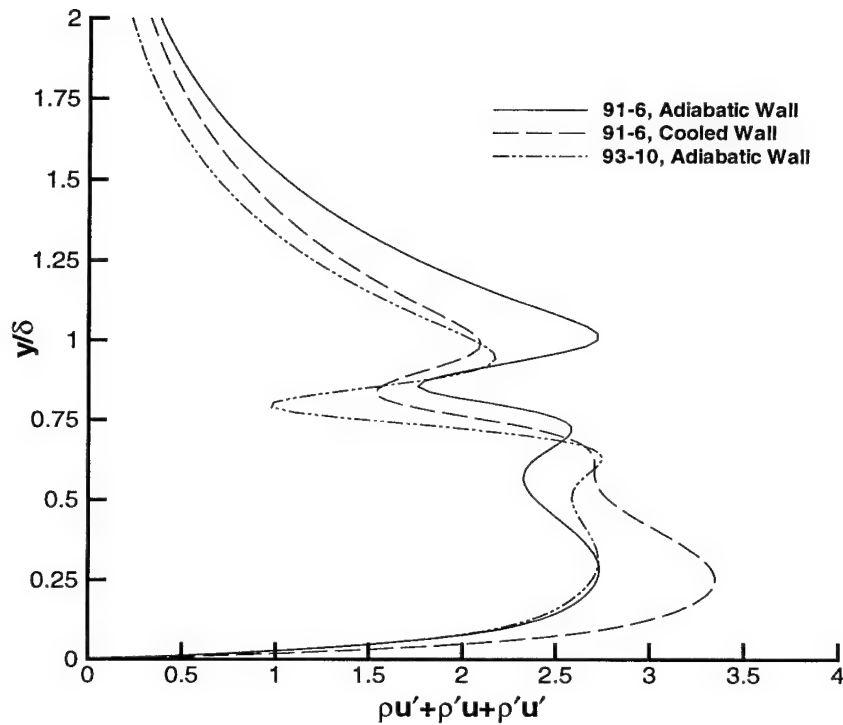


Figure 4.56. Mass Flux Eigenfunctions for 91-6 and 93-10 Models, $x=13''$

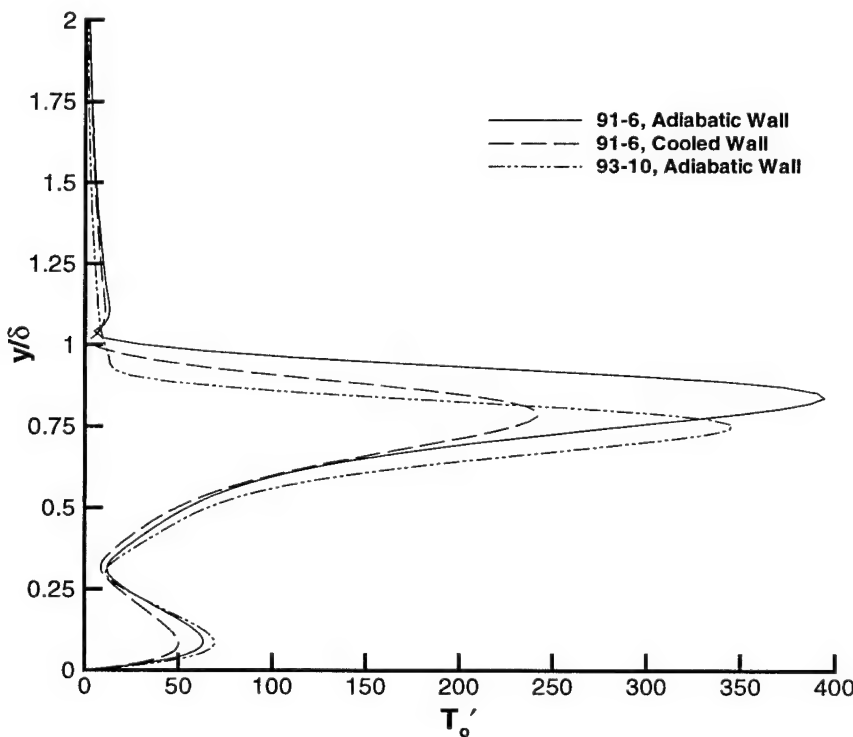


Figure 4.57. Total Temperature Eigenfunctions for 91-6 and 93-10 Models, $x=13''$

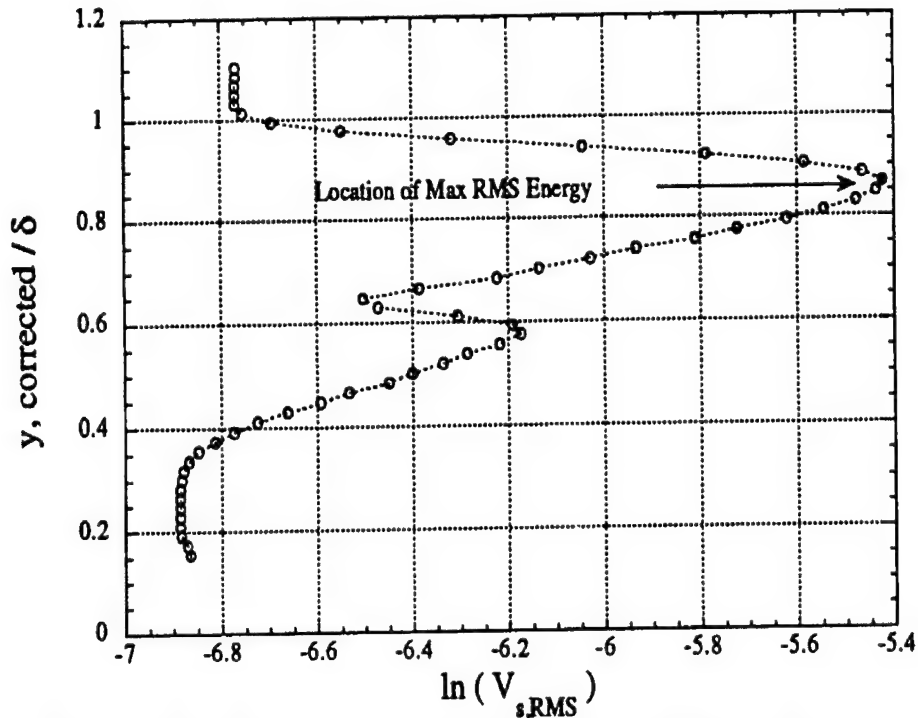


Figure 4.58. RMS Hot-wire Output for 91-6 Adiabatic Model at $x=9''$
(Blanchard and Selby, 1996)

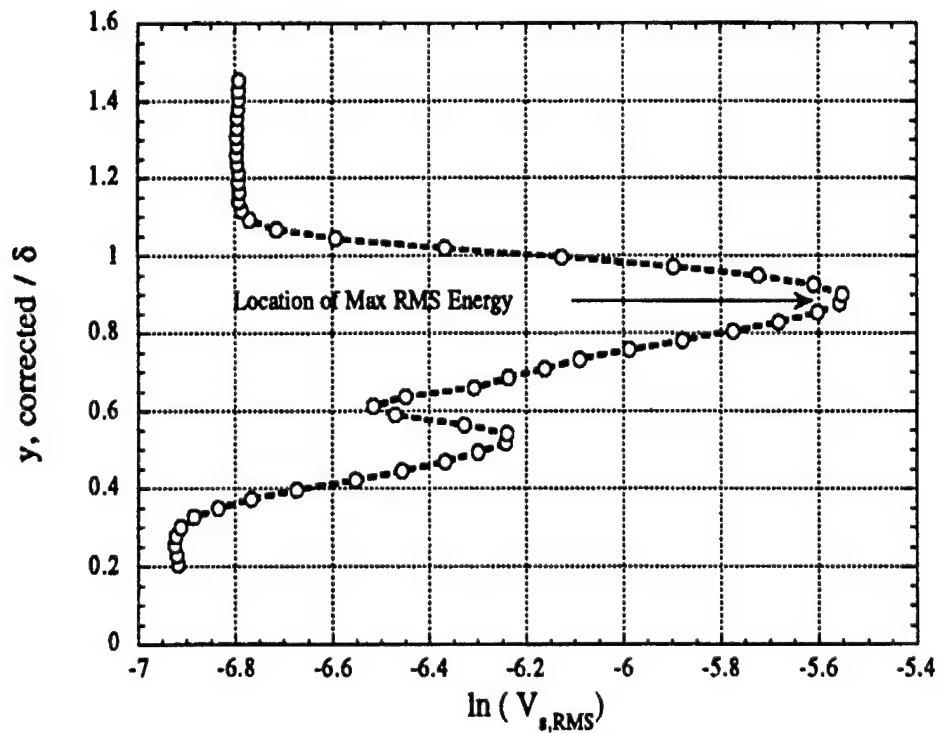


Figure 4.59. RMS Hot-wire Output for 91-6 Cooled Model at $x=9''$
(Blanchard and Selby, 1996)

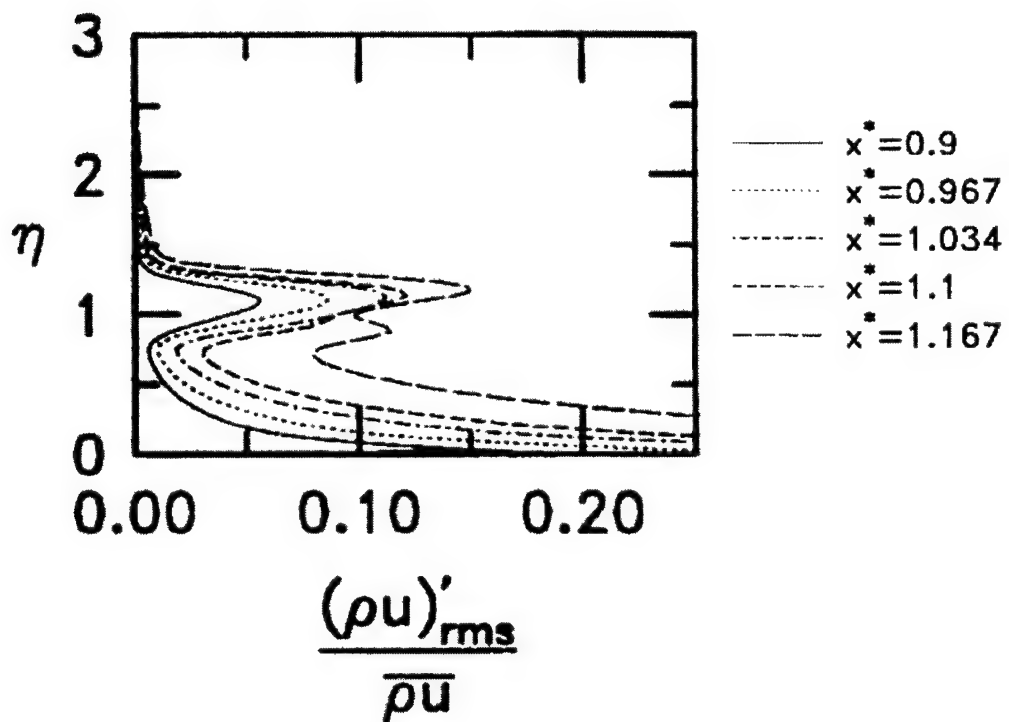


Figure 4.60. Streamwise Evolution of DNS Computed Mass Flux Fluctuations,
93-10 Model (Pruett and Chang, 1998)

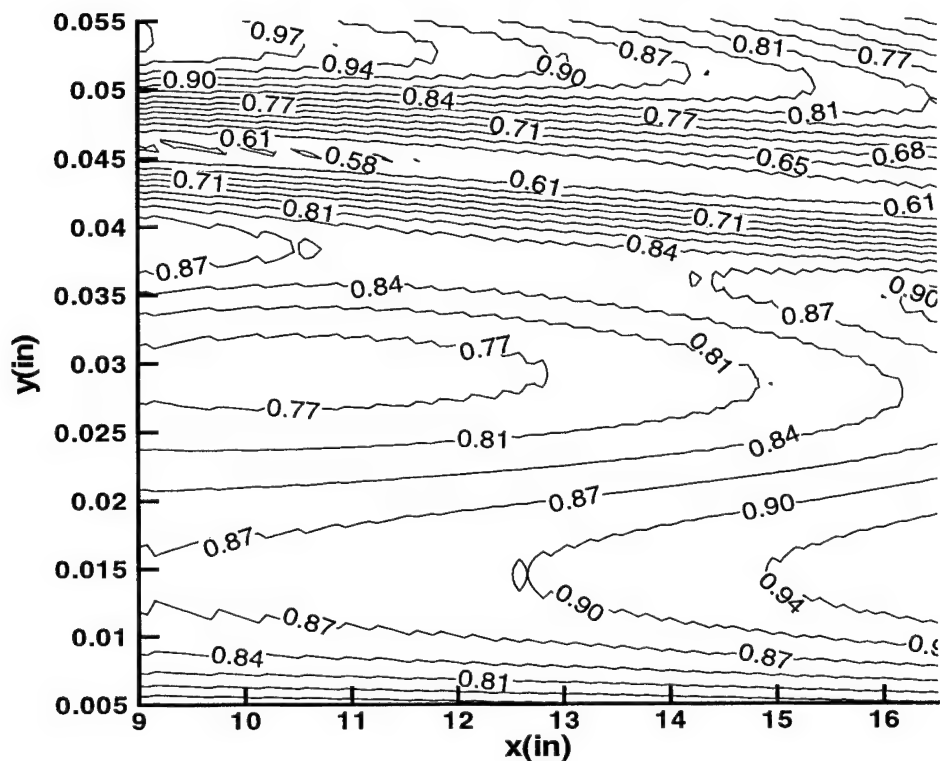


Figure 4.61. Normalized Mass Flux Contour Plot, 91-6 Adiabatic Model

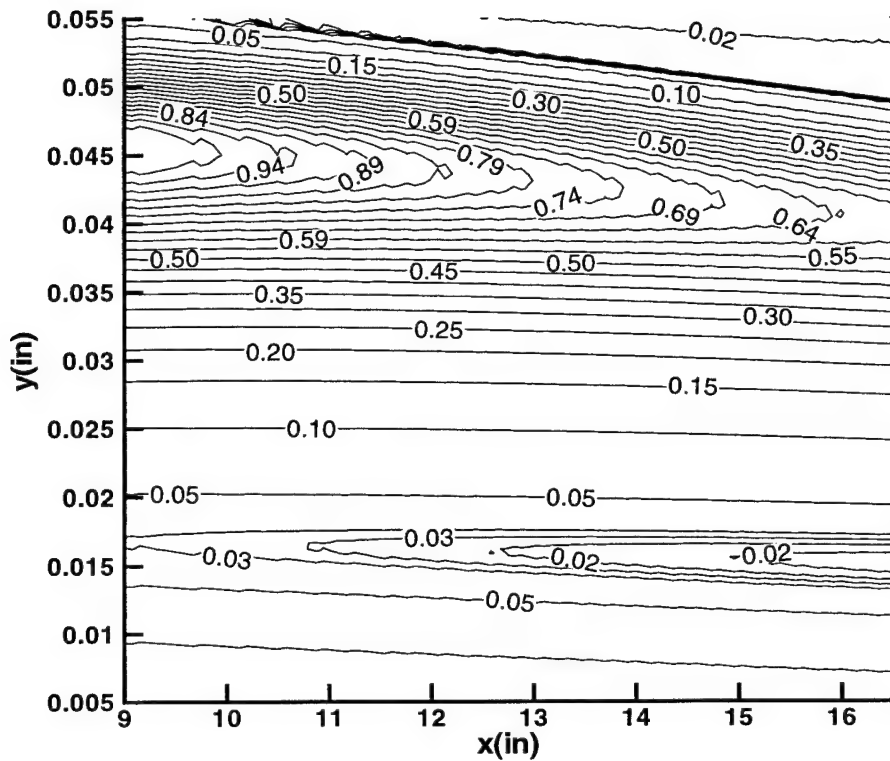


Figure 4.62. Normalized Total Temperature Contour Plot, 91-6 Adiabatic Model

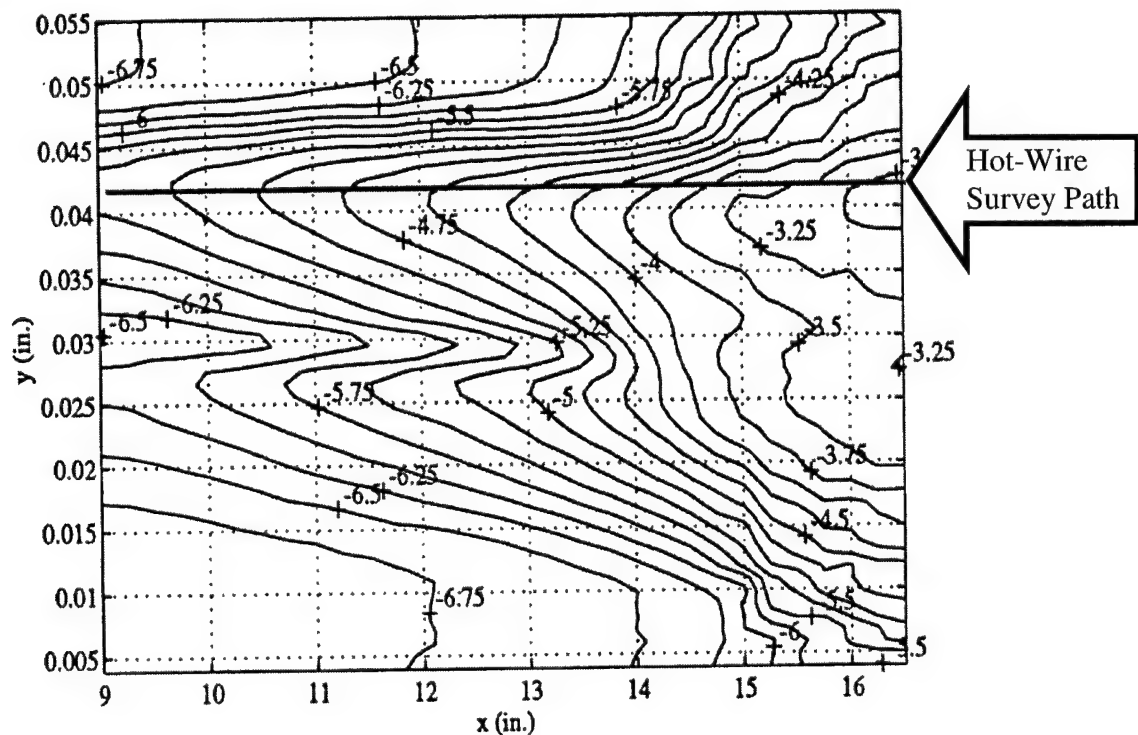


Figure 4.63. Hot-Wire Survey Path and RMS Contours for 91-6 Adiabatic Model
(Blanchard and Selby, 1996)

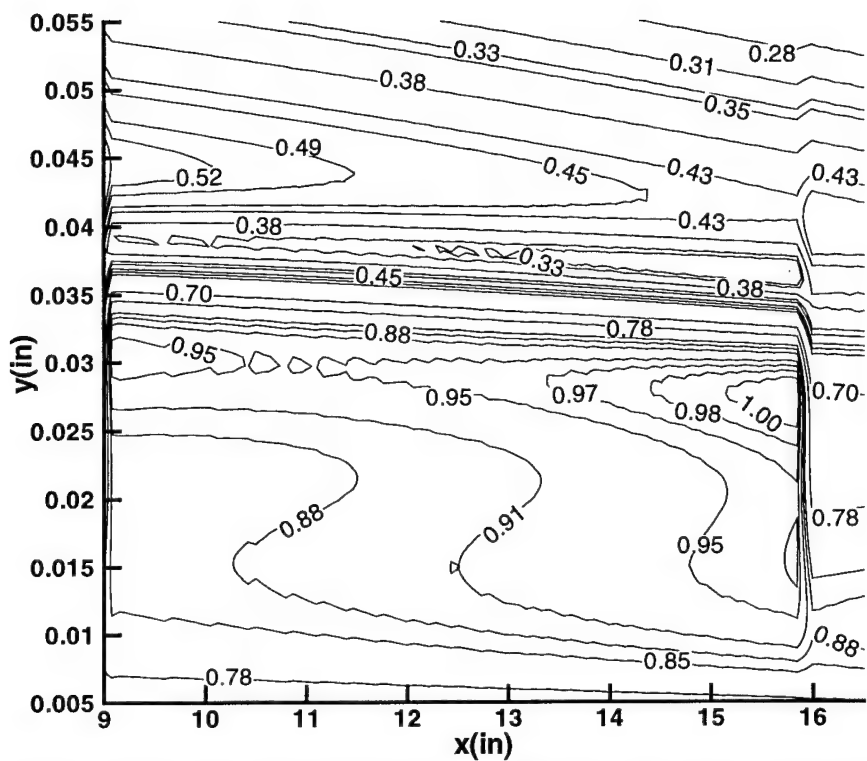


Figure 4.64. Normalized Mass Flux Contour Plot, 91-6 Cooled Model

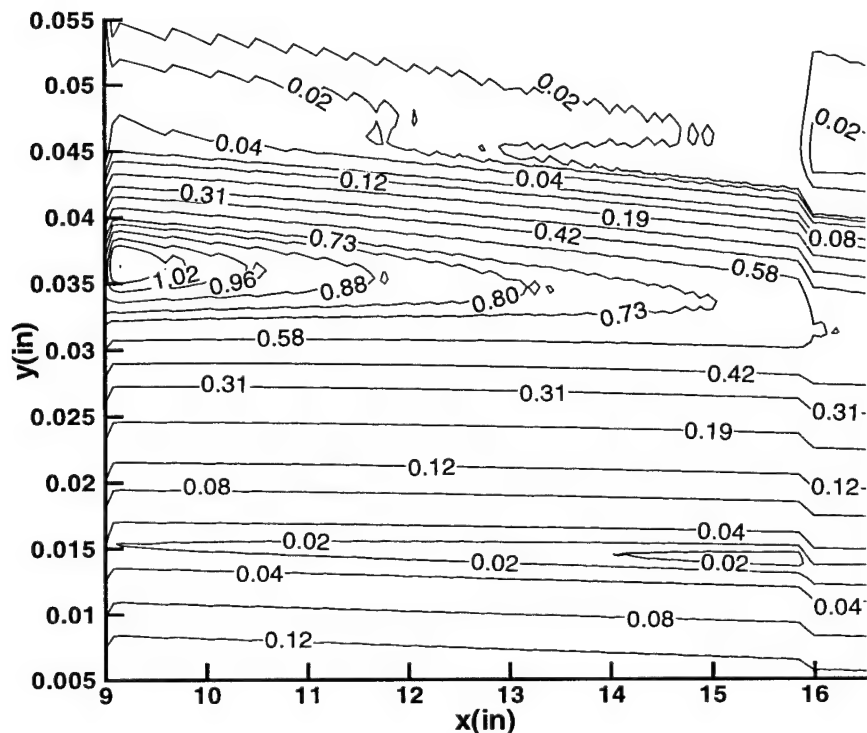
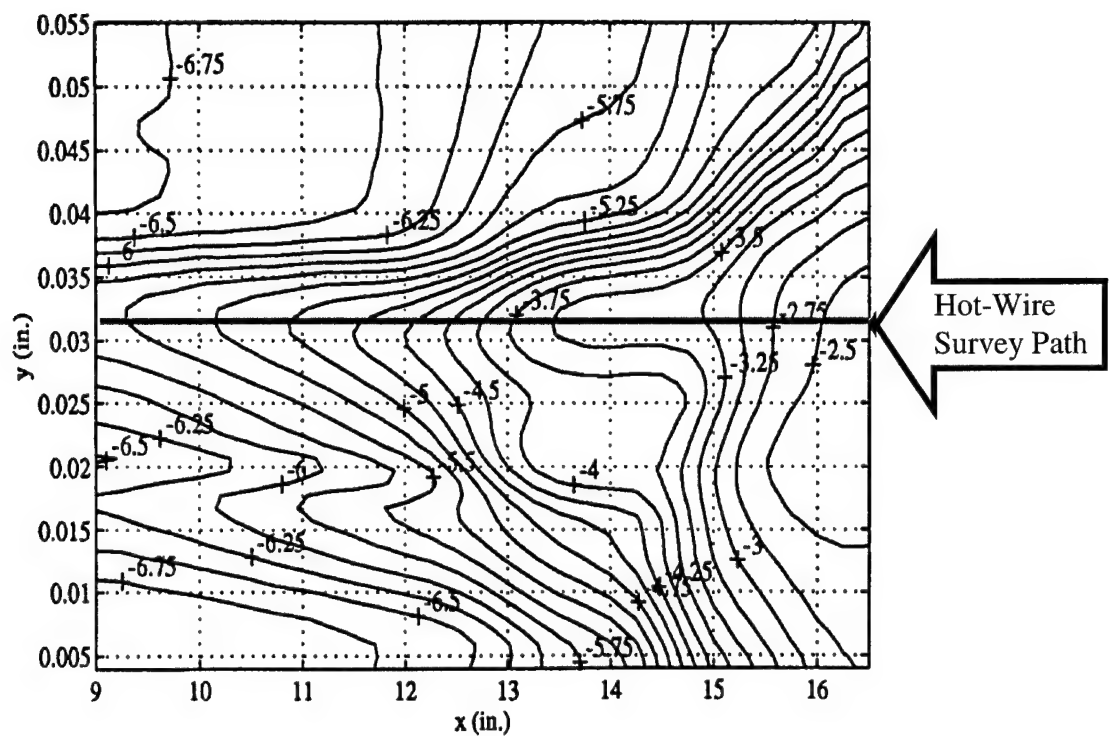


Figure 4.65. Normalized Total Temperature Contour Plot, 91-6 Cooled Model



**Figure 4.66. Hot-Wire Survey Path and RMS Contours for 91-6 Cooled Model
(Blanchard and Selby, 1996)**

CHAPTER 5

CONCLUDING REMARKS

A computational assessment of two stability experiments performed in the NASA Langley Mach 6 Quiet Nozzle Test Chamber Facility has been conducted. Navier-Stokes calculations of the mean flow and linear stability theory analysis of the boundary layer disturbances are conducted. The two experiments analyzed in this work enable the effects of adverse pressure gradient and wall cooling to be examined.

The computed surface pressures are in very good agreement with the experimental measurements. Computed surface temperatures also show overall good agreement with the experiment. However, in the experiments a thin walled model is used. Thus, with wall cooling a pronounced temperature gradient exists on the forward portion of the model, whereas in the computation a constant wall temperature is specified. The use of a variable wall temperature fit to the experimentally measured data for the computations shows that there is neither a significant effect on the mean flow profiles nor on the boundary layer stability due to the temperature gradient. The majority of the experimental measurements are uncalibrated hot-wire measurements. The computed profiles of mass flux and total temperature show very good agreement with hot-wire measurements when the wire is operated in a high and low overheat modes respectively. This finding verifies that the hot-wire operated with the CVA behaves similarly to the more traditional CCA and CTA in regards to the mixed mode sensitivity. In the one case where calibrated hot-wire data are available, the computed and experimental profiles show excellent agreement in the early stages of the transitional flow. In the latter streamwise stations, where nonlinear interactions become important,

differences are seen in the profiles over the height of the boundary layer. In future work, it would be of interest to assess the performance of newly developed transitional models in this region of the boundary layer development.

The sensitivity of the hot-wire to mass flux and total temperature is also examined using the computed wire Reynolds number and eigenfunction profiles. The analysis suggests that even when operated in the high overheat mode, the sensitivity of the hot-wire to total temperature is significant. This is most clearly observed when profiles of the CVA output are compared with eigenfunctions of mass flux and total temperature. The eigenfunctions show multiple peaks, whereas the CVA output shows only two peaks. The variation of the wire Reynolds number across the boundary layer suggests a highly nonlinear response of the hot-wire. Thus, while uncalibrated hot-wire measurements are useful to characterize the overall features of the flow, calibrated hot-wire measurements are necessary for quantitative flow comparisons with stability theory results. In order to make comparisons with PSE it is also necessary to adequately document the initial flow conditions in the experiment.

The computed effects of adverse pressure gradient and wall cooling are found to be consistent with experimental observations. The boundary layer thickness decreases with both adverse pressure gradient and wall cooling. The unstable second mode disturbances are tuned to the boundary layer thickness; thus, the frequencies of the disturbances increase with added adverse pressure gradient and wall cooling. The amplification rates of the unstable disturbances also increase due to adverse pressure gradient and wall cooling. In future work it will be useful to conduct PSE analysis,

which takes into account nonlinear and nonparallel effects; this analyses, however, requires calibrated hot-wire experimental measurements.

REFERENCES

Balakumar, P., Malik, M. R., "Effect of Adverse Pressure Gradient and Wall Cooling on Instability of Hypersonic Boundary Layers," *High Technology Report No. HTC-9404*, March 1994.

Beckwith, I. E., "Development of a High Reynolds Number Quiet Tunnel for Transition Research," *AIAA Journal*, Vol. 13, No. 3, March 1974, pp. 300-306.

Blanchard, A. E. and Selby, G. V., "An Experimental Investigation of Wall-Cooling Effects on Hypersonic Boundary-Layer Stability in a Quiet Wind Tunnel," *NASA CR-198287*, 1996.

Chang, C. -L. and Malik, M. R., "Non-Parallel Stability of Compressible Boundary Layers," *AIAA Paper 93-2912*, July 1993.

Chen, F. -J., Malik M. R. and Beckwith, I. E., "Boundary-Layer Transition on a Cone and Flat Plate at Mach 3.5," *AIAA Journal*, Vol. 27, No. 6, June 1989, pp. 687-693.

Chen, F. -J., Wilkinson, S. P. and Beckwith, I. E., "Görtler Instability and Hypersonic Quiet Nozzle Design," *Journal of Spacecraft and Rockets*, Vol. 30, No. 2, March-April 1993, pp. 170-175.

Chokani, N., "Nonlinear Spectral Dynamics of Hypersonic Laminar Boundary Layer Flow," *Phys. Fluids*, Vol. 12, December 1999, pp. 3846-3851.

Chokani, N., "Wavelet Analysis of a Hypersonic Laminar Boundary Layer Flow," *AIAA Paper 2000-0535*, January 2000.

Comte-Bellot, G., "Hot Wire Anemometry," in *Handbook of Fluid Dynamics*, Chap. 34, edited by R. W. Johnson, CRC Press, Boca Raton, FL, 1998.

Demetriades, A. "Boundary-Layer Instability Observations at Mach Number 7," *Journal of Applied Mechanics - Transactions of the ASME*, March 1977, pp. 7-10.

Demetriades, A., "New Experiments on Hypersonic Boundary Layer Stability Including Wall Temperature Effects," *Proc. Heat Transfer and Fluid Mechanics Institute*, Vol. 39, 1978.

Doggett, G. P., Chokani, N. and Wilkinson, S. P., "Effects of Angle of Attack on Hypersonic Boundary Layer Stability in a Quiet Wind Tunnel," *AIAA Journal*, Vol. 35, No. 3, March 1997, pp. 464-470.

Edwards, J. R., "Nonlinear Relaxation/Quasi-Newton Algorithm for the Compressible Navier-Stokes Equations," *AIAA Journal*, Vol. 31, No. 1, January 1993, pp. 57-60.

Edwards, J. R., "A Diagonal Implicit/Nonlinear Multigrid Algorithm for Computing Hypersonic, Chemically-Reacting Viscous Flows," *AIAA Paper 94-0762*, January 1994.

Edwards, J. R., "A Low-Diffusion Flux-Splitting Scheme for Navier-Stokes Calculations," *AIAA Paper 95-1703-CP*, 1995.

Garriz, J. A., Vasta V. N. and Sanetrik M. D., "Issues Involved in Coupling Navier-Stokes Mean-Flow and Linear Stability Codes," *AIAA Paper 94-0304*, January 1994.

Gasperas, G., "The Stability of the Compressible Boundary Layer on a Sharp Cone at Zero Angle of Attack," *AIAA Paper 87-0494*, January 1987.

Gridgen User Manual, Version 13.3, POINTWISE® Inc., Copyright © 1997-99.

Hall, P., "The Linear Development of Görtler Vortices in Growing Boundary Layers," *Journal of Fluid Mechanics*, Vol. 130, pp. 41-58 July 1982.

Herbert, T., "Boundary-Layer Transition - Analysis and Prediction Revisited," *AIAA Paper 91-0737*, January 1991.

Herbert, Th., Stuckert, G. K., and Lin, N., "Method for Transition Prediction in High-Speed Boundary Layers," *WL-TR-93-3097*, September 1993.

Hudson, M. L., *Linear Stability of Hypersonic Flows in Thermal and Chemical Nonequilibrium*, Ph. D. Dissertation, North Carolina State University, February 1996.

Hudson, M. L., Chokani, N., and Candler, G. V., "Linear Stability of Hypersonic Flow in Thermochemical Nonequilibrium," *AIAA Journal*, Vol. 35, No. 6, pp. 958-964, June 1997.

Iyer, V., Assessment of Meanflow Solutions for Instability Analysis of Transitioning Flows," *AIAA Paper 91-1638*, June 1991.

Kendall, J. M. Jr., "An Experimental Investigation of Leading-Edge Shock-Wave - Boundary-Layer Interaction at Mach 5.8," *Journal of Aeronautical Sciences*, Vol. 24, January 1956, p. 47-56.

Kendall, J. M., "Wind Tunnel Experiments Relating to Supersonic and Hypersonic Boundary Layer Transition," *AIAA Journal*, Vol. 13, No. 3, March 1975, pp. 290-299.

Kendall, J. M., "Experimental Methods and Results on Supersonic Boundary-Layer Stability and Receptivity," *Course Notes Prepared for ICASE/LaRC Short Course on Transition*, June 1993.

Kimmel, R. L., and Kendall, J. M., "Nonlinear Disturbances In a Hypersonic Laminar Boundary Layer," *AIAA Paper 91-0320*, January 1991.

Kimmel, R. L. and Poggie, J., "Disturbance Evolution and Breakdown to Turbulence in a Hypersonic Boundary Layer: Ensemble-Averaged Structure," *AIAA Paper 97-0555*, January 1997.

Kimmel R. L., and Poggie, J., "Effect of Total Temperature on Boundary Layer Stability at Mach 6," *AIAA Journal*, Vol. 38, No. 9, September 2000, pp. 1754-1755.

Kimmel, R. L., "Hypersonic Boundary Layer Stability Measurements Using Uncalibrated Hot Wires," *AIAA Paper 2001-0275*, January 2001.

Lachowicz, J. T., and Chokani, N., "Hypersonic Boundary Layer Stability Experiments in a Quiet Wind Tunnel with Bluntness Effects," *NASA CR-198272*, January 1996.

Lachowicz, J. T., Chokani, N., and Wilkinson, S. P., "Boundary-Layer Stability Measurements in a Hypersonic Quiet Tunnel," *AIAA Journal*, Vol. 34, No. 12, December 1996, pp. 2496-2500.

Lees, L. and Lin, C. C., "Investigation of the Stability of the Laminar Boundary Layer in a Compressible Flow," *NACA Technical Note No. 1115*, 1946.

Mack, L., "Boundary-Layer Stability Theory," Special Course on Stability and Transition of Laminar Flow, *AGARD-R-709*, 1984.

Mack, L. M., "Stability of Axisymmetric Boundary Layers on Sharp Cones at Hypersonic Mach Numbers," *AIAA Paper 87-1413*, June 1987.

Malik, M. R., "Transition in Hypersonic Boundary Layers," *4th Symposium on Numerical and Physical Aspects of Aerodynamic Flows*, January 1989.

Malik, M. R., "Hypersonic Boundary Layer Stability," *Journal of Computational Physics*, Vol. 86, 1990, pp. 376-413.

Malik, M. R., " e^{Malik} : A New Spatial Stability Analysis Program for Transition Prediction Using the e^N Method," *High Technology Report No. HTC-9203*, May 1992.

Morkovin, M. V., "Fluctuations and Hot Wire Anemometry in Compressible Flow," *AGARDograph 24*, November 1956.

Morkovin, M. V., "Critical Evaluation of Transition from Laminar to Turbulent Shear Layers with Emphasis on Hypersonically Traveling Bodies," *AFFDL-TR-68-149*, Air Force Flight Dynamics Laboratory, Wright-Patterson AFB, OH, 1969.

Pate, S. R. and Schueler, C. J., "Radiated Aerodynamic Noise Effects on Boundary-Layer Transition in Supersonic and Hypersonic Wind Tunnels," *AIAA Journal*, Vol. 7, No. 3, March 1969, pp. 450-457.

Pate, S. R., "Measurements and Correlations of Transition Reynolds Numbers on Sharp Slender Cones at High Speeds," *AIAA Journal*, Vol. 9, No. 6, January 1971, pp. 1082-1090.

Potter, J. L., "Observations on the Influence of Ambient Pressure on Boundary Layer Transition," *AIAA Journal*, Vol. 6, No. 10, October 1968, pp. 1907-1911.

Pruett, C. D., and Chang C-L, "Direct Numerical Simulation of Hypersonic Boundary-Layer Flow on a Flared Cone," *Theoretical and Computational Fluid Dynamics*, Vol. 11, 1998, pp. 49-67.

Reshotko, E., "Boundary Layer Instability, Transition, and Control," *AIAA Paper 94-0001*, January 1994.

Reshotko, E., "Progress, Accomplishments and Issues in Transition Research," *AIAA Paper 97-1815*, June 1997.

Sarma, G. R., "Transfer Function Analysis of the Constant Voltage Anemometer," *Review of Scientific Instruments*, Vol. 69, No. 6, June 1998, pp. 2385-2391.

Sarma, G. R. and Lankes, R. W., "Automated Constant Voltage Anemometer with *in situ* Measurements of Overheat and Time Constant of Hot Wire," *Review of Scientific Instruments*, Vol. 70, No. 5, May 1999, pp. 2384-2386.

Schneider, S. P., "Private Communication," June 2000.

Stetson, K. F., Thompson, E. R., Donaldson, J. C. and Siler, L. G., "Laminar Boundary Layer Stability Experiments on a Cone at Mach 8, Part 1: Sharp Cone," *AIAA Paper 83-1761*, July 1983.

Stetson, K. F., Thompson, E. R., Donaldson, J. C. and Siler, L. G., "Laminar Boundary Layer Stability Experiments on a Cone at Mach 8, Part 2: Blunt Cone," *AIAA Paper 84-0006*, January 1984.

Stetson, K. F., Thompson, E. R., Donaldson, J. C. and Siler, L. G., "Laminar Boundary Layer Stability Experiments on a Cone at Mach 8, Part 4: on Unit Reynolds Number and Environmental Effects," *AIAA Paper 86-1087*, May 1986.

Stetson, K. F., Thompson, E. R., and Donaldson, J. C and Siler, L. G., "On Hypersonic Transition Testing and Prediction," *AIAA Paper 88-2007*, January 1988.

Stetson, K. F., Thompson, E. R., Donaldson, J. C. and Siler, L. G., "Laminar Boundary Layer Stability Experiments on a Cone at Mach 8, Part 5: Tests with a Cooled Model," *AIAA Paper 89-1895*, June 1989.

Stuckert, G. K., and Lin., N., "Nonparallel Effects in Hypersonic Boundary Layer Stability," *AIAA Paper 95-0776*, January 1995.

Tannehill, J. C., Anderson, D. A., and Pletcher, R. H., *Computational Fluid Mechanics and Heat Transfer*, Taylor & Francis Publishers, Washington, DC, 1997.

Warren, E. S. and Hassan, H. A., "Transition Closure Model for Predicting Transition Onset," *Journal of Aircraft*, Vol. 35, No. 5, September 1998, pp. 769-775.

White, F. M., *Viscous Fluid Flow*, 2nd ed., McGraw-Hill, New York, 1991.

Wilkinson, S. P., "A Review of Hypersonic Boundary Layer Stability Experiments in a Quiet Mach 6 Wind Tunnel," *AIAA Paper 97-1819*, 1997.